THE RESONANT JUNCTION TRANSISTOR

A Dissertation

Presented to the Faculty of the Graduate School

of Cornell University

In Partial Fulfillment of the Requirements for the Degree of

Doctor of Philosophy

by

Eugene Oh Hwang

January 2012

THE RESONANT JUNCTION TRANSISTOR

Eugene Oh Hwang, Ph. D.

Cornell University 2012

Vibrating RF MEMS resonators have emerged as a potential solution for implementing monolithically integrated filters and frequency references for applications that require extreme scaling of size and weight. Electrostatically transduced resonators in particular have received attention as on-chip stable high frequency references due to their compatibility with existing CMOS processes and high quality factor (*Q*) often exceeding 10,000. Many of these electrostatic resonators, however, use extremely small air-gaps, which pose significant reliability problems, or use very thick device layer (> 10 μm) silicon-on-insulator (SOI) substrates, which require significant changes to existing SOI CMOS processes and significantly increases cost. This dissertation presents a novel transduction mechanism using the depletion forces in pn-diodes to achieve efficient transduction at frequencies exceeding 1 GHz without sacrificing *Q*, fabricated in a process that can be completely integrated into a typical SOI RF CMOS front end process flow without any significant changes.

This dissertation presents the theory of actuation and sensing, fabrication process, and experimental results for these pn-diode internally transduced RF MEMS resonators fabricated in the Cornell Nanoscale Science and Technology Facility (CNF). Measurements were performed using a pseudo-differential setup to

demonstrate the feasibility of using such devices in conjunction with simple interfacing electronics. Experimental results indicate Q = 18,000 at a resonant frequency of 3.72 GHz, yielding the highest reported electrically measured room temperature f-Q product in silicon to date of 6.69×10^{13} Hz.

The high Q of these devices – approaching the material limit in silicon – can be attributed in part to the simple transducer using only a homogeneous doped single-crystal silicon structure. Such devices might therefore be useful for investigating the intrinsic acoustic loss mechanisms not only in silicon, but also in any other semiconducting material whose electrical properties can be controlled by doping. In this dissertation, we use these devices to present the first experimental verification of Landau-Rumer phonon-phonon scattering in single-crystal silicon at gigahertz frequencies via temperature measurements. In addition, data presented in this dissertation at low temperatures below 50 K indicates that electron-phonon scattering may play a greater role in limiting the Q of gigahertz silicon mechanical resonators than previously believed.

While pseudo-differential measurements were able to yield a distinct second-order transmission response, the need for a differential environment may be a limitation for certain systems where a single-ended architecture is necessary, especially for ultra low-power or portable applications. To solve this problem, we make use of the piezoresistive property of single-crystal silicon (i.e., change in resistivity due to elastic strain) to sense the output motional current. This sensing mechanism eliminates the direct feedthrough path from input to output formed by the static capacitance of the transducers and allows for electrical detection of the mechanical resonance using a simple two-port RF measurement setup. In this dissertation, we employ a variation of

the presented pn-diode transduced RF MEMS resonator which uses piezoresistive sensing through the lightly doped channel in an embedded junction field effect transistor (JFET) – the resonant junction transistor. Using this device, we demonstrate a micromechanical resonator with Q = 25,900 at a resonant frequency of 1.61 GHz. The frequency selective acoustic transconductance induced via the piezoresistive effect is 171 μS for a drain current of 143 μA, yielding an acoustic transconductance to bias current ratio (g_a/I_D) of 1.2 V^{-1}. When integrated with SOI RF CMOS transistors that can provide power gain at the resonant frequency, this value puts this device in the realm of practicality for monolithic, direct synthesis of high-frequency local oscillator (LO) signals for low-power transceivers.

BIOGRAPHICAL SKETCH

Eugene Oh Hwang was born in Tempe, AZ to Jeong-Mo and Jae-Wan Hwang on July 11, 1983. Eugene lived in multiple locations throughout his childhood including Tempe, AZ; Pittsburgh, PA; and Plano, TX, where he has to date spent the longest time at any single residence – six years – and graduated from Matthews Elementary School. His family then moved to Taejeon, South Korea, where he attended Eoeun Elementary School and the nearby Eoeun Middle School. After four years in the country of his ethnicity, he returned to the United States and in 2002, graduated from Monta Vista High School in Cupertino, CA. Following high school, Eugene attended the University of California, Berkeley and obtained his Bachelor of Science in Electrical Engineering and Computer Science in 2006. In August 2006, he joined the OxideMEMS Lab in the School of Electrical and Computer Engineering at Cornell University under the supervision of Prof. Sunil Bhave, where he worked on vibrating RF MEMS resonators for CMOS-integrated filters and frequency references. He obtained his Doctor of Philosophy in Electrical and Computer Engineering in January 2012. He is currently working as a Product Engineer in the inertial sensors product development group at Analog Devices, Inc. in Wilmington, MA working on next generation gyroscopes and accelerometers for high-performance consumer applications.

To my parents, whose wisdom – technical or otherwise –

I am only now beginning to understand

ACKNOWLEDGMENTS

First and foremost, I would like to thank my research advisor, Prof. Sunil Bhave, for his endless support and encouragement during my pursuit of a doctoral degree. I am irreparably indebted to him for providing me with all the resources I could ever need in my research endeavors and for always having a backup plan when things seemed to be going sour. His enthusiasm and wit made my graduate career interesting and enjoyable. His genuine concern for his students is not common amongst research advisors and I consider myself extremely lucky to have worked with him and be able to call him a mentor and friend.

I would also like to thank the members of my graduate committee – Prof. Amit Lal, Prof. Edwin Kan, and Prof. Alyosha Molnar – for their advice and support during my time here. Their technical insight and probing questions have guided the directions of my research and my work at Cornell would not have reached its current level without their guidance. I am particularly thankful for their willingness to just sit down and answer any questions I may have had, in many cases, without prior warning. It has certainly been a joy to absorb their both deep and far-reaching breadth of knowledge during these discussions.

I am also thankful for the friendship and support of past and present members of the OxideMEMS Lab: Dana Weinstein, Hengky Chandrahalim, Suresh Sridaran, Tiffany Cheng, Laura Fegely, David Hutchison, Siddharth Tallur, Tanay Gosavi, and Ryan Wang. I am honored to be considered their colleague and look forward to working with them now and in the future. I am particularly indebted to Dana and Hengky for their mentorship during our overlapping time at Cornell. The SonicMEMS group members also deserve my gratitude for their friendship, in particular Rajesh Duggirala, Kursad Araz, Serhan Ardanuc, Alper Bozkurt, Norimasa Yoshimizu,

Steven Tin, Abhishek Ramkumar, Siva Prasad, Janet Shen, Kwame Amponsah, Larry Lu, Yue Shi, and Sarvani Piratla. I would particularly like to thank Kwame for sharing lab equipment and his know-how with regards to device fabrication, as well as helpful discussions.

This work would not be possible without the help and support of the entire staff of the Cornell Nanoscale Science and Technology Facility (CNF). I would specifically like to name Paul Pelletier and Rob Ilic for their help with ion implantation, Garry Bordonaro for his help with photolithography, Aaron Windsor for his help with the evaporator and RTA, Jerry Drumheller for constantly changing out sputtering targets, and Mike Skvarla for many helpful discussions during which he imparted unto me much of his fabrication wisdom.

A significant portion of my work here has been done through collaboration with colleagues at the U.S. Army Research Laboratory: Ron Polcawich, Jeff Pulskamp, Sarah Bedair, and Andrew Driscoll. Their assistance ranging from help with low temperature measurements to fabrication of lead zirconium titanate (PZT) resonators and filters in addition to their extensive technical expertise has made working with them an enjoyable and technically edifying experience.

I would like to thank the "ECE Ph.D. Korean mafia" for caring for me as they would a brother: Jae-goo Lee, Yong-cheol Choi, Jeonghyun Hwang, Daniel Seung Lee, Moon Kyung Kim, Sang Hyeon Lee, Jaeyoon Kim, Seung Keun Yoon, Tae Eung Sung, Wooram Lee, Joon Young Kwak, Changhyuk Lee, Jaesung Lee, Jinsub Lee, Daniel Joe, and Yoon Ho Lee. I would especially like to thank Jaeyoon Kim and his family for their constant care and support and many delicious home-cooked meals. In addition, other members of the board of the Korean Graduate Student Association at Cornell deserve my thanks for their friendship: Sung A Kim, Justin Kyungseung Choi, Hyunjung Kim, Hyekyung Kim, Wooyoung Jeon, Jungyoon Mo, Raymond Kim,

Yumi Seo, Youngho Chung, Jai Kyoung Jung, and Paul Dongwoo Kim. Others who have made my weekends more enjoyable through Saturday morning soccer and baseball games include Seongyeon Ko, Chanhong Kim, Bonggu Shim, Hanjong Paik, Joonkyum Lee, Oukjae Lee, Dong Hwan Kim, John Sunwoo, Chibeom Park, Jihun Kang, Brian Park, Bongchul Sin, and Yongho Lee.

Other friends in ECE include Paul George, Sunwoo Lee, Xiao Wang, Mustansir Mukadam, Omeed Momeni, Bo Xiang, Wacek Godycki, Shantanu Rajwade, and Krishna Jayant. There are some other people who do not fit into any of the above categories, but that does not by any means indicate they are any less valuable to me. These friends include Matthew Horwitz, Kyeongmin Park, Jee Ho Ryoo, and Youngsang Song.

One special person that is reserved a place in my heart is Bo Ri Seo for her love, sacrifice, and support. The other corner of my heart is reserved for my family: my brother Paul and my parents, whose loving support has always urged me to dream bigger dreams. In particular, my father has been feeding me with wisdom that I have continuously rejected for the past quarter century until I have only recently begun to realize just how valuable his words really are. As for my mother, it is evident that her love is blind and unconditional since there are many times that I would have even given up on myself.

Finally, I thank God for this life and I ground myself always in the words which have guided all of my intellectual endeavors:

"*The fear of the LORD is the beginning of wisdom...*"

Proverbs 1:7a

TABLE OF CONTENTS

LIST OF FIGURES

LIST OF TABLES

CHAPTER 1

INTRODUCTION

1.1 Scaling of Electrical Systems and Opportunities for RF MEMS

The exponential advances in technology that have shaped human society since the invention of the first vacuum tube triode at the turn of the 20th century can in some ways be thought of as the history of the miniaturization of electronics. Figure 1.1 shows a timeline illustrating technical milestones enabling the scaling of electrical systems and a handful of innovative applications that have emerged as a result. Prior to the invention of the vacuum tube triode (also called the "audion" by its inventor Lee DeForest [1]), bulky and unreliable crystal receivers were used for the detection of wireless telegraphy or AM modulated audio signals generated by large and inefficient spark-gap transmitters or alternators. The invention of the audion in 1906 revolutionized radio transceivers by reducing their size and cost, making them available to the general public and revolutionizing America by creating a mainstream culture. The influence of the vacuum tube did not stop there, however, and other systems were built based on this new technology, including the all-electrical television and the first general purpose electronic computer ENIAC, which occupied an entire basement [2], [3].

The next big step in the miniaturization of electronics came with the invention of the transistor by Bardeen and Brattain in 1947 [4]. The first realization of this influential device used germanium with a point contact for the injection of minority carriers. This development led to a number of new consumer products, the first of which were mostly small radios and hearing aids. The first fully transistorized computer – the TRADIC – also used these point-contact transistors to reduce size and

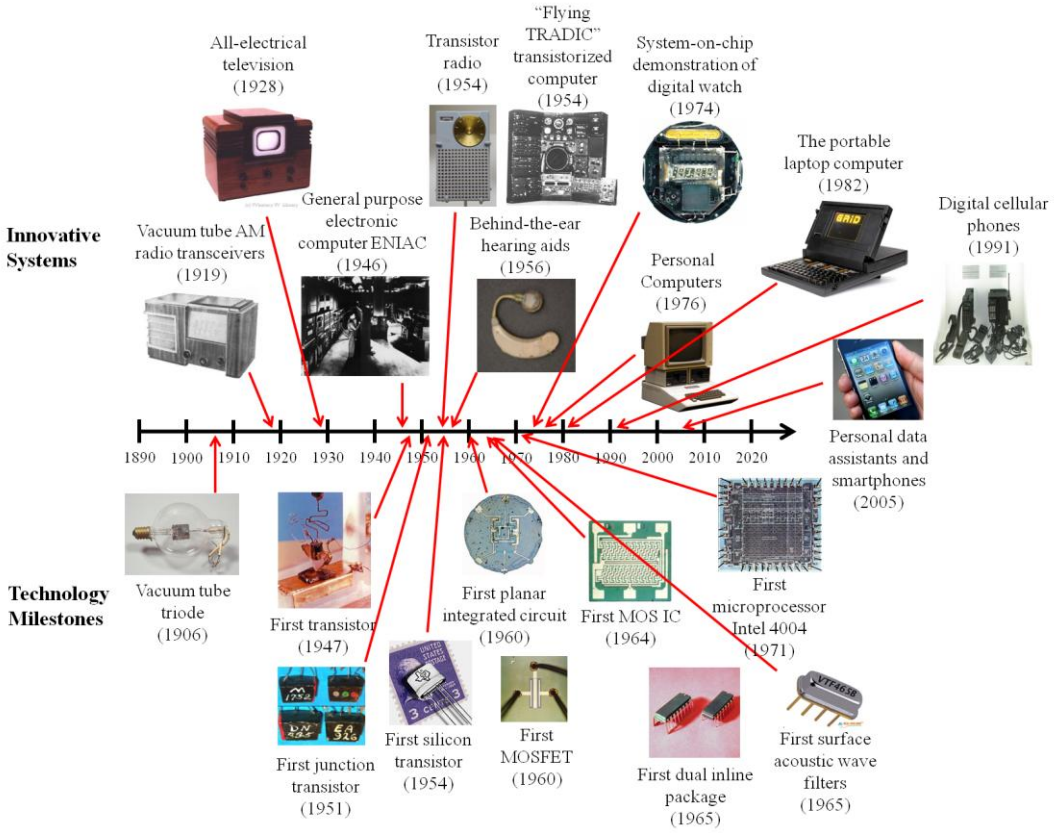

Figure 1.1. Timeline of important technology milestone and new and innovative systems that were developed based on them. This figure illustrates how dimensional scaling of basic computational elements leads to the development of more complex, more powerful systems.

power consumption compared to previous vacuum tube computers [5]. The point contact in these transistors, however, was unreliable and this design was quickly replaced by the junction transistor (today known as the bipolar junction transistor) which was first commercialized in 1951 [6-8]. This further reduced the size of electronics and led to truly portable systems like the transistor radio – an American cultural icon – and concealable behind-the-ear hearing aids. Junction transistors also enabled the reduction of size of the TRADIC computer to fit inside a C-131 aircraft, thus realizing the first airborne transistorized digital computer, the "flying TRADIC" [9].

These first junction transistors were developed using germanium, which had

serious problems with leakage current, making them unacceptable for computer logic. They were also restricted to operating temperatures between 0 and 70°C, limiting their use in rugged applications. Thus, silicon was targeted as the new semiconductor material for transistors and silicon transistors eventually became a reality in 1954, following innovations in refinement techniques that allowed for "semiconductor-grade" silicon [10]. This was the first in a number of innovations in manufacturing technology that led to the fabrication of the first planar integrated circuit (IC) in 1960 by Fairchild Semiconductor, which implemented a Direct Coupled Transistor Logic (DCTL) flip-flop with four transistors and five resistors [11]. In the same year, advances in the understanding and treatment of the semiconductor interface allowed for the first successful demonstration of the metal-oxide-semiconductor field effect transistor (MOSFET) [12].

The rest, as they say, is history. It was not long before the first commercial MOSFET IC was introduced in 1964 [13], allowing for more transistors on a single chip and enabling large scale integrated memory arrays. With the seminal paper by Gordon Moore in 1965 which coined the term "Moore's Law," the era of transistor scaling was in full effect [14]. The first microprocessor IC – the Intel 4004 – was fabricated in 1971 and enabled the concept of the personal computer (PC) in the 70s and 80s, which provided the general public with unprecedented computing power [15]. Continued scaling of transistor technology and the increased computing power available on a single chip with each technology generation continued to increase the performance of the PC and enabled other innovative products, such as the laptop computer [16]. By the 90s, the digital revolution was in full swing and many traditionally analog applications were implemented using digital electronics due to the availability of cheap microcontrollers and digital signal processors (DSP).

These innovations in conjunction with developments in network theory birthed the

World Wide Web (WWW) and ushered in the Information Age, where the free exchange, storage, and processing of information became the main driving force of society. The increasing need to be virtually "plugged in" at all times has since given rise to mobile communication systems, such as 2nd generation (2G) digital cellular networks (1G cellular networks were analog in nature) in the 90s and personal data assistants (PDAs) and smartphones which have emerged within the past few years.

Throughout this past century of technological achievements, the common thread underlying all of this has been the miniaturization of electrical systems. And no other technology has benefited more significantly from this continued miniaturization than complementary MOS (CMOS) technology. In fact, many of the recent advances in mobile technology, particularly in radio frequency (RF) ICs, arise from the fact that certain aspects of MOSFET performance (in particular f_T and f_{max}) improve as dimensions scale. These improvements are driving electronics toward ever higher levels of integration and overall smaller and lighter systems. And yet again, as seen throughout history, the promise of packing ever increasing amounts of computing power into a single chip has brought new ideas (e.g., distributed sensor networks and implantable medical devices for real-time patient monitoring) into the realm of possibility. To be complete, such systems would require a wireless I/O interface, necessitating integration of the RF transceiver with the baseband electronics. However, there are at present many challenges to complete on-chip integration of RF systems in CMOS. One of the most significant of these challenges for radio receivers is the lack of monolithically integrated narrowband filters and stable frequency references.

This is where RF micro-electromechanical systems (MEMS), specifically vibrating RF MEMS resonators and filters, may continue the path towards complete system-on-chip (SoC) integration [17]. This technology has demonstrated resonator quality

factors (*Q*) greater than 10,000 at frequencies now extending into the ultra high frequency (UHF, 300 MHz – 3 GHz) and super high frequency (SHF, 3 GHz – 30 GHz) [18-20]. But the greatest benefit of this technology is its potential for integration into existing CMOS ICs. The availability of such performance on a single silicon chip that can directly interface with state-of-the-art electronics may be exactly what is needed to overcome the challenges listed above.

1.2 Monolithic Integration Strategies for RF MEMS and CMOS

The monolithic integration of RF MEMS and CMOS is a topic that has received much attention and has been investigated by many research groups. The proposed methods can largely be classified depending on the structural material in which the MEMS devices are designed: post-CMOS integration, back-end-of-line integration (BEOL), and front-end-of-line (FEOL) integration. This section will review representative examples of each integration methodology.

1.2.1 Post-CMOS Integration

Of all the methods listed in this overview, most of the approaches that have been proposed to date are those using post-CMOS integration. The main characteristic of this integration method is that the structural material is deposited and patterned above a completed CMOS die and is not an inherent part of the CMOS back end. A prominent example is the Digital Micromirror Device (DMD) technology by Texas Instruments, Inc. shown in Figure 1.2 [21]. This process uses aluminum alloys as the structural material and UV-cured photoresist as the sacrificial layer. One main advantage of this approach is the area savings over the other strategies since this

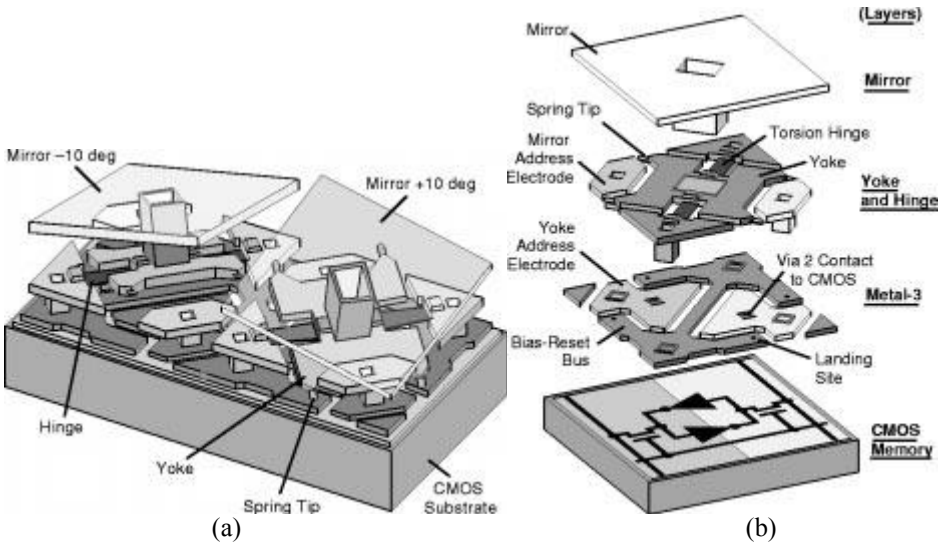

Figure 1.2. (a) Functional illustration of two DMD pixels (mirrors are shown as transparent. (b) Expanded view showing the different post-CMOS fabricated mechanical layers and underlying CMOS memory. Images reproduced from [21].

approach does not exclude any active die area for the underlying electronics. This is exploited in the DMD process by its use of CMOS memory placed directly underneath the moving mirrors, saving area and minimizing routing for optimal addressing. Other groups, such as Prof. Clark Nguyen's and Prof. Khalil Najafi's groups at the University of Michigan, Ann Arbor, have also investigated the possibility of using metal, specifically nickel, as the structural material for resonator applications [22], [23]. These investigations resulted in some moderate Q (>1,000) resonators, but there were other problems associated with drift, instability, and low acoustic velocity limiting the frequency of operation. Some of these problems were improved using a localized annealing method [24], but this required temperatures in excess of 850°C, which may not be suitable for today's deep submicron technologies that use low-K interlayer dielectrics (ILD). Nevertheless, electroplated nickel without an annealing step was possible and a 10 MHz oscillator was demonstrated using this technology (Figure 1.3) [25]. Other work at the University of California, Berkeley investigated polycrystalline silicon germanium as a structural material (Figure 1.4) [26]. These

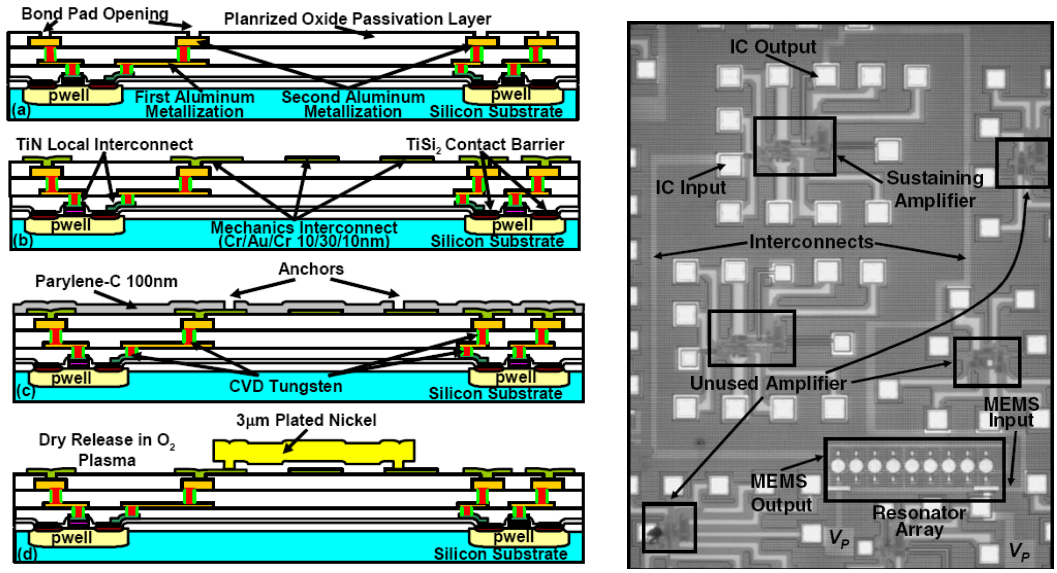

(a) (b)

Figure 1.3. (a) Cross-sectional fabrication process flow for the post-CMOS integration of nickel flexural disk resonators on a 0.35 μm CMOS chip. (b) Optical microscope image of the 10 MHz monolithic nickel micromechanical resonator oscillator. Images reproduced from [25].

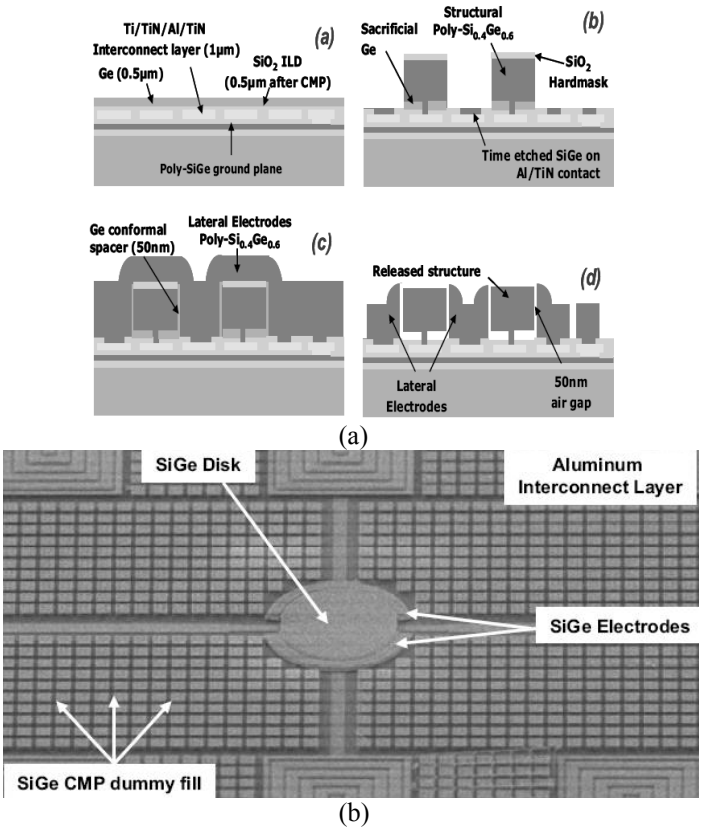

Figure 1.4. (a) Cross-sectional fabrication process flow and (b) SEMs of the poly-SiGe disk resonators. Images reproduced from [26].

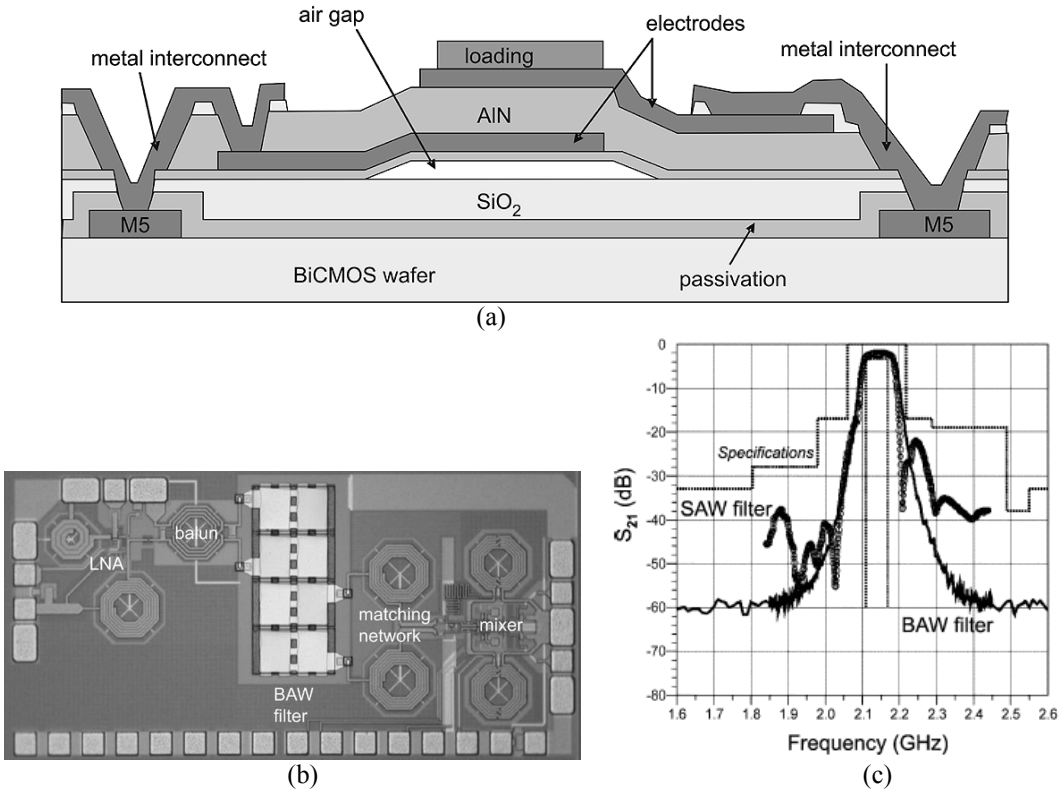

Figure 1.5. (a) Technology cross-section for the integration of AlN FBAR resonators on a 0.25 µm BiCMOS chip. (b) Top view SEM of the RF front-end receiver on BiCMOS chip with integrated AlN FBAR filters as proof-of-concept. (c) Measured results of integrated AlN FBAR compared with external SAW filter. Images reproduced from [27].

resonators had higher *Q* (~10,000) in the very high frequency (VHF) range (30-300 MHz), but still required relatively high deposition temperatures (~450°C) and thus may encounter the same thermal budget limitations as the annealed nickel resonators.

While the previous examples were all targeting electrostatic resonators due to their higher *Q* and use of CMOS-compatible materials, other work from CSEM in Switzerland used piezoelectric materials, specifically aluminum nitride, as the structural material integrated above a BiCMOS chip [27]. Similar thin film bulk acoustic wave (FBAR) resonators have seen great commercial success elsewhere as off-chip filters and duplexers due to their efficient electromechanical coupling, meeting the stringent filter performance requirements of today's mobile devices [28]. The work from CSEM demonstrates some very promising results using their above-IC

FBAR process, shown in Figure 1.5.

There are, however, a number of drawbacks to these methods. The first which has already been briefly discussed is the low thermal budget required for any post-CMOS processing. This severely limits the choice of structural material, and even materials that do meet these requirements may have low *Q* since high temperature annealing is not possible. The more significant drawback, however, is the cost associated with post-CMOS processing. Since mask costs constitute a sizable portion of the total fabrication costs, adding just a few additional masks (especially those defining critical lithography steps) may result in a total cost increase of a factor of two or three [29]. All of the aforementioned post-CMOS processes require at least three extra masks (with the AlN FBAR process using up to six), significantly increasing the total fabrication cost. For many applications, this cost increase over a typical multi-chip solution is not easily justifiable, and thus further development of such processes in an industrial setting has been difficult.

1.2.2 Back-end-of-line (BEOL) Integration

While the post-CMOS method makes use of additional layers not included in the CMOS process, this approach uses the metal or the metal-ILD composite in the CMOS back end as a structural material. Prominent examples include work performed by Prof. Gary Fedder's group at Carnegie Mellon University and more recently by Prof. Sheng-Shian Li at the National Tsing Hua University in Taiwan [30], [31]. The novelty of these methods is that the mask count is reduced by patterning the resonator structure in the same process step as the BEOL metal patterning (Figure 1.6). Using this method, only two extra etching steps without any additional masks are required to

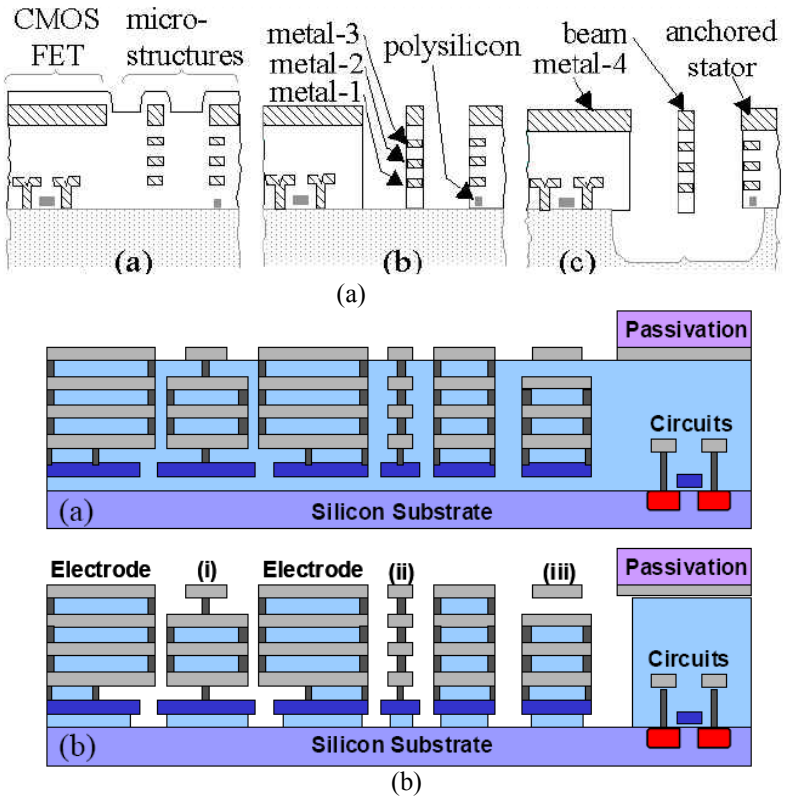

Figure 1.6. Technology cross-sections of representative BEOL integration methods which use the BEOL stack as the structural material etched (a) by DRIE with a metal mask (from [30]) and (b) using via and interconnect metal to protect structures released with commercial SiO_2 etchant selective to metal (from [31]).

completely define the MEMS structure in both of these demonstrations, making this approach a cost-friendly method of monolithic integration.

Due to more conservative design rules in the CMOS back end layers, the gap widths as fabricated for both processes are limited to > 300 nm. Since narrow gaps are desirable for efficient electrostatic transduction, some methods of gap reduction thus need to be implemented in these resonators in order to make them feasible for use in oscillators or filters. The former makes use of Joule heating in the polysilicon layer to cause lateral bending of the device, thus bringing it closer to the electrode and closing the gap. The latter makes use of electrostatic pull-in to reduce the transduction gap. An interesting additional benefit of the latter method is the ability to change the anchoring

boundary conditions of the device, as seen in regions labeled (i), (ii), and (iii) in Figure 1.6(b). This technique allows for a relatively wide range of frequencies that can be implemented on a single die. Both demonstrations show a moderate *Q* (~1,000) in the HF (3-30 MHz) range.

While these methods make clever use of existing BEOL layers to define the resonant structures, there are still drawbacks associated with this approach. The first of these are problems associated with the gap reduction methods. The Joule heating method employed in the first work results in temperatures as high as 900°C during operation, which poses significant problems for long-term or continuous operation and would result in significant performance degradation of the adjacent electronics. The second method using electrostatic tuning requires voltages in excess of 32 V, which may be incompatible with fragile deep submicron CMOS transistors. Also, this method excludes die area where the resonant structure is located from being used for the underlying electronics. This leads to long interconnect lines and more importantly large footprint, which ultimately affects fabrication costs. In addition, the trend in industry towards using low-K ILDs results in low elastic stiffness of the vibrating structure. This places limitations on the achievable resonant frequency of such devices and also results in relatively low *Q* compared to other electrostatic resonators due to small amounts of elastic energy storage.

While it remains to be seen whether or not these approaches are practical for RF MEMS resonators, they may find utility in lower frequency inertial sensors such as accelerometers or gyroscopes, making them feasible candidates for MEMS-CMOS integration for certain applications.

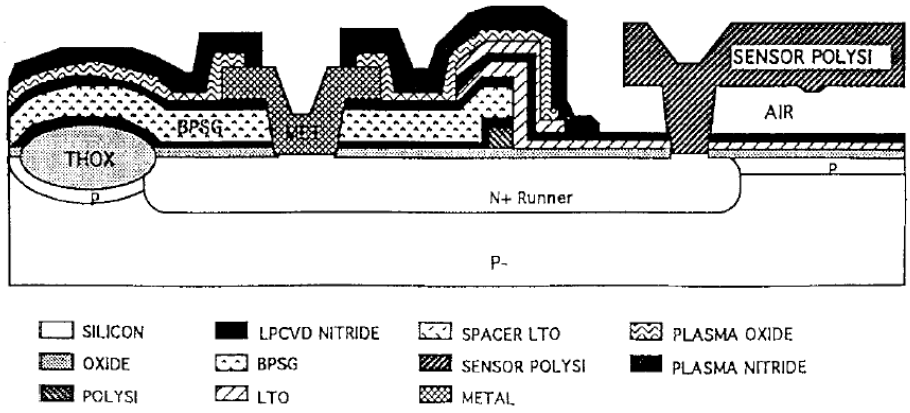

Figure 1.7. Technology cross-section for the interleaved MEMS-BiMOS process used by Analog Devices, Inc. for integrated accelerometers. Image reproduced from [32].

1.2.3 Front-end-of-line (FEOL) Integration

Intuitively, it seems like integration of MEMS devices into the CMOS front end process will significantly compromise the performance of the electronics. This is partially true, which is why this specific approach to monolithic integration has not been widely attempted. There are, however, a few commercial examples of products that use this approach, for example, the ADXL50 low-power accelerometer product line from Analog Devices, Inc. [32]. This product uses an interleaved process which switches back and forth between CMOS and MEMS processing steps. As seen in Figure 1.7, the electrical contact between the MEMS and CMOS circuitry is through n^+ diffused "runners" in the silicon substrate. Special care has been taken in this process to ensure that each process step does not damage either the underlying CMOS or the MEMS devices. This complex process is possible because both the process engineers and circuit designers can work together to optimize the process for the given application. Other advantages of this process include the close proximity of the MEMS device to other electronics, of course, at the cost of active area.

While this customizability can be a good thing, it is also the main drawback of this approach. As we have seen, CMOS scaling driven by Moore's Law has far outpaced that of MEMS devices, especially resonators, since a certain target frequency requires specific resonator geometry and dimensions. This is a good thing for circuit designers in general, but in order to keep device performance within acceptable bounds with each technology generation, many tricks have to be employed, especially in deep submicron CMOS. Some of these tricks are hard to integrate with MEMS in the front end, thus requiring a significant redesign of the process every time when scaling to a more advanced technology node, delaying time to market and increasing cost. It is therefore not surprising to see many products made through such interleaved integration approaches still using transistor technologies that are decades old. In contrast, all of the approaches in the last two subsections begin processing of the actual MEMS devices after all CMOS processing steps are completed, thereby allowing the use of advanced CMOS processes in conjunction with MEMS devices.

Due to these limitations, others have come up with clever ways to use unique features of a typical CMOS front end process to define resonant structures. One example is work performed by Prof. Jeevak Papria's group at Cornell University where they build a dome resonator and "arch-bridge" resonator shown in Figure 1.8 using a two-poly front end CMOS process [33]. This work makes clever use of the "bird's beak" that forms during thermal oxidation in the presence of a thin silicon nitride layer and is typically used in CMOS processes to provide isolation between transistors. This work combines the benefits of some of the previous approaches while solving some of the drawbacks: polysilicon can be used as the structural material for potentially higher frequency and Q than BEOL integration methods without the thermal budget constraints and extra masks required of the post-CMOS methods (only two addition etch steps at the end, like BEOL integration methods). Also, the

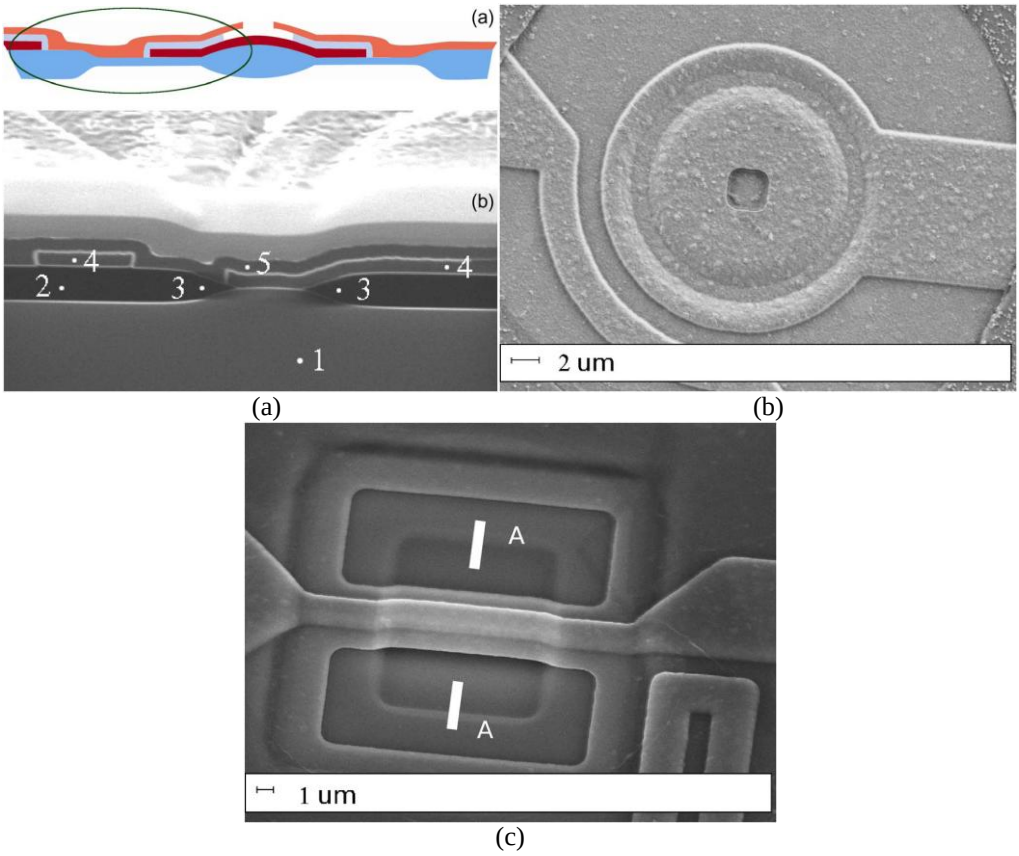

Figure 1.8. (a) Cross section and (b) top view SEM of polysilicon dome resonator using the front-end polysilicon as the structural material fabricated in a 1.5 µm 2-poly 2-metal commercial foundry. (c) Top view SEM of arch-bridge resonator fabricated in same process. Images reproduced from [33].

resonator can easily be incorporated into any CMOS process that uses two polysilicon layers (this work uses a 1.5-µm 2P2M CMOS process from ON Semiconductor available through MOSIS) since it is defined independently of other front end process considerations, making it possible for designers to leverage the improved performance of deep submicron processes (unlike the interleaved front end integration process). This particular resonator design does, however, suffer from a few drawbacks of its own, specifically that the resonant frequency is extremely sensitive to the length of the HF release step and the polysilicon film stress. Also, due to the flexural resonant mode of this resonator, resonators operating at frequencies beyond the VHF band would likely be unachievable. While these issues do exist, the basic idea of incorporating the

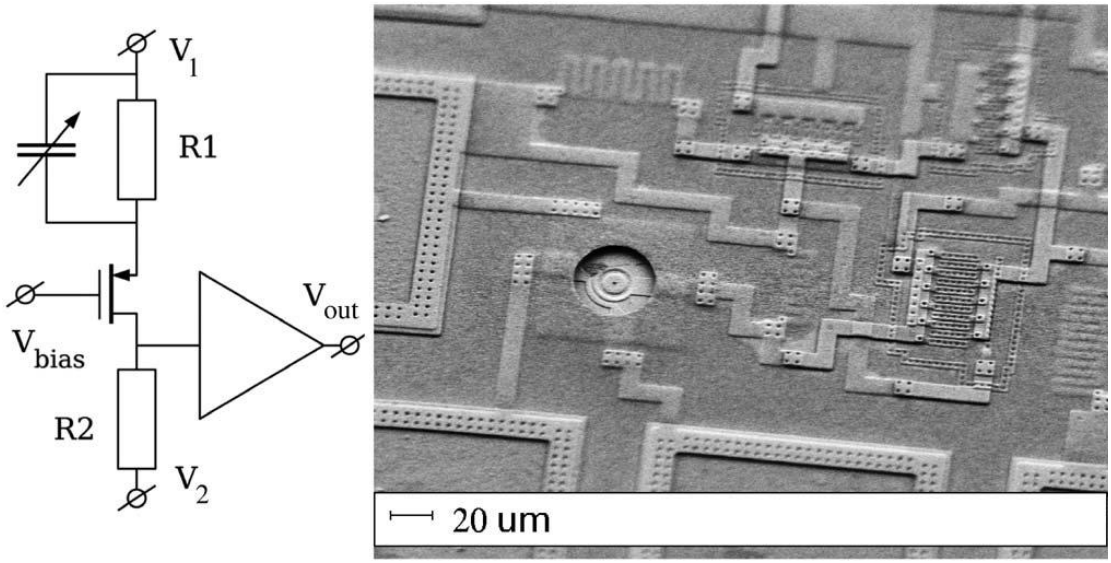

Figure 1.9. Equivalent circuit schematic and top view SEM showing the on-chip transimpedance amplifier (TIA) circuit for electrical readout. The dome resonator is represented as a time varying capacitor degenerating the source of a PMOS transistor. The small signal current through the transistor is modulated by the impedance of this capacitor and is converted to a voltage by the TIA. Image reproduced from [33].

MEMS resonator into an unmodified CMOS front end process in close proximity to the electronics is the main novelty of this work.

In this work, the authors also demonstrate an interesting electrical drive and sense technique made possible due to the close proximity to electrical circuits. Figure 1.9 shows this setup where the resonator acts as a time-varying source degeneration impedance for the PMOS transistor. While this technique is limited to low frequencies where the shunt capacitive admittance of the resonator is much smaller than the transconductance (g_m) of the transistor to which it is connected, it is a very interesting demonstration of using mechanical resonance to modulate the drain current through a transistor and serves as a compelling demonstration of interesting circuit-device interactions that are possible with the monolithic integration of RF MEMS resonators.

Surprisingly, this idea is not new. In fact, the first ever demonstration of microfabricated mechanical resonators – and sadly, too far ahead of its time – used

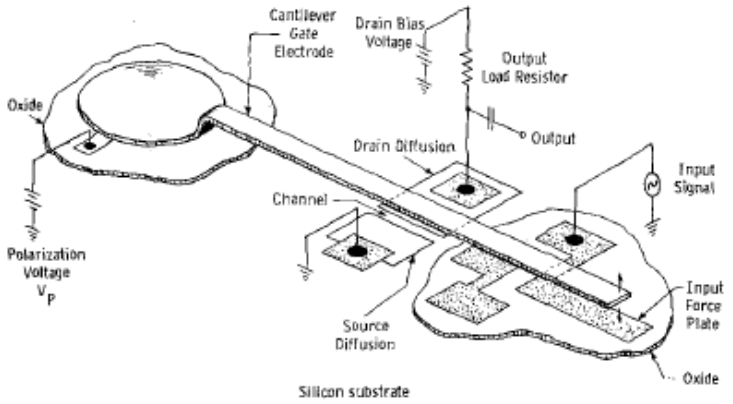

Figure 1.10. Illustration of the RGT device structure showing gold cantilever gate electrode, source/drain regions, and actuation electrode. The movement of the gate modulates the gate capacitance and thus channel charge distribution. Image reproduced from [34].

this very idea of mechanical modulation of transistor characteristics for electrical detection: the resonant gate transistor (RGT) developed by Harvey C. Nathanson at Westinghouse in 1967 [34]. Here, the transistor gate is a floating cantilever placed above the MOSFET channel (Figure 1.10) and mechanical motion is excited by a separate electrode placed underneath the cantilever. When the input voltage excites mechanical resonance, the gate capacitance (in this case, the dielectric is air) is modulated, effecting the charge density in the inverted channel and resulting in modulation of the drain current. Unfortunately, microfabrication technology in the 1960s still suffered from significant reliability and yield issues, halting further development of this idea. However, recent works have rediscovered and modified it to demonstrate other methods of coupling between mechanical resonance and transistor electrical behavior, giving birth to hybrid resonant transistors [35]-[37]. Such hybrid resonant transistors provide a number of advantages, including elimination of a direct capacitive feedthrough path and the possibility of gain in a MEMS resonator.

One example of such hybrid devices is work by Prof. Adrian Ionescu's group at EPFL in Switzerland. They demonstrate HF and VHF resonators with Q ~ 6,000-7,000 using both flexural and bulk mode MEMS resonators with built in transistors, which

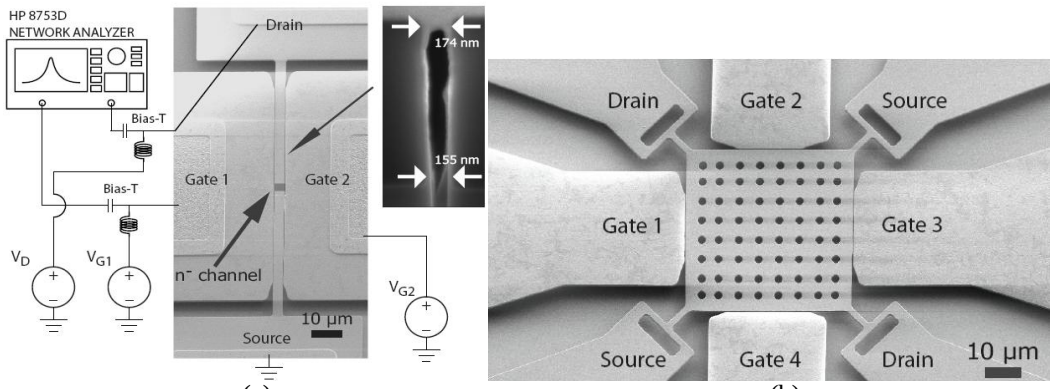

Figure 1.11. Top view SEMs of the (a) dual-channel flexural beam and (b) four-channel bulk acoustic wave vibrating-body field effect transistors. Inset plot in (a) shows the narrow transduction gaps achieved through this fabrication process. Images reproduced from [35].

they call the vibrating body field effect transistor (VB-FET) shown in Figure 1.11. Interestingly enough, their transistor of choice is an accumulation-mode nMOSFET with an n^- channel region. They use such a configuration with a very narrow air-gap functioning as both the input transducer and the nMOSFET gate dielectric. The use of an accumulated channel here maximizes electromechanical transduction since all of the input actuation voltage is now applied across the transducer instead of being split between a gate capacitance in series with a bulk capacitance, as would be the case for an inverted channel. In this case, the movement of the body causes a modulation of the accumulated channel charge. In addition, there is also a piezoresistive modulation in the bulk region further away from the channel due to the strain fields within the structure. They have determined based on their analysis in [36] that for flexural mode resonators, the channel charge modulation effect is the dominant origin of output motional current, whereas in the bulk mode resonators, piezoresistive modulation becomes dominant. This can be readily understood by noticing that in flexural mode resonators, the integrated strain in the bending direction sums to zero and that the amplitude of motion is a larger percentage of the gate dielectric gap width than in the case of bulk mode resonators.

Using their 2 MHz flexural mode resonators, they demonstrate for the first time a MEMS resonator with gain under appropriate bias conditions. As always though, this device suffers from a number of drawbacks. The need for very narrow air-gaps presents a large obstacle to monolithic integration in a typical foundry CMOS process. The devices in this work use air-gaps of roughly 150 nm width fabricated using a sacrificial polysilicon layer, but the incorporation of this into a standard SOI CMOS process would result in an interleaved process much like the approach used in [32] with the same associated drawbacks of that method. Another more technical problem with using an air-gap is the reduced performance of the transistor itself due to degraded gate control of the channel. In order for this device to achieve the same gate control that is seen in typical CMOS transistors with gate oxide thicknesses roughly on the order of 10 nm, the air-gap width must be reduced by a factor equal to the gate oxide dielectric constant, resulting in a necessary gap width of roughly 2.5 nm. With a 150 nm gap width, gate control is in fact reduced by roughly a factor of 60, as seen in the I-V curves of Figure 1.12 which shows little change in the drain current for different values of the gate voltage. In actuality, the gate control is reduced even further for these specific devices since they are operating in accumulation mode with an n^- channel doping, meaning that there are parallel current paths away from the accumulated channel at the surface that are not controlled by the gate. This is especially troublesome for low-power analog or RF circuit design since the transconductance g_m is significantly reduced, resulting in very low values of transconductance to drain current ratio g_m/I_D, a measure of the signal amplification for a given power consumption of a transistor. The g_m/I_D value for this device is roughly 0.003 V^{-1} ($g_m \sim 1.7$ μS, $I_D \sim 560$ μA), which is unacceptably low for any low-power application (typical CMOS processes have values of roughly 10-20 V^{-1} in moderate inversion, BJTs theoretically have values as high as $q/kT \sim 38$ V^{-1}).

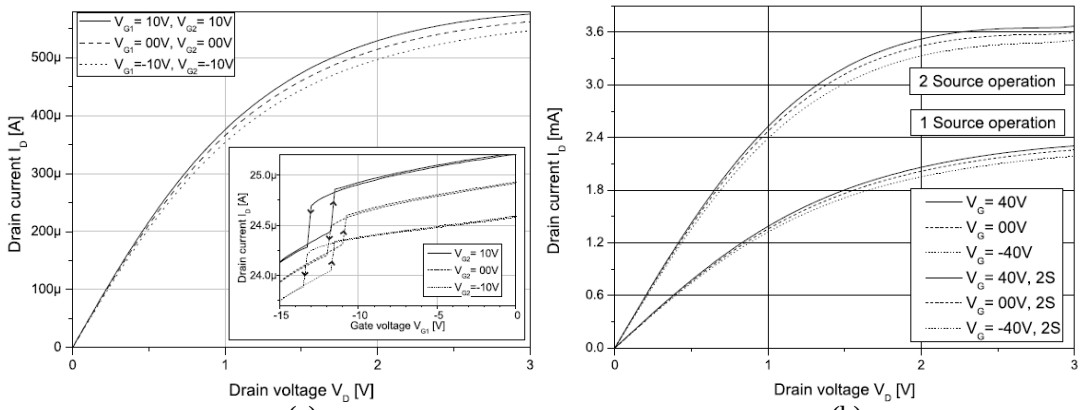

(a) (b)

Figure 1.12. I_D vs. V_D characteristics of the (a) dual-channel flexural beam VB-FET and (b) four-channel bulk VB-FET for varying gate voltage combinations. Images reproduced from [35].

To alleviate some of the problems associated with using an air-gap, Dana Weinstein while at Cornell University investigated a novel method of transduction called internal dielectric transduction, which uses a thin solid dielectric film embedded in the body of a resonator to excite acoustic waves within the structure [20], [38]. The theory for such transduction shows that when the dielectric film is optimally placed at a displacement node within the resonant structure, the transduction efficiency increases with increasing frequency until the film thickness corresponds to half the acoustic wavelength. This characteristic frequency for a device with a 15 nm nitride film embedded in a polysilicon resonator as presented in this work is roughly 367 GHz, indicating the potential of this method for RF and microwave applications.

This thin dielectric film was used to replace the air-gap used in the previous work to now enable transduction in the UHF band (300 MHz – 3 GHz) and this device was dubbed the resonant body transistor (RBT) [37]. Other improvements were also made, including the use of an inverted channel for improved gate control. While this is not as crucial to the device performance as in the VB-FET since the main mechanism of output motional current here is the piezoresistive effect in the channel rather than channel charge modulation, it is necessary to turn off the drain current when needed

and adds an extra level of flexibility for the designer. However, now the input actuation voltage cannot be applied directly to the main transistor gate since the transistor action will cause a feedthrough signal in addition to the piezoresistive motional current, overwhelming the resonant signal. For this reason, a split-gate finFET device was chosen for implementation, with one gate biased in accumulation for electromechanical transduction and the other creating an inverted channel for FET operation as shown in Figure 1.13. Such finFET devices have already been identified for use in future technology nodes making the RBT an ideal candidate for integration in sub-45 nm CMOS technologies. Using such a device structure, she was able to demonstrate a Q of roughly 1,830 at a resonant frequency of 11.7 GHz, the highest frequency mechanical resonance demonstrated on a silicon wafer to date.

However, the utility of such a device in aggressively-scaled finFET technology platforms remains to be seen. The finFET is a modification of the planar bulk MOSFET whose main emphasis is on alleviating the short-channel effects that have been plaguing planar bulk CMOS for digital applications. With the increasing push towards SoC integration, some groups have investigated the performance of these devices for RF applications and have found that there are some key drawbacks of using finFETs for high frequency operation when compared to bulk planar MOSFETs, particularly g_m degradation and larger parasitic capacitances and source/drain resistances [39]-[43]. In addition, the complex processing required for finFET technologies significantly increases cost, while the integration of good quality RF passives has not yet been investigated for such technologies, as their focus is primarily on digital systems. These questions must be addressed in the future to realize the full potential of the RBT for enabling true monolithic integration of RF systems.

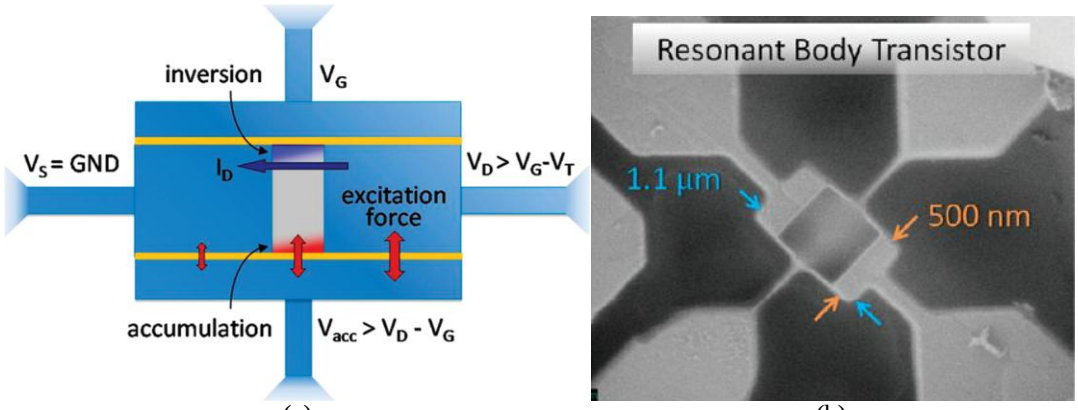

(a) (b)

Figure 1.13. (a) Device schematic and (b) SEM of resonant body transistor (RBT) operating at 11.7 GHz. Dual gate design based on FinFET geometry allows separation of the actuation gate biased in accumulation from the FET gate biased in inversion. Images reproduced from [37].

Based on the methods of FEOL integration presented here, it seems as though this approach to integration has some unique advantages in comparison with the other two strategies, particularly the ability to intimately couple both acoustic and electronic devices. In addition, different demonstrations have independently shown that this approach has the potential to address some of the main limitations of the other approaches, such as the need for additional processing steps or masks and limits on achievable frequency and *Q*. However, these demonstrations all used very different technology platforms ranging from BiCMOS to dual-poly CMOS to deep submicron finFET technologies. In order for the field of vibrating RF MEMS resonators to advance into a ubiquitous technology like CMOS, there needs to be a unification of methods and devices that are platform independent and can be easily parameterized and designed. This capability of CMOS, in addition to scaling, is the reason why it has become an irreplaceable part of our daily lives.

1.3 Research Goals and Dissertation Outline

Based on the previous discussion of the current needs for complete SoC

integration of RF transceivers with baseband signal processors and the myriad of different integration strategies that have been investigated, the goal of the research presented in this dissertation can be summarized as follows:

To identify and develop a high-Q, *UHF micromechanical resonator technology that can be integrated into a generic, mixed-signal (RF, analog, and digital) technology platform with a minimum number of extra processing steps and is intimately coupled to the electronic devices for efficient electromechanical transduction.*

The remainder of this dissertation is focused on addressing this goal. We start in Chapter 2 by exploring the idea of pn-diode internal transduction, a method which uses the electrostatic forces present in the depletion region of a reverse-biased diode to excite and detect acoustic resonance at gigahertz frequencies. In addition to the simplicity of such transduction methods, the ubiquity of pn-diodes in all semiconductor processes presents the possibility of integration in a variety of different platforms. We use a silicon-on-insulator (SOI) process which can be fully integrated into a generic SOI CMOS process without any modification to the front end. One of the benefits of integration into SOI CMOS is the fact that this technology has demonstrated superior transistor performance over bulk CMOS for both digital and analog/RF applications with improved on-chip isolation between noise sensitive analog/RF and noisy digital blocks and higher quality passives [44]. We present experimental results of a resonator employing this transduction mechanism with a record-setting frequency-quality factor (*f*-*Q*) product, a main figure of merit for RF resonators.

Due to the extremely high *Q* at gigahertz frequencies exhibited by these

resonators, an investigation into the intrinsic material limits of doped single-crystal silicon was conducted. This is discussed in detail in Chapter 3, and we find that at high enough frequencies, the conventional wisdom that *Q* is inversely proportional to frequency does not necessarily hold. We conducted an experimental investigation into the different phonon and electron scattering processes that may contribute to acoustic attenuation in degenerately doped single-crystal silicon and present a model identifying the dominant mechanisms across temperature and frequency.

In Chapter 4, we present the resonant junction transistor (RJT), which combines the high-*Q*, high frequency pn-diode transduction mechanism with the FET-sensing approach using a junction field effect transistor (JFET) for increased sensitivity and reduced parasitic feedthrough, in addition to other benefits provided by the use of JFETs. The theory of operation and fabrication of the device is presented and experimental results are discussed.

Finally, we conclude by discussing some future research directions based on the work presented in this dissertation. The path forward for monolithic integration of this technology into a commercial CMOS process is identified and remaining challenges as well as potentially new applications are discussed. The benefits of the technology presented in this work show that continued development may result in a very promising RF MEMS platform for addressing today's needs for high-quality integrated RF building blocks to implement tomorrow's complete SoC applications.

CHAPTER 2

PN-DIODE INTERNAL TRANSDUCTION

2.1 Solid Dielectric Transduction

The origins of electrostatic forces in capacitors lie in the electrical energy stored $U_E = ½CV^2$ between the capacitor plates. For most electrical calculations, the typical assumption is that the capacitor plates are fixed and that fringing fields can be ignored, in which case there is no mechanical response. However, when the capacitor plates are allowed to move, there is now a force applied to the capacitor plates given by the expression

$$\vec{F}_{es} = -\nabla U_E = -\frac{1}{2}V^2 \nabla C(\vec{x}) = -\frac{1}{2}\varepsilon_r \varepsilon_0 V^2 \nabla\left(\frac{A(\vec{x})}{g(\vec{x})}\right). \tag{1}$$

Imagine now that these plates are connected to a spring compliant in only the direction parallel to the electric field, as shown in Figure 2.1. In this case, A is constant and $g(x) = g_o - x$, and if we assume a small displacement x relative to the original gap width g_o (i.e., $x << g_o$), then

$$\vec{F}_{es} = \frac{1}{2}\frac{\varepsilon_r \varepsilon_0 A V^2}{g_o^2}. \tag{2}$$

If a sinusoidal input voltage v_{in} is added on top of a bias voltage V_{DC}, then this expression can be expanded as

$$\vec{F}_{es} = \frac{1}{2}\frac{\varepsilon_r \varepsilon_0 A}{g_o^2}\left(V_{DC}^2 + 2V_{DC}v_{in}e^{j\omega t} + v_{in}^2 e^{j2\omega t}\right). \tag{3}$$

We can see in (3) that electrostatic force components are generated at DC, the frequency of the input voltage, and also its second harmonic. Typically, this second harmonic voltage is very small and can be neglected. What remains then is a static force in addition to a component at the original input frequency, which is primarily of interest for resonator design. At this frequency, we can define what is called the

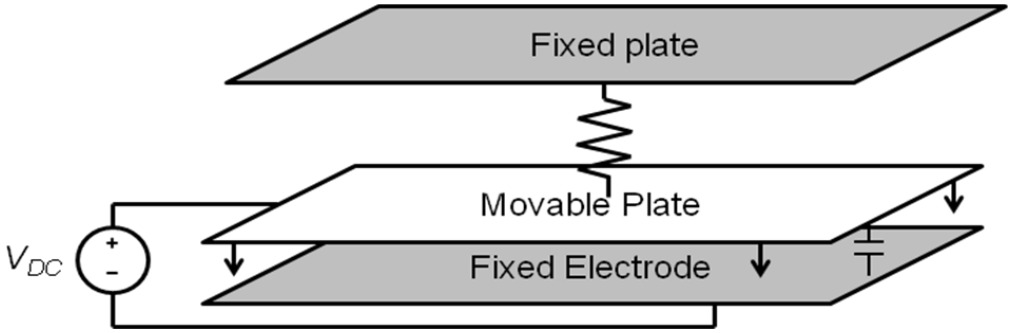

Figure 2.1. Schematic illustration of electrostatic (capacitive) actuation. Bottom capacitor plate is fixed while the top plate is connected to a spring compliant only in the *x*-direction (normal to the plates, parallel to the electric field).

electromechanical transduction efficiency of the actuation transducer η_a given in (4), which is the ratio of dynamic force generated in the structure over the input voltage amplitude.

$$\eta_a = \frac{\varepsilon_r \varepsilon_0 A V_{DC}}{g_o^2} \tag{4}$$

Similarly, the mechanical motion of the resonator can also be sensed by applying a DC bias voltage across an identical capacitor. In this case, the displacement current flowing through the capacitor is given by

$$i_{out} = \frac{d}{dt}(CV_{DC}) = V_{DC}\frac{dC}{dt}. \tag{5}$$

Again, if the capacitor places are fixed to a spring which restricts motion in all but the direction parallel to the electric field, then

$$i_{out} = V_{DC}\frac{dC(x)}{dx}\frac{dx}{dt} = V_{DC}\frac{\varepsilon_r \varepsilon_0 A}{g_o^2}\dot{x} \tag{6}$$

and the corresponding electromechanical transduction efficiency of the sensing transducer η_s defined as the ratio of the output motional current over the resonant velocity amplitude is

$$\eta_s = \frac{\varepsilon_r \varepsilon_0 A V_{DC}}{g_o^2} \tag{7}$$

What has just been described is the concept of electrostatic transduction of RF

MEMS resonators. Such electrostatically transduced resonators can use fully CMOS-compatible materials and manufacturing processes to realize high-Q resonance, making them promising candidates for integration into CMOS electronics, as mentioned in Chapter 1. Note in both (4) and (7) the dependence of the force on ε_r, the relative permittivity of the dielectric material. For air-gap electrostatic transduction, ε_r is simply equal to unity. However, if a material of higher permittivity could be used, then both the electrostatic force and output motional current could be boosted by a factor of ε_r, resulting in an overall reduction of motional impedance $R_X = v_{in}/i_{out}$, which is reduced by ε_r^2. This is the primary motivation for using solid dielectric films with higher relative permittivity in place of air-gaps. In addition, eliminating the narrow gaps typical in electrostatically actuated MEMS resonators provides other benefits, including robustness against contaminants, increased fabrication yield, and improved reliability. The first investigation of this so-called solid dielectric transduction for resonator applications was performed by Bouwstra in his seminal paper where he used a dielectric film to electrostatically actuate and sense acoustic resonance in a cantilever beam [45]. Since then, others have used dielectric films to actuate acoustic resonance in a variety of other ways which will be discussed here.

2.1.1 Poisson Effect Transduction

The derivation of the electrostatic force and output motional current in the previous subsection is valid under the assumption that the capacitor plates or edges of the dielectric film move uniformly in a direction normal to their surface. Thus, one might easily imagine using solid dielectric transduction for exciting bulk longitudinal resonant modes with the frequency determined by the dimension parallel to the

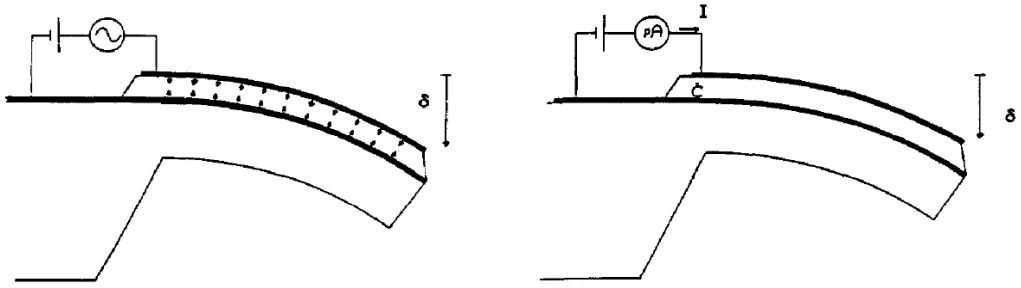

(a) (b)

Figure 2.2. Side view of silicon cantilever with silicon nitride solid dielectric transducer. Structure is both (a) actuated and (b) motional current is sensed through the use of Poisson effect transduction. Reproduced from [45].

displacement. However, exciting flexural resonant modes in something like a cantilever beam as in [45] is not as straightforward as placing a solid dielectric film between the electrode and resonating structure.

The method employed in [45] actually makes use of the Poisson effect, where strain is created in perpendicular directions when an initial strain in induced in one direction. The configuration used in this work is shown in Figure 2.2 and places the solid dielectric film sandwiched between two electrodes on top of the vibrating cantilever. As described in the previous subsection, when a DC bias voltage and AC input signal are applied across a solid dielectric film, an electrostatic force is created which compresses the film in the *z*-direction. Due to the Poisson effect, there is a strain and resulting stress which is also induced in the (isotropic) dielectric film in the *x*-direction. Since this stress is located close to the upper surface of the cantilever, it acts in much the same way as residual film stress resulting in beam bending [46], [47]. On the other hand, as the cantilever undergoes resonant motion, the dielectric film will be squeezed and distorted. When a DC bias is applied across the dielectric film, a motional current is detected at the output, in accordance with (5).

This work by Bouwstra illustrates the use of Poisson effect transduction to translate a stress in one direction to a perpendicular direction directly coupled to the

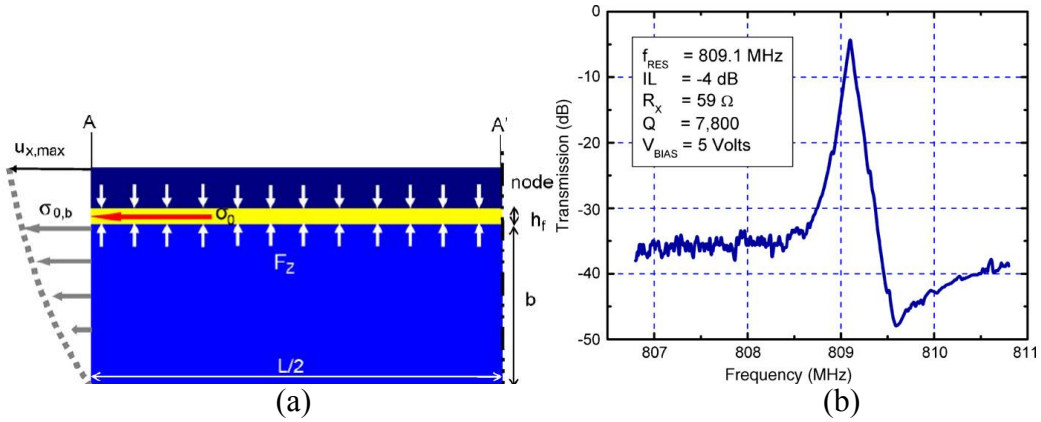

Figure 2.3. (a) Cross-sectional schematic of half-wavelength thickness shear silicon resonator showing the principle of operation using a silicon nitride solid dielectric transducer and (b) experimental results. Reproduced from [49].

resonant mode shape. In the case of [45], this was used to translate longitudinal dielectric stress in the thickness direction of the cantilever to an effective shear stress at the top of the cantilever acting in the axial direction. Other demonstrations of this transduction mechanism include work by Bhave and Howe [48] and Chandrahalim, Weinstein, and Bhave [49] where the first uses this method to excite contour modes in bar resonators at 120 MHz, while the latter work excites thickness shear modes at 723 MHz and 809 MHz with a similar resonator geometry and Q = 4,000-7,000. Experimental results from [49] are shown in Figure 2.3.

One thing to note is that while the expected ε_r^2 reduction in motional impedance is there, a penalty due to the Poisson ratio is also present. For example, for the thickness shear mode resonators in [49],

$$R_X \propto \frac{1-\nu_f}{\nu_f^2 \varepsilon_r^2}. \tag{13}$$

For a silicon resonator with silicon nitride dielectric transducer (ε_r = 7, ν_f = 0.22), we find that the expected motional impedance reduction is roughly a factor of 3, not the factor of 49 that is naively expected from considering only the relative permittivity. Still, even this 3× reduction is beneficial and, in many cases, when combined with other associated benefits of eliminating a narrow air-gap, may be worth it. But while

this method shows marked improvement at frequencies less than 1 GHz, some key features of this analysis may start to fail at higher frequencies. The key assumption under question here is how well the stress in the dielectric film is transferred to the rest of the resonant structure. Stoney's formula used to measure beam deflection for a given shear stress [47] is exact only for static beam deflection. For low enough frequencies, the error is negligible, but as frequency increases, this may no longer be true. In such cases, it is expected that acoustic mismatch will cause strange reflections at the boundaries between the dielectric and resonator material, significantly distorting the mode shape. Thus, opportunities for frequency scaling beyond 1 GHz are limited for this type of transduction scheme.

2.1.2 External Transduction

Due to the limitations of Poisson effect transduction, others have tried direct transduction of bulk longitudinal mode resonators by replacing the air-gap with a dielectric film such that the actuated stress is more strongly coupled to the mode shape. This was studied in detail by Lin and Nguyen by filling the air-gap of a 60 MHz wine-glass disk resonator with a 20 nm silicon nitride film, as shown in Figure 2.4 [50]. The resonant mode targeted in this work has boundary conditions similar to the case of an air-gap, specifically that the acoustic mode is largely confined to the original polysilicon material. In this scenario, the dielectric is effectively "outside" of the mechanical resonator, thus earning the name *external dielectric transduction*. In the case of an air-gap, the perfectly stress-free boundary condition reflects all waves back into the resonant structure. Of course, when a dielectric film is placed between the electrode and resonator, one would expect a non-zero amount of energy to be transmitted through the dielectric film and into the anchors, where it would be lost.

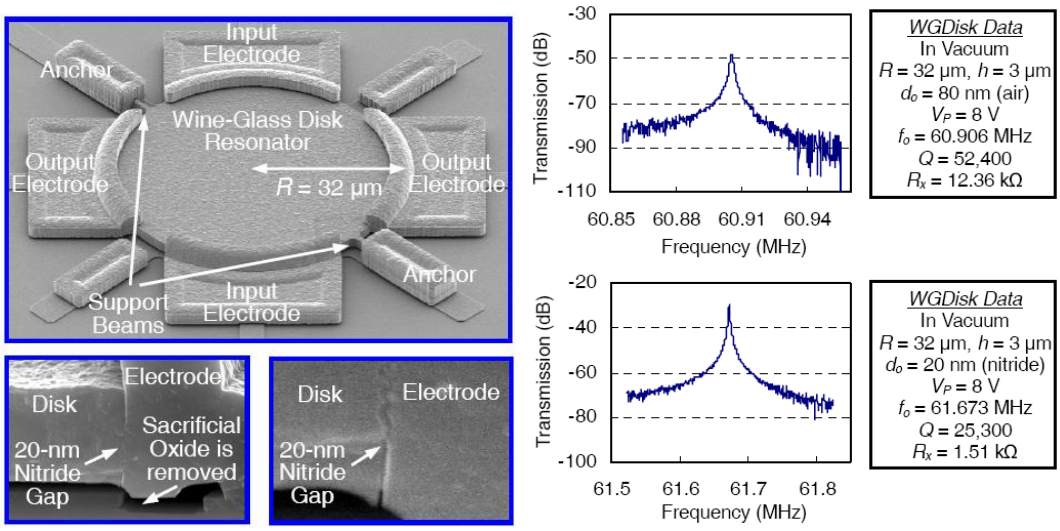

(a) (b)

Figure 2.4. (a) Top view and cross-sectional SEMs showing the polysilicon wine-glass disk resonator using solid nitride gaps for external dielectric transduction. (b) Experimental results for the polysilicon wine-glass disk resonators with conventional air-gap transduction (top) and solid nitride gap (bottom) for comparison. The frequency shift is relatively small, while the Q is decreased to half, yet the boost in efficiency due to the relatively permittivity results in an 8× improvement in motional impedance. Reproduced from [50].

One would also expect that the resonant amplitude be reduced.

Surprisingly, the small frequency shift and relatively small drop (~50%) in Q measured between air-gap transduced and dielectrically transduced 60 MHz disks seems to confirm that a decent portion of the elastic energy is confined to the original disk structure. The result is a factor of 8 improvement in the motional impedance, which is still much smaller than the expected ε_r^2 improvement and is a consequence of the reduction in resonant amplitude and imperfect boundary condition at the dielectric-resonator interface. These effects only become worse at higher frequencies, as discovered in work using 1 GHz wine glass rings [51]. Experimental results from this work show that the transmission amplitude between both air-gap and external dielectric transduction are nearly the same, indicating that any benefits from using a high permittivity transducer are non-existent. In fact, the motional impedances for both devices are so high that the resonant response can only be seen through mixing measurements. The effects of imperfect boundary conditions and constrained

amplitude become increasingly important for these higher frequencies and we see these penalties make external dielectric transduction too inefficient for practical use above 1 GHz.

2.1.3 Internal Transduction

The previous section shows that simply replacing the air-gap with a solid dielectric material is suboptimal in terms of transduction efficiency, especially at gigahertz frequencies. A large part of this, as discussed previously, is due to the suboptimal boundary conditions of the targeted resonant modes that arise by placing a solid material where there should be a stress-free boundary condition. A mathematically rigorous analysis would thus require the inclusion of the acoustic waves propagating in the film and into the electrode. In fact, if we are able to define a reasonable boundary condition for the opposite end of the *electrode*, which is now acoustically coupled to the vibrating body through the dielectric film, this whole composite structure including the dielectric may function as a resonator in itself. This incorporation of the dielectric film as part of the resonant structure is what distinguishes *internal dielectric transduction* from the external dielectric transduction introduced in the previous section. This concept was first demonstrated by Weinstein and Bhave [20] and shows some very interesting properties for actuating and sensing longitudinal bulk acoustic modes, specifically the increase in transduction efficiency with higher frequency. Figure 2.5 shows the structure used in this work where a free boundary condition is applied at that opposite end of the electrode, making it part of the vibrating structure.

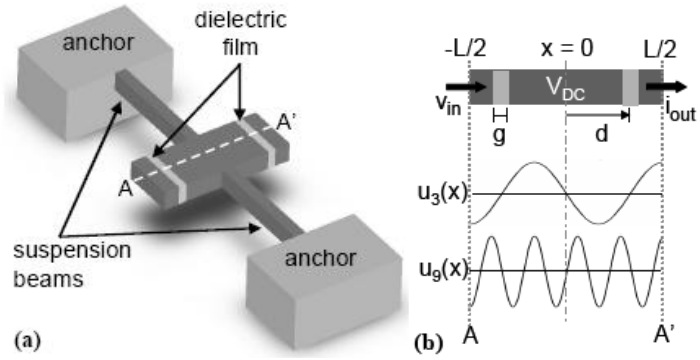

(a) (b)

Figure 2.5. (a) Illustration of internal dielectrically transduced resonator structure where electrodes are incorporated into the resonating body. (b) Side view of the vibrating structure with illustrations showing the resonant mode shape for the 3rd and 9th harmonics of the resonator. Reproduced from [20].

As previously discussed, when a voltage is applied to a solid dielectric parallel plate capacitor, a stress is induced in the dielectric film in the direction of the electric field. This can serve as the forcing input (right-hand side) in the equation of motion for a longitudinal bulk mode bar resonator shown in (14).

$$\rho A\frac{\partial^2 u(x,t)}{\partial t^2} - bA\frac{\partial^3 u(x,t)}{\partial t \partial x^2} - EA\frac{\partial^2 u(x,t)}{\partial x^2} = \frac{\partial F_{es}(x,t)}{\partial x} \tag{14}$$

Here, $u(x,t)$ is the displacement, ρ and E are the density and Young's modulus, respectively, of the resonator material, and A is the cross sectional area. Also, b is the damping factor of the resonator that is related to the Q. The DC component of F_{es} may be neglected here. This partial differential equation can be solved by guessing an initial solution, which for this case will be the sinusoidal mode shape of the resonator given by

$$u(x,t) = U_o \sin\left(\frac{n\pi x}{L}\right)e^{j\omega t}. \tag{15}$$

In this expression, n is the mode number of the longitudinal resonance. By substituting this solution into the equation of motion, the expression for the resonant amplitude U_o is given by

$$|U_o| = \frac{4Q\varepsilon_r\varepsilon_0 V_{DC} v_{in}}{n^2\pi^2 E}\frac{L}{g^2}\cos\left(\frac{n\pi d}{L}\right)\sin\left(\frac{n\pi}{L}\frac{g}{2}\right) \tag{16}$$

where d is the position of the center of the dielectric film relative to the center of the resonator body, g is the dielectric film thickness, and Q is the quality factor of the resonator. Here, the usual ε_r and $1/g^2$ dependence that is expected for the capacitive transducer is observed, but one should also note the additional sinusoidal terms that have parameters associated with the dielectric film in their arguments. These terms arise from the incorporation of the transduction dielectric film as part of the resonating structure.

An expression similar to (6) can be applied to find the output motional current, resulting in

$$\begin{aligned} i_{out} &= \frac{2\omega_{res}\varepsilon_r\varepsilon_0 V_{DC} A}{g^2}\cos\left(\frac{n\pi d}{L}\right)\sin\left(\frac{n\pi}{L}\frac{g}{2}\right)U_o \\ &= \frac{8Q(\varepsilon_r\varepsilon_0)^2 V_{DC}^2 A}{n\pi\sqrt{E\rho}\,g^4}\cos^2\left(\frac{n\pi d}{L}\right)\sin^2\left(\frac{n\pi}{L}\frac{g}{2}\right)v_{in} \end{aligned} \tag{17}$$

The final motional impedance R_X is then

$$R_X = \frac{n\pi\sqrt{E\rho}}{8Q(\varepsilon_r\varepsilon_0)^2 V_{DC}^2 A}\frac{g^4}{\cos^2\left(n\pi d/L\right)\sin^2\left(n\pi g/2L\right)} \tag{18}$$

A closer look at the cosine term in the denominator indicates that the optimal location for the dielectric film is at $d = (m/n)L$ where $m = 0,1,2,...n$. These locations correspond to displacement nodes of the mode shape. Figure 2.6(a) plots this dependence of motional impedance on the position of the dielectric within the resonator body along with experimental data and clearly illustrates the need to place the dielectric at these optimum points. In terms of the dielectric thickness, the strong dependence on g means that the thinnest possible dielectric films are desirable. This is limited by fabrication tolerances and other concerns such as breakdown voltage and reliability, etc. However, given the thinnest possible dielectric film, the second sine term indicates that at the frequency such that $g = L/n = \lambda/2 = c/(2f_{res})$ – where c is the

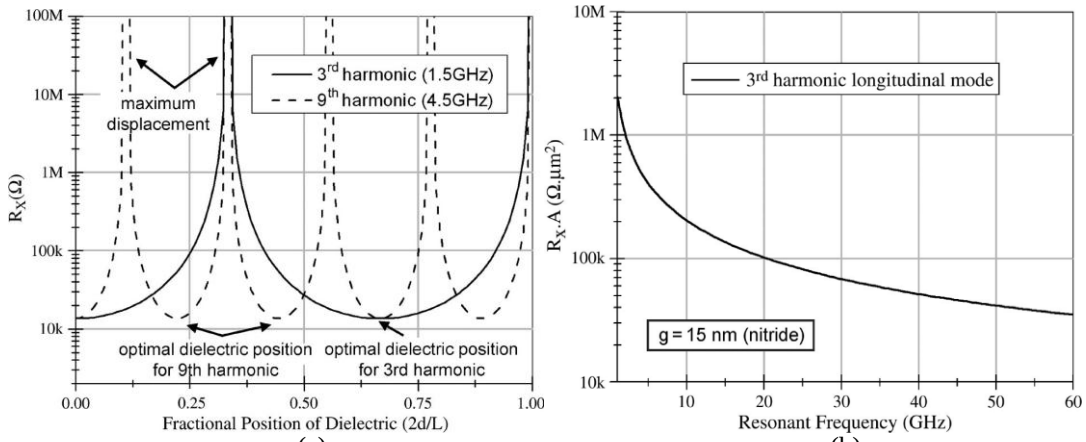

Figure 2.6. Motional impedance obtained using internal dielectric transduction using a silicon nitride embedded transducer as a function of (a) relative dielectric position and (b) resonant frequency for a given dielectric film thickness (15 nm). These plots show that dielectric transducer should be placed at displacement nodes for optimal transduction and that impedance decreases with frequency until acoustic half-wavelength is equal to the dielectric film thickness. Images reproduced from [38].

acoustic velocity in the dielectric film – R_X will be at a minimum, and that it will decrease monotonically with frequency up to the point where this equality holds. For 15 nm of silicon nitride as in [20], this comes out to 367 GHz. This is illustrated in Figure 2.6(b) showing both the scaling of motional impedance with frequency under the assumption of a constant *f-Q* product of 5×10^{13} Hz. Experimental data of two internally transduced silicon bar resonators – the first with a 3rd harmonic at 1.55 GHz and a 9th harmonic at 4.68 GHz, the second with a 3rd harmonic at 2.24 GHz and a 9th harmonic at 6.2 GHz – also shows that the transmission roughly increases with frequency, although the performance gains may not be quite as high as expected at the higher frequencies. This may be due to the fact that fabrication tolerances that shift the dielectric film from its optimal position become increasingly significant at higher frequencies because these small shifts constitute a larger fraction of the acoustic wavelength. What is important though is that the data seems to corroborate the general trend, verifying the utility of this method for efficient transduction in the UHF and SHF range.

While the data seems to corroborate the general trend, certain details are missing

from the initial analysis that may play a rather significant role in the actual motional impedance of these internal dielectrically transduced longitudinal bar resonators. One significant source of discrepancy between this theory and experimental results is the omission of acoustic mismatch between the dielectric transducer and surrounding resonator material. Here, we will provide the full analysis of this composite resonator structure using Green's function methods and discuss the effects of acoustic mismatch on the motional impedance of internal dielectrically transduced bulk mode resonators.

Figure 2.7 shows the structure of interest for this analysis. Regions 1 (resonator inner body) and 3 (electrode) are made of the resonator structural material; for this study, we will use silicon without loss of generality. Region 2 is the embedded dielectric film used for transduction via capacitive forces as discussed above. Due to the complexity of the analysis, we make a few simplifying assumptions to aid in the development of this theory. First, the structure shown in Figure 2.7 is only half of the bar resonator, with the left end corresponding to the center of the structure. We assume odd symmetry with respect to the center of the resonator due to anchoring (zero displacement at the center), allowing us to reduce the number of degrees of freedom to three spatial variables, x_1, x_2, x_3, each corresponding to the spatial variable within each region of the resonator (Figure 2.7). The resulting mode shapes are all odd-order harmonics of the fundamental, which is indeed the case for the resonator in [8]. In addition, we assume only 1-D longitudinal motion, which makes this analysis exact only for rectangular bar resonators where the 1-D approximation is valid ($L >> w, t$). The insight provided by this theory, however, should generally apply to similar composite longitudinal bulk-mode devices, like those in [52] and [53]. All effects of acoustic mismatch are compared against a baseline case which uses an acoustically

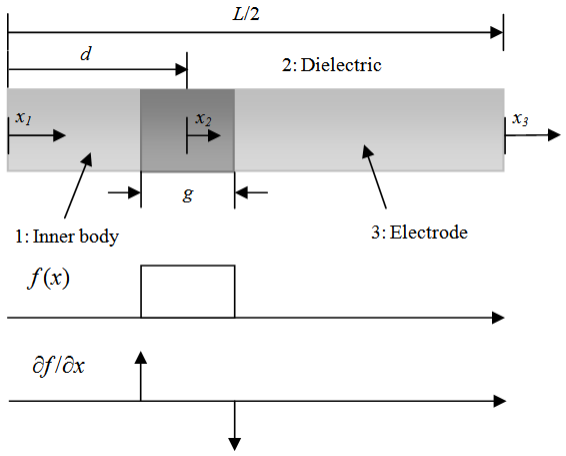

Figure 2.7. Illustration of composite resonator geometry and coordinate system used in the analysis of acoustic mismatch effects due to dielectric transducer layer. There are three distinct regions in the structure: the inner body, dielectric film, and electrode. The inner body and electrode are assumed to be made of silicon, while the dielectric film can be any material with arbitrary acoustic properties. The force *f*(*x*) and force distribution *df*/*dx* actuated by the dielectric film is shown below.

matched dielectric layer (i.e., Young's moduli and density of dielectric layer are equal to those of the structural layer) with a relative permittivity equal to that of nitride.

This analysis utilizes linearity to find the overall response of the system as the sum of Green's function solutions to the equations of motion in each region (similar to (14)) coupled through appropriate boundary conditions. These coupled inhomogeneous equations of motion are

$$\rho_{si}\frac{\partial^2 u_1(x_1,t)}{\partial t^2} - b_{si}\frac{\partial^3 u_1(x_1,t)}{\partial t \partial x_1^2} - E_{si}\frac{\partial^2 u_1(x_1,t)}{\partial x_1^2} = q_1(x_1,t) \tag{19}$$

$$\rho_{diel}\frac{\partial^2 u_2(x_2,t)}{\partial t^2} - b_{diel}\frac{\partial^3 u_2(x_2,t)}{\partial t \partial x_2^2} - E_{diel}\frac{\partial^2 u_2(x_2,t)}{\partial x_2^2} = q_2(x_2,t) \tag{20}$$

$$\rho_{si}\frac{\partial^2 u_3(x_3,t)}{\partial t^2} - b_{si}\frac{\partial^3 u_3(x_3,t)}{\partial t \partial x_3^2} - E_{si}\frac{\partial^2 u_3(x_3,t)}{\partial x_3^2} = q_3(x_3,t). \tag{21}$$

In the above equations, u_n are the solutions to the coupled forced wave equations within each region for input forcing functions $q_n = \partial f_n/\partial x_n$. The subscripts "*si*" and "*diel*" are used to distinguish between the material parameters for the structural material (silicon) of regions 1 and 3 and the dielectric film of region 2, respectively. As in the previous derivation, *E*, *b*, and ρ each represent the Young's modulus,

damping factor, and density, respectively. If we assume time harmonic excitation, then q_n and u_n can be expressed as

$$q_n(x_n,t) = Q_n(x_n)e^{-j\omega t}$$
$$u_n(x_n,t) = U_n(x_n)e^{-j\omega t} \tag{22}$$

This allows us to separate time-dependence from (19)-(21). Furthermore, if we define

$$Q_n(x_n) = \delta(x_n - \zeta_n), \tag{23}$$

where ζ_n is the point of excitation, then $U_n(x_n) \rightarrow G_n(x_n \mid \zeta_n)$, where G_n is the Green's function of the following coupled system of equations.

$$-\omega_{res}^2\rho_{si} - (E_{si} - j\omega b_{si})\frac{\partial^2 G_1(x_1 \mid \zeta_1)}{\partial x_1^2} = \delta(x_1 - \zeta_1) \tag{24}$$

$$-\omega_{res}^2\rho_{diel} - (E_{diel} - j\omega b_{diel})\frac{\partial^2 G_2(x_2 \mid \zeta_2)}{\partial x_2^2} = \delta(x_2 - \zeta_2) \tag{25}$$

$$-\omega_{res}^2\rho_{si} - (E_{si} - j\omega b_{si})\frac{\partial^2 G_3(x_3 \mid \zeta_3)}{\partial x_3^2} = \delta(x_3 - \zeta_3). \tag{26}$$

To find the resonant frequencies, we will first consider the case where the system is lossless, or $b_{si} = b_{diel} = 0$. This can be done since we are assuming that the loss in the system is relatively low and thus its impact on the resonant frequency is small. In this case, the general Green's function solution in each region is a sum of sine and cosine terms, where k_{diel} and k_{si} are the wavenumbers in region 2 and regions 1 and 3, respectively. We assume here that all regions have a linear dispersion relationship as given by (30).

$$G_{1,i}(x_1 \mid \zeta_1) = A_{1,i}(\zeta_1)\sin(k_{si}x_1) + B_{1,i}(\zeta_1)\cos(k_{si}x_1) \tag{27}$$

$$G_{2,i}(x_2 \mid \zeta_2) = A_{2,i}(\zeta_2)\sin(k_{diel}x_2) + B_{2,i}(\zeta_2)\cos(k_{diel}x_2) \tag{28}$$

$$G_{3,i}(x_3 \mid \zeta_3) = A_{3,i}(\zeta_3)\sin(k_{si}x_3) + B_{3,i}(\zeta_3)\cos(k_{si}x_3) \tag{29}$$

$$k_{si} = \frac{\omega}{c_{si}}, k_{diel} = \frac{\omega}{c_{diel}} \tag{30}$$

Here c_{si} and c_{diel} refer to the longitudinal acoustic velocities in regions 1, and region 2, respectively. Since the input forcing function we are concerned with consists of two delta functions, we employ the subscript i to specify the excitation location (either "left" or "right" for the force at the left dielectric interface or the right dielectric interface, respectively) that produces the corresponding Green's function. Obtaining the amplitude coefficients in (27)-(29) can be done by applying boundary and continuity conditions. The boundary and continuity conditions arising from the impulse on the left dielectric interface for a free resonator are given by

$$G_{1,left}(0) = 0 \tag{31}$$

$$\frac{dG_{3,left}}{dx_3}(0) = 0 \tag{32}$$

$$G_{1,left}(L_{body}) = G_{2,left}(-\frac{g}{2}) \tag{33}$$

$$G_{3,left}(-L_{elec}) = G_{2,left}(\frac{g}{2}) \tag{34}$$

$$E_{diel}\frac{dG_{2,left}}{dx_2}\bigg|_{x_2=-g/2} - E_{si}\frac{dG_{1,left}}{dx_1}\bigg|_{x_1=L_{body}} = -\frac{\varepsilon_r\varepsilon_0 V_{DC}}{g^2} \tag{35}$$

$$E_{si}\frac{dG_{3,left}}{dx_3}\bigg|_{x_3=-L_{elec}} - E_{diel}\frac{dG_{2,left}}{dx_2}\bigg|_{x_2=g/2} = 0 \tag{36}$$

Here, L_{body} and L_{elec} are used for brevity and refer to the length of the inner body (region 1) and the electrode (region 3), respectively. Specifically, $L_{body} = d - g/2$ and $L_{elec} = L/2 - d - g/2$. For an impulse on the right dielectric interface, (31)-(34) are still valid (with subscript "left" changed to "right'), but (35)-(36) change to (37)-(38).

$$E_{diel}\frac{dG_{2,right}}{dx_2}\bigg|_{x_2=-g/2} - E_{si}\frac{dG_{1,right}}{dx_1}\bigg|_{x_1=L_{body}} = 0 \tag{37}$$

$$E_{si}\frac{dG_{3,right}}{dx_3}\bigg|_{x_3=-L_{elec}} - E_{diel}\frac{dG_{2,right}}{dx_2}\bigg|_{x_2=g/2} = \frac{\varepsilon_r\varepsilon_0 V_{DC}}{g^2} \tag{38}$$

The results for each excitation are then summed to give the displacement U_n (x_n) in

each region

$$U_1(x_1) = G_{1,left} + G_{1,right} = A_1 \sin(k_{si} x_1) + B_1 \cos(k_{si} x_1) \tag{39}$$

$$U_2(x_2) = G_{2,left} + G_{2,right} = A_2 \sin(k_{si} x_2) + B_2 \cos(k_{si} x_2) \tag{40}$$

$$U_3(x_3) = G_{3,left} + G_{3,right} = A_3 \sin(k_{si} x_3) + B_3 \cos(k_{si} x_3) \tag{41}$$

The full expressions for the amplitude coefficients A_n and B_n in each region are long and on their own do not provide much insight. They are provided in the Appendix for the interested reader. However, there is one expression D shown in (42) which appears in common in the denominator of all expressions. For the lossless case, there will be values of ω such that $D(\omega) = 0$, at which the amplitude coefficients approach infinity. These values of ω correspond to the resonant frequencies of the system. The finite values of these coefficients at the resonant frequencies are found when loss is included in the system.

$$\begin{aligned} D = {} & \sin(k_{diel} g) \\ & \left[\frac{E_{diel}\rho_{diel}}{E_{si}\rho_{si}} \cos\left(k_{si}\left(\frac{g}{2} - \frac{L}{2} + d \right)\right) \sin\left(k_{si}\left(d - \frac{g}{2} \right)\right) - \sin\left(k_{si}\left(\frac{g}{2} - \frac{L}{2} + d \right)\right) \cos\left(k_{si}\left(d - \frac{g}{2} \right)\right)\right] \\ & - \sqrt{\frac{E_{diel}\rho_{diel}}{E_{si}\rho_{si}}} \cos(k_{diel} g) \cos\left(k_{si}\left(\frac{L}{2} - g \right)\right) \end{aligned} \tag{42}$$

In the limit that the dielectric layer and the resonator body material are acoustically matched, $k_{diel} = k_{si} = n\pi/L$, $E_{diel} = E_{si}$, and $\rho_{diel} = \rho_{si}$. The reader can verify that in this acoustically matched limit, the mode shape converges to a perfectly sinusoidal mode shape as predicted by [20], thus verifying that this theory converges to known behavior.

Now that the mode shapes are known, finding the motional impedance requires incorporating loss into the system. Previously, we had taken $b_{diel} = b_{si} = 0$, which

allowed us to choose sine and cosine solutions with purely real wavenumbers k in each region. With non-zero values for these loss coefficients, (24)-(26) indicate that the effective energy storage modulus (simply the Young's modulus for the lossless case) becomes complex. This means that the same general solution may be used, except k is now a complex wavenumber given by

$$k_{si} = \beta_{si} + j\alpha_{si},\ k_{diel} = \beta_{diel} + j\alpha_{diel} \tag{43}$$

$$\beta_{si} = \frac{\omega}{c_{si}}, \beta_{diel} = \frac{\omega}{c_{diel}}, \alpha_{si} = \frac{\omega^2 b_{si}}{2c_{si}E_{si}}, \alpha_{diel} = \frac{\omega^2 b_{diel}}{2c_{diel}E_{diel}}. \tag{44}$$

Here, β now signifies the wave propagation constant while α is a quantity that characterizes the loss per wavelength within the medium. For the following analysis, we will assume for simplicity that $b_{diel} = b_{si}$. Qualitatively, this means that for each acoustic wavelength traveled, a longitudinal plane wave traveling through the dielectric material will be attenuated by the same amount as a longitudinal plane wave traveling through silicon. Generally, the damping factor is highly material dependent, meaning $b_{si} \neq b_{diel}$. However, at low frequencies where the acoustic wavelength in the dielectric $\lambda_{diel} >> g$, we can assume that the difference in energy loss for acoustic waves traveling through the dielectric layer and the surrounding silicon is negligible. As a final note, notice that in the acoustically matched limit, $\beta_{si} = \beta_{diel} = \beta$ and $\alpha_{si} = \alpha_{diel} = \beta/2Q$, where Q is the quality factor of the resonance.

If we assume that the system is low loss (i.e., $E >> \omega b$), taking the series expansion of D shows that at the resonant frequencies of the system, all real terms in (42) cancel out, D becomes purely imaginary and the magnitude exhibits a local non-zero minimum. This magnitude determines the finite values of the coefficients in (39)-(41) Due to the complex nature of the above equations, finding an analytical expression for the magnitude is difficult. Therefore, numerical simulations in MATLAB were used to gain insight into the results of the preceding analysis. For the

numerical simulations, we introduce two parameters that characterize the acoustic mismatch between the two materials: r_E and r_ρ, defined as

$$r_E = \sqrt{\frac{E_{diel}}{E_{si}}},\ r_\rho = \sqrt{\frac{\rho_{diel}}{\rho_{si}}}. \tag{45}$$

The dependence of the motional impedance and resonant frequency on these parameters are found using simulations on a resonator with L = 12 μm, corresponding to a 3rd harmonic frequency of 1.067 GHz and an acoustic wavelength of 8 μm in a uniform silicon bar resonator.

First, we sweep the resonant frequency as a function of the dielectric position d and parameterize by both r_E and r_ρ, as shown in Figure 2.8. As a verification of our theory, we also use the finite element analysis software COMSOL to extract the resonant frequencies of resonators with the same dimensions as described above. This is done by repeatedly performing a modal analysis (which solves the coupled eigenvalue problem for each finite element of the specified geometry) on the resonator geometry while changing the dielectric position and the parameters r_E and r_ρ. The results of these COMSOL simulations are also included in Fig. 2.8 and show good agreement with the presented theory. We see from both these plots that the dependence on d is roughly sinusoidal with a wavelength equal to half that of the resonant wavelength in the resonator body. The average value and amplitude of the sinusoid is dependent upon r_E, r_ρ, and g. For $r_E > 1$ or $r_\rho < 1$, the resonant frequency increases with respect to the acoustically matched case ($r_E = r_\rho = 1$). This is expected since the resonator is effectively becoming stiffer or lighter. The opposite is true for $r_E < 1$ or $r_\rho > 1$. Also, as g increases, a larger portion of the resonator is affected by the acoustic mismatch, which explains the increase in frequency deviation with g.

Close inspection of Fig. 2.8(a) and (b) shows that at displacement nodes (d = 4 μm), the frequency varies minimally with r_ρ and maximally with r_E. The opposite is

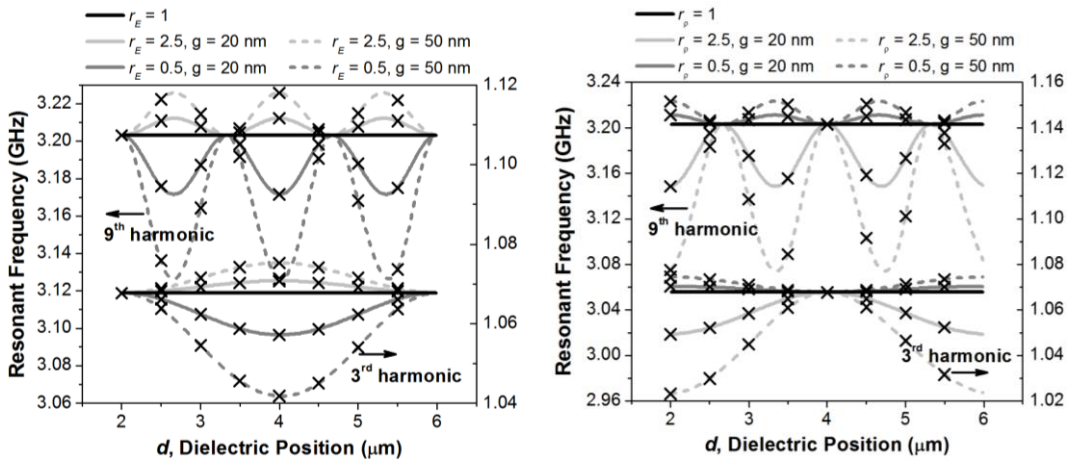

Figure 2.8. (a) f_o vs. d with r_ρ = 1 and different values of r_E and g for 3rd and 9th harmonics. (b) f_o vs. d with r_E = 1 and different values of r_ρ and g for 3rd and 9th harmonics. COMSOL simulation results are overlaid in X's.

also true at displacement maxima (d = 2 μm or 6 μm). This intuitively suggests that the dielectric film acts as a mass-spring system that couples the inner body and the electrode of the resonator.

A mechanical resonator can be modeled as a distributed network of infinitesimal masses and springs, just like a transmission line is modeled as a network of infinitesimal inductances and capacitances. Since we are assuming that $g << \lambda_{diel}$, we can model this whole system as two transmission lines representing the inner body and the electrode coupled by a mass-spring element, which represents the dielectric film.

This observation helps make sense of the numerical simulation results. At displacement nodes, the coupling mass does not contribute much since it does not move, while the coupling spring contribution is large since it is stretched maximally (i.e., maximum strain). On the other hand, at displacement maxima, the strain is minimal so the coupling spring contribution is small while the coupling mass contributes largely since it moves maximally. Note that this is only valid when the thickness of the dielectric film g is small compared to the acoustic wavelength of the dielectric film. Next, the motional impedance as a function of d and parameterized by

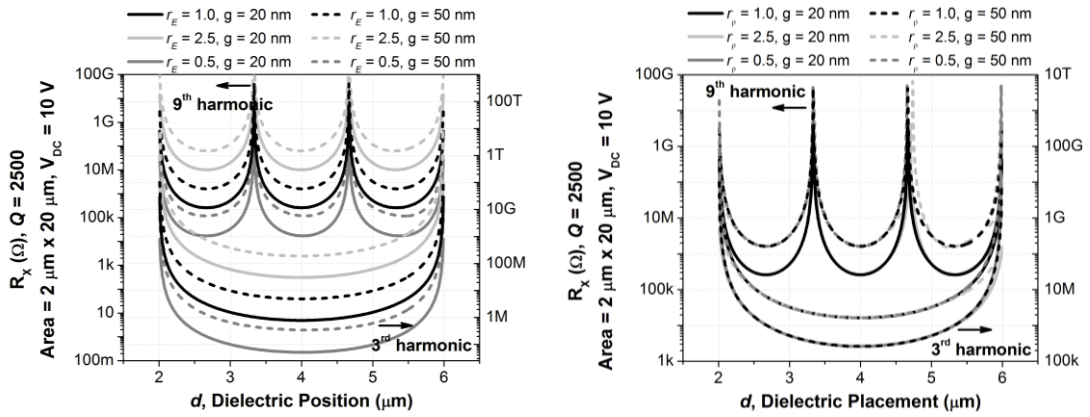

(a) (b)

Figure 2.9. (a) R_X vs. d with r_ρ = 1 and different values of r_E and g for 3rd and 9th harmonics. (b) R_X vs. d with r_E = 1 and different values of r_ρ and g for 3rd and 9th harmonics. Assumed parameter values are Q = 2500, Area = 20×2 μm^2, and V_{DC} = 10 V.

both r_E and r_ρ is plotted in Fig. 2.9 and shows a roughly $1/\sin^2(kd)$ dependence of motional impedance on d, much like what is described in [20]. These plots also reveal that the minimum motional impedance is a strong quartic function of r_E but remains roughly constant with r_ρ.

Closer examination of the motional impedance as a function of dielectric position shows that the minimum point of motional impedance depends on r_E and r_ρ. An analytical expression for this shift can be found by solving for the value of d that results in a maximum value of $U_2(-g/2) - U_2(g/2)$. After applying the simplifying assumptions previously stated (i.e., E_{si}, $E_{diel} >> \omega b$, $g << \lambda_{diel}$), a relatively simple expression for the shift in optimal dielectric position d_{opt} can be found. This expression is shown below in (46). Fig. 2.10 shows good agreement between the simulated optimal dielectric position and that predicted by (46). Note that roughness in the simulation results is due to resolution limits in the numerical simulation and improve with better frequency and spatial resolution at the cost of simulation time.

$$\frac{d_{opt,mismatch}}{d_{opt,ideal}} = \frac{1-\frac{g}{L}}{1-\frac{g}{L}\frac{E_{si}}{E_{diel}}} \frac{1-\frac{g}{2L}\frac{\rho_{diel}}{\rho_{si}}}{1-\frac{g}{2L}}. \tag{46}$$

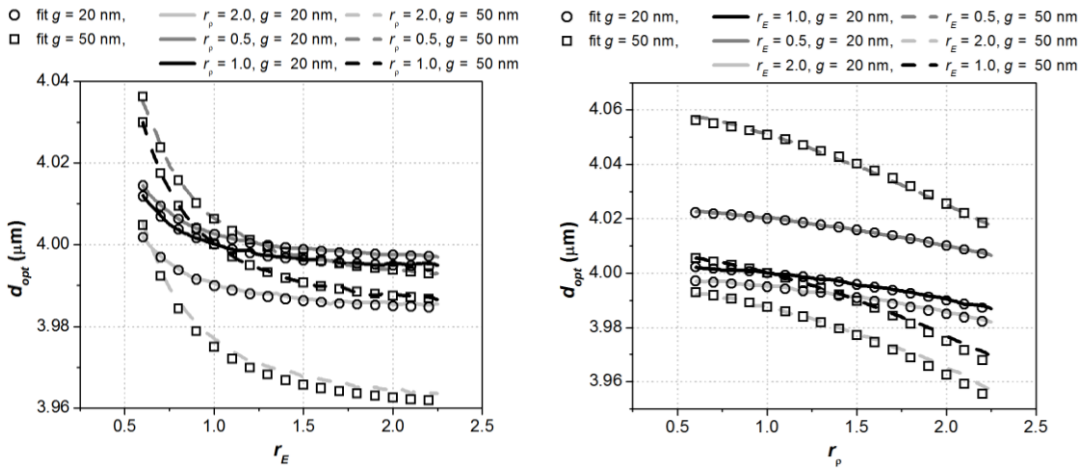

Figure 2.10. (a) d_{opt} vs. r_E with g = 20 nm for different values of r_ρ at 3rd harmonic. (b) d_{opt} vs. r_ρ with g = 20 nm for different values of r_E at 3rd harmonic. The optimal dielectric position for acoustically matched layers for this device geometry is 4 μm.

Finally, to provide insight into the effects of acoustic mismatch on practical devices, numerical simulations were also conducted on resonators using common dielectric materials such as nitride and hafnia. These results are shown in Fig. 2.11. As previously mentioned, since an optimally designed resonator should have the dielectric placed at a displacement node, only r_E contributes to the motional impedance for all practical purposes. Thus,

$$R_{X,mismatch} = \left(\frac{E_{diel}}{E_{si}} \right)^2 R_{X,ideal}. \tag{47}$$

Table 2.1 lists the minimum motional impedances for different dielectric films and resonator geometries. Here we see the significance of the r_E^4 dependence of motional impedance. Although nitride has a relative permittivity roughly twice as large as oxide, its use results in significantly higher motional impedance because it is extremely stiff. Using hafnia results in a lower impedance than what is obtained using oxide, but not nearly as low as expected if taking into account only the improvement due to higher relative permittivity. This indicates that acoustic mismatch effects, particularly the Young's modulus of the dielectric transducer material, together with

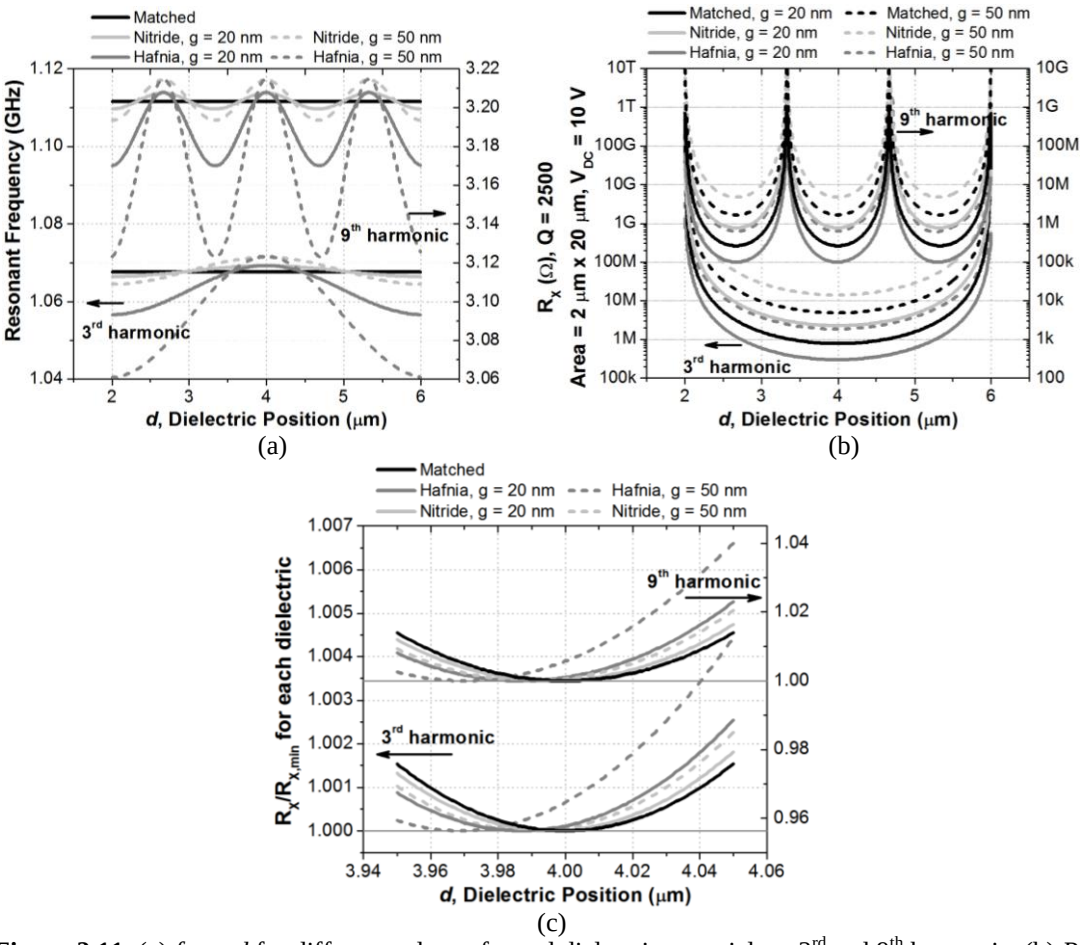

Figure 2.11. (a) f_o vs. d for different values of g and dielectric materials at 3rd and 9th harmonic. (b) R_X vs. d for different values of g and dielectric materials at 3rd and 9th harmonic. Assumed parameter values are Q = 2500, Area = 20×2 μm^2, and V_{DC} = 10 V. (c) Close-up view of normalized R_X for different dielectric materials.

the relative permittivity must be considered in choosing the optimal dielectric material.

In summary, we have seen that the method of internal dielectric transduction has great potential for CMOS-integrated longitudinal bulk mode acoustic resonators for a variety of reasons. From a practical standpoint, it is really possible to achieve such small transduction gap widths only by this method; etching 15 nm air-gaps for a 2.5 μm-thick silicon device layer (aspect ratio = 167) would be practically infeasible. This is important because the motional impedance is highly dependent upon this parameter.

Table 2.1. 3rd harmonic motional impedances for various dielectric materials assuming Q = 2,500, Area = 20×2 μm^2, and V_{DC} = 10 V.

Dielectric	g	d_{opt}	$R_{x,min}$
Acoustically Matched ε_{diel} = 7, E_{diel} = 170 GPa, ρ_{diel} = 2330 kg/m^3	20 nm	4 μm	781 kΩ
	50 nm	4 μm	4.88 MΩ
Si_3N_4 ε_{diel} = 7, E_{diel} = 290 GPa, ρ_{diel} = 3184 kg/m^3	20 nm	3.997 μm	2.27 MΩ
	50 nm	3.991 μm	14.1 MΩ
HfO_2 ε_{diel} = 20, E_{diel} = 300 GPa, ρ_{diel} = 9680 kg/m^3	20 nm	3.988 μm	297 kΩ
	50 nm	3.968 μm	1.85 MΩ
SiO_2 ε_{diel} = 4, E_{diel} = 66 GPa, ρ_{diel} = 2270 kg/m^3	20 nm	4.009 μm	367 kΩ
	50 nm	4.026 μm	2.36 MΩ

In addition, the relative permittivity of the dielectric reduces the motional impedance as well. Other benefits which are more practical in nature include increased robustness to contaminants and higher manufacturing yield. Finally, and perhaps most importantly, this method of transduction provides a path for scaling resonators into the UHF and SHF range due to their interesting property where the motional impedance decreases with frequency.

However, there are drawbacks to incorporation of the dielectric film in the resonator body. As presented in this section, inefficiencies resulting from acoustic mismatch act to cancel out some of the reduction of motional impedance predicted in the ideal case. In addition, defects at the interface between the dielectric film and resonator material may increase acoustic losses and limit Q [54]. More significantly, however, power handling and field reliability become practical issues with the use of a thin dielectric film. As the dielectric film thickness is scaled to smaller dimensions, the breakdown voltage of the film also decreases, limiting both the applicable DC bias

voltage and also the maximum input AC voltage signal. This breakdown is permanent, creating pinholes in the dielectric and making the device useless after such an event occurs. Closely related to this is the susceptibility to electrostatic discharge (ESD), which also increases as the dielectric film thickness decreases. Such issues must be addressed before deployment in practical electrical systems.

2.2 Theory of pn-Diode Internal Transduction

If there existed a method to take advantage of all the benefits of internal dielectric transduction without having to use a dielectric film, many of the drawbacks associated with this method could be mitigated. Fortunately, a device that exhibits charge storage behavior like a capacitor without requiring a separate dielectric material between the two electrodes is found everywhere in any semiconductor process: the simple (reverse-biased) pn-junction diode. These devices are very well characterized and highly controllable in most integrated circuit processes, thus making them ideal candidates for implementing internal transduction for CMOS-integrated high frequency micromechanical resonators. In fact, the use of diodes for electromechanical transduction has been demonstrated before. Examples include work by Ransley and Seshia using gold-silicon Schottky diodes to actuate flexural vibrations in cantilever beams [55] and investigation of the electrostrictive coefficients of silicon by Sterkenburg [56]. These demonstrations were all limited to very low frequency (~10 kHz) and used inefficient placement of the transducer based on the forthcoming analysis. The purpose here is to make use of the internally embedded nature of pn-diodes to efficiently transduction of UHF RF MEMS resonators.

Many of the reliability issues that affect dielectrically transduced resonators are now greatly mitigated with the use of pn-junctions for electromechanical transduction.

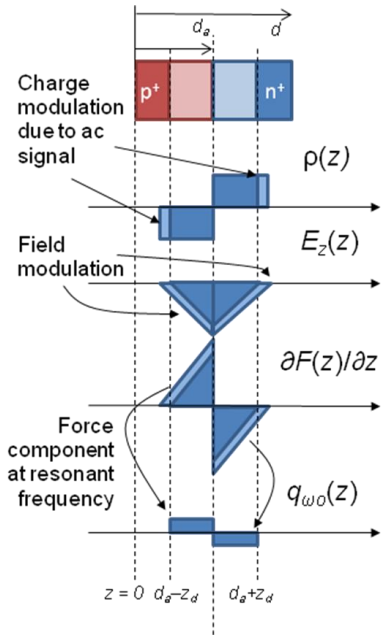

Figure 2.12. Illustration of principle of actuation in the input junction showing the charge density ρ, electric field in the thickness direction E_z, and force component at resonant frequency $q_{\omega o}$ throughout the structure.

Breakdown of these diodes is caused by either Zener or avalanche breakdown, both of which are completely reversible processes. In addition, resonators transduced in this way can be composed of only a single, homogeneous material (e.g., single-crystal silicon), which eliminates acoustic mismatch non-idealities and Q degradation due to interfaces and allows full exploitation of low acoustic loss materials to achieve high Q. Here, we will present the full theory on how replacing the dielectric film with a reverse-biased pn-junction diode will affect the transduction properties and will derive a self-consistent model with equivalent Butterworth-Van Dyke (BVD) circuit model for easy incorporation into circuit simulations.

2.2.1 Actuation

Figure 2.12 shows a pn-diode embedded in a silicon structure with the frequency defining dimension now labeled as d and the junction location is labeled as d_a. This notation is used since the device demonstrating this concept uses a thickness-

extensional (i.e., FBAR) mode. The configuration for the junction is similar to that of the embedded dielectric film for internal dielectrically transduced resonators. To find the actuated resonant amplitude, we must first find the force distribution within the resonator body. This force distribution arises from the electrostatic force acting on the immobile charge (i.e., donor/acceptor ions) within the depletion region of the pn-junction, as shown in Figure 2.12. Assuming an abrupt symmetric junction profile, the expressions for the charge distribution $\rho(z)$, electric field $E_z(z)$, and the force distribution $\partial F/\partial z$ are given by

$$\rho(z)=\begin{cases}-eN_a, & d_a - z_{d,a} < z < d_a \\ eN_a, & d_a < z < d_a + z_{d,a}\end{cases} \tag{48}$$

$$E_z(z)=\begin{cases}-\dfrac{eN_a}{\varepsilon_{si}\varepsilon_0}\left(z_{d,a} - d_a + z\right), & d_a - z_{d,a} < z < d_a \\ \dfrac{eN_a}{\varepsilon_{si}\varepsilon_0}\left(z - z_{d,a} - d_a\right), & d_a < z < d_a + z_{d,a}\end{cases} \tag{49}$$

$$\frac{\partial F}{\partial z}=\begin{cases}-\dfrac{e^2 N_a^2 A_{j,a}}{\varepsilon_{si}\varepsilon_0}\left(z_{d,a} - d_a + z\right), & d_a - z_{d,a} < z < d_a \\ \dfrac{e^2 N_a^2 A_{j,a}}{\varepsilon_{si}\varepsilon_0}\left(z - z_{d,a} - d_a\right), & d_a < z < d_a + z_{d,a}\end{cases}. \tag{50}$$

where e is the elementary charge, N_a is the symmetric junction doping concentration, ε_{si} is the relative permittivity of silicon, ε_0 is the permittivity of free space, $A_{j,a}$ is the junction area, and $2z_{d,a}$ is the junction depletion width given by the expression

$$z_{d,a}(v_{in})=\sqrt{\frac{\varepsilon_{si}\varepsilon_0}{eN_a}\left[\phi_{bi,a} - (V_{DC,a} + v_{in}e^{j\omega t})\right]} \tag{51}$$

where $\Phi_{bi,a}$ is the junction built-in voltage. The subscript 'a' in these expressions indicates that the corresponding parameter is relevant to the actuation junction. Eqs. (48)-(51) indicate that this function is nonlinear with the input voltage v_{in}. If $v_{in} << \Phi_{bi} - V_{DC}$, then (48) can be linearized around the bias point, yielding a distributed force at the excitation frequency given by

$$q_{\omega_o} = \begin{cases} -\dfrac{(eN_a)^{3/2} A_{j,a}}{2\sqrt{\varepsilon_{si}\varepsilon_0(\phi_{bi,a} - V_{DC,a})}} v_{in}, & d_a - z_{d,a} < z < d_a \\ \dfrac{(eN_a)^{3/2} A_{j,a}}{2\sqrt{\varepsilon_{si}\varepsilon_0(\phi_{bi,a} - V_{DC,a})}} v_{in}, & d_a < z < d_a + z_{d,a} \end{cases} . \tag{52}$$

This force distribution yields the following equation of motion replaces the expression on the right hand side of the equation of motion for the longitudinal bulk acoustic mode resonator given by (14) Note that there is a difference between $A_{j,a}$ in the above expressions and A in (14); the former is the cross-sectional area of the actuation junction, while the latter is the cross-sectional area of the resonant structure. These two parameters are not necessarily the same, as is the case for the structure which is used as a demonstration of this transduction mechanism. This actually requires that the structure is two-dimensional, thus a more accurate model would need to include this extra degree of freedom. This, however, complicates the analysis significantly without yielding any additional insight into the different design parameters and therefore will not be considered. In any case, all theories regarding 2-D plates are all numerical due to their complexity which makes it hard to find a closed-form solution [57].

Finally, by solving the equation of motion using (52) as the input forcing function, we obtain the electromechanical transduction efficiency for the actuation junction

$$\eta_a = \frac{2dA_{j,a}}{n\pi} \frac{eN_a}{z_{d0,a}} \sin\left(\frac{n\pi d_a}{d}\right) \sin^2\left(\frac{n\pi}{d}\frac{z_{d0,a}}{2}\right) \tag{53}$$

where $z_{d0,a} = z_{d,a}(v_{in} = 0)$. The resonant amplitude is given by

$$|U_o| = \frac{4Qd^2}{n^3\pi^3 E} \frac{A_{j,a}}{A} \frac{eN_a}{z_{d0,a}} \sin\left(\frac{n\pi d_a}{d}\right) \sin^2\left(\frac{n\pi}{d}\frac{z_{d0,a}}{2}\right) v_{in}. \tag{54}$$

It should be noted that this analysis assumes that the movement of charge at the edges of the depletion region is dominated by the response of majority carriers, i.e. the junction is in reverse-bias. This is because the movement of minority carriers is too slow to adequately respond to input voltages at high frequencies. To analyze the

behavior in forward bias, an equivalent shunt conductance can be added to model the minority carrier response time as an RC time constant, if necessary. This, however, will not be considered here.

Eq. (54) has a few similarities with (16), particularly in the sinusoidal dependencies on junction location and depletion width. Like (16), (54) indicates that the optimal junction location is at a displacement node and the second sinusoidal term shows that the same increase in efficiency with frequency also occurs in this transducer. There are a few differences, however, due primarily to the fact that the depletion width is not fixed, as is the thickness of the dielectric film. In fact, (51) shows that it actually increases with reverse bias voltage and relative permittivity, which is why the dependence on these parameters is also different. This can be more readily seen if we simplify (54) and (16) assuming that $2z_{d0,a}$, $g << \lambda/2$ and that the junction is optimally placed. The results are shown below in (55) and (56).

$$\left|U_o\right|_{pn-diode} = \frac{Q}{n\pi E}\frac{A_{j,a}}{A}\sqrt{eN_a\varepsilon_{si}\varepsilon_0(\phi_{bi,a} - V_{DC,a})}v_{in}. \tag{55}$$

$$\left|U_o\right|_{dielectric} = \frac{2Q}{n\pi E}\frac{1}{g}\varepsilon_r\varepsilon_0 V_{DC}v_{in} \tag{56}$$

We see that both these expressions increase with greater bias voltage and relative permittivity, but the square root dependence in (55) is due to the fact that the effective "gap" also increases according to a square root with these parameters. Otherwise, the functional forms are very similar.

2.2.2 Sensing

The sensing mechanism employed in this work is fundamentally electrostatic, therefore one may be quick to assume that (5) and (6) apply directly without further consideration. This scenario, however, is exact when there is a physical separation

(i.e., dielectric layer) across which charge is accumulated. In this case, the flow of charge is easy to account for: since $Q = CV$ and because C is changed due to the physical extension or contraction of the gap size, when the voltage is held constant charge will flow in or out and reside on the plates of the parallel capacitor accordingly. This is not exactly the case for the proposed device, which has a depletion layer across which charge can still move. This subtlety slightly complicates the analysis, but surprisingly, it still results in a model that is mathematically consistent with the simple capacitive sensing model of (5) and (6) using the depletion capacitance of the junction instead of a parallel plate capacitance. We will first present the simplified calculations and then explore the subtleties that exist for the proposed device.

Expanding (5) under the assumption that the depletion capacitance at the output behaves like a physical capacitance, the expression for motional current becomes,

$$|U_o| = \frac{\omega \varepsilon_{si} \varepsilon_0 (\phi_{bi,s} - V_{DC,s}) A_{j,s}}{2 z_{d0,s}^2} U_o \sin\left(\frac{n\pi d_s}{d}\right) \sin\left(\frac{n\pi z_{d0,s}}{d}\right). \tag{57}$$

Here, the parameters are all similar to the case of the actuation junction, except that the "*s*" subscript indicates that these are parameters of the sensing junction. The electromechanical transduction efficiency of the sensing junction is now

$$\eta_s = \frac{\varepsilon_{si} \varepsilon_0 (\phi_{bi,s} - V_{DC,s}) A_{j,s}}{2 z_{d0,s}^2} \sin\left(\frac{n\pi d_s}{d}\right) \sin\left(\frac{n\pi z_{d0,s}}{d}\right). \tag{58}$$

Again, as in the theory of actuation, this analysis assumes that the distribution of free carriers at the edges of the depletion region respond instantaneously to changes in the capacitance, which would indeed be the case for an actual parallel plate capacitance. Similarly, this requires the junction to be reverse-biased.

As mentioned above, however, a full derivation requires looking at the actual movement of charge across the junction. For this analysis, we will again assume the instantaneous response of free carriers to the input stimulus – in this case the stress – allowing us to consider this as an adiabatic system. In addition, we will assume that

the voltage across the junction is held constant at a value *V*. By observing how the stress changes the immobile charge density and thus the diffusion and drift current components across the junction, we will find an expression for the output motional current.

We start by considering the case of compressive stress, where the silicon lattice is squeezed. A qualitative picture of the process is shown in Figure 2.13. Fig. 2.13(a) shows the band diagram of the initial unstrained junction. All four current components are annotated in this diagram. As shown in the diagram, $J_{n,drift}$ and $J_{p.drift}$ are the current components resulting from the movement of thermally generated minority carriers on each side within the diffusion length of the depletion region edge. These carriers then drift across the junction due to the electric field. There also exist $J_{n,diff}$ and $J_{p,diff}$, which are the current components that arise as a result of majority carriers on each side that overcome the potential barrier and diffuse across the junction. These carriers become minority carriers and recombine on the other side of the junction.

When the stress is applied, the immobile charge density now changes. Since we are considering what happens adiabatically, we can imagine that at the exact moment that the strain compresses the junction, the free carriers have not yet responded. Thus, the depletion region width initially stays constant but because of the underlying compression of the ions in the lattice, we expect the charge density and subsequently the electric field to now increase within the depletion region. This will increase the barrier height to a value V', as indicated by the dashed line in Figure 2.13(b). As the barrier increases, $J_{n,drift}$ and $J_{p,drift}$ also increase, resulting in a negative current across the junction. Once these minority carriers cross the junction, they become majority carriers, which define the depletion region width. At this moment, if the potential across the junction were allowed to vary, then the compressive stress would simply increase the effective doping density and the depletion region width would remain

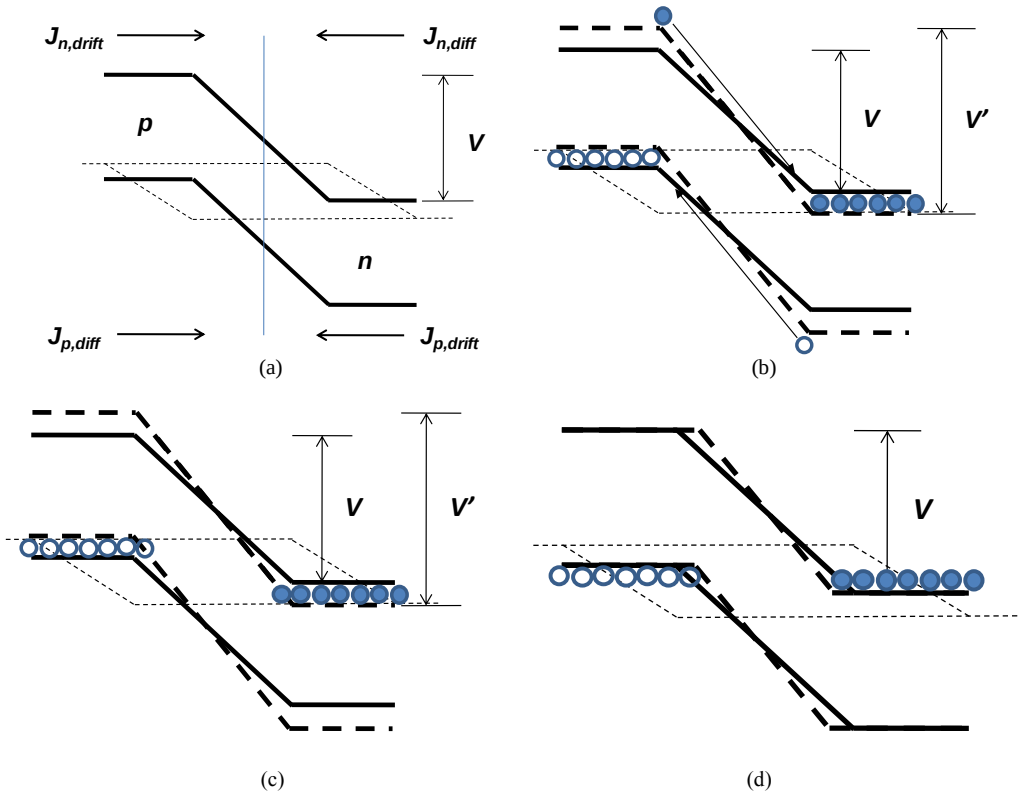

Figure. 2.13. (a) Band diagram of unstrained pn-junction showing individual current components. (b) Compressive strain in the junction causes an increase in the dopant density, subsequently increasing the electric field and the barrier height. This causes the current components $J_{n,drift}$, $J_{p,drift}$ to increase while decreasing $J_{n,diff}$, $J_{p,diff}$. The result is a net movement of electrons to the n-side and holes to the p-side. (c) The excess carriers become majority carriers when they cross the junction and (d) there return the system to the original barrier height.

constant. The total static current across the junction would be the quantity that increases. However, this is where the fact that the potential across the junction is forced constant by a voltage source becomes important. In this case, the system will try to restore the barrier height to *V* and the increased negative currents would allow this to happen by using the newly available majority carriers to decrease the depletion region width and thus the electric field. When the barrier height is restored to *V*, then the currents will return to the original value expected for the corresponding bias. In contrast to the case where the potential were allowed to vary freely, the quantity that permanently changes is now the depletion region width.

The case of tensile strain is exactly the opposite in that the immobile charge density effectively decreases, resulting in a decrease in the barrier height and thus an

increase in the $J_{n,diff}$ and $J_{p,diff}$ components. Again, since the voltage across the junction is held constant, the movement of charge provides a means for the system to readjust the depletion width to return to the original potential. This process is not illustrated here for the sake of brevity.

We can quantitatively analyze the effect of strain on the change in depletion width by considering the amount of immobile charge within the depletion region and finding how much this width must change in order to accommodate the same voltage. First, we must consider how the strain changes the immobile charge density. If we consider an infinitesimal section of the depletion region *dz* and the charge within this region *dQ*, we can observe that

$$dz' = dz(1+\varepsilon(z)) \tag{59}$$

$$dQ = N_{s0}A_{j,s}dz = N_s(z)A_{j,s}dz' \tag{60}$$

$$N_s(z) = \frac{N_{s0}}{1+\varepsilon(z)} \approx .N_{s0}(1-\varepsilon(z)) \tag{61}$$

where $\varepsilon(z)$ is the strain and N_{so} is the doping density – i.e., the original immobile charge density. The last simplification is made possible by assuming a small strain ($\varepsilon(z) << 1$).

The total potential across the unstrained junction is given by the following expression

$$V = \int_{-z_{d,s}}^{+z_{d,s}} \vec{E}_z \bullet \vec{dl} \tag{62}$$

The electric field here is described by (49). Likewise, the potential across the strained junction is given by

$$V = \int_{-z_{d,s}'}^{+z_{d,s}'} \vec{E}_{z,strained} \bullet \vec{dl} \tag{63}$$

and in this case, $E_{z,strained}$ is equivalent to (15) with N_{so} replaced by $N_s(z)$ and $z_{d,s}$

replaced by the new strained depletion width $z_{d,s}$'. Since the potential across both the unstrained and strained junctions must be equal, we can then set (62) and (63) equal and solve for $z_{d,s}$' in terms of $z_{d,s}$. If we assume that the maximum displacement amplitude is much less than the wavelength (i.e., $\varepsilon(z) << \lambda/d$), then we obtain the rather interesting result that

$$z_{d,s}' = z_{d,s}(1 + \varepsilon(z_{d,s})) \tag{64}$$

This expression for $z_{d,s}$' indicates that the new depletion width is just the original depletion width changed by the amount of strain at the depletion width edge. In other words, we can think of the edges of the depletion width mimicking the movement of the charge accumulation layers (i.e., capacitor plates) of a parallel plate capacitor. This result justifies the use of the simple capacitive model previously mentioned for the case of reverse bias and small strain, allowing easy modeling of the proposed resonator.

With this understanding, we can develop an equivalent BVD circuit model shown in Figure 2.14. The expressions for the motional impedance, inductance, and capacitance are well-known and can be expressed in terms of previous determined parameters

$$R_X = \frac{n\pi A\sqrt{E\rho}}{2Q}\frac{1}{\eta_a \eta_s} \tag{65}$$

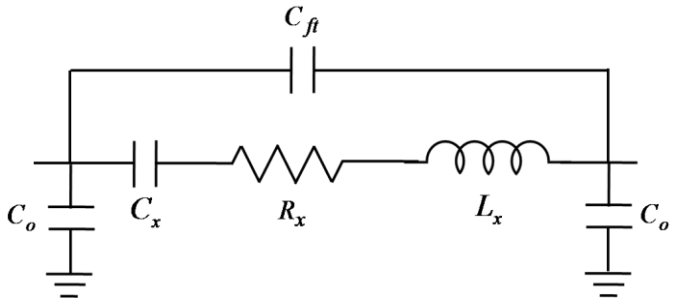

Figure 2.14. Equivalent Butterworth-Van Dyke circuit model of the proposed pn-diode internally transduced resonator in a two-port configuration.

$$L_X = \frac{\rho A d}{2} \frac{1}{\eta_a \eta_s} \tag{66}$$

$$C_X = \frac{2d}{n^2 \pi^2 AE} \frac{1}{\eta_a \eta_s} \tag{67}$$

In addition to these series resonant circuit components, there is a direct feedthrough capacitance C_{ft}, usually due to fringing fields and there are also two shunt capacitors at the input and output, which are equivalent to the junction depletion capacitances

$$C_{0,a} = \sqrt{\frac{\varepsilon_{si} \varepsilon_0 e N_a A_{j,a}}{4(\phi_{bi,a} - V_{DC,a})}} \tag{68}$$

$$C_{0,s} = \sqrt{\frac{\varepsilon_{si} \varepsilon_0 e N_s A_{j,s}}{4(\phi_{bi,s} - V_{DC,s})}} \tag{69}$$

At this point, one note should be made on the effect of asymmetric doping. In conventional semiconductor processes, it is difficult to achieve perfectly symmetric doping profiles, especially for the high doping concentrations required for efficient transduction in the proposed device. This doping asymmetry will undoubtedly have some effect on the transduction efficiency of the pn-diode transduced resonators. A detailed analysis will be omitted for brevity but a look at Figure 2.11 illustrates what will happen as the doping concentration becomes more and more asymmetric. As the doping asymmetry increases, the charge density, electric field, and force distribution will all approach a very tall and thin distribution in the highly doped semiconductor, while the depletion region will extend far into the lightly doped semiconductor. In the extreme case of a Schottky junction, the result will be an almost delta function force distribution exactly at the metallurgical junction. For such a junction, the optimal location will now be at a displacement maxima (i.e., edges of the resonator for the current device) and even at the optimal junction location, the efficiency will be decreased. Furthermore, the benefits associated with internal transduction will no longer be seen since the force distribution looks much like that of an externally transduced air-gap resonator. However, this is only in the case of extremely

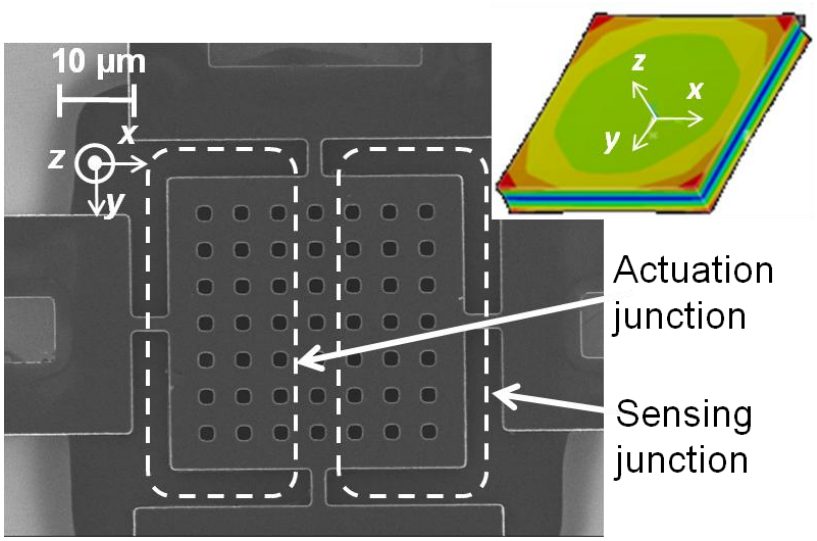

Figure 2.15. SEM of the 40 µm × 40 µm pn-diode transduced micromechanical resonator. The resonant frequency of 3.72 GHz is determined by the silicon device layer thickness (no electrodes or other mass loading layers). The thickness extensional mode shape (contours represent displacement in the *z*-direction) is shown in the inset plot. Etch holes are required for timed HF release.

asymmetric doping; for the doping asymmetries that can be achieved through careful process characterization, the overall effect will be a slight reduction in transducer efficiency and shift of the optimal junction location. Our results will show that even though asymmetric doping will decrease performance, we are still able to demonstrate a relatively low motional impedance device using conventional semiconductor processes.

2.3 Fabrication Process

In order to validate the theory of pn-diode internal transduction presented in this dissertation, we fabricated single-crystal silicon thickness extensional mode (FBAR mode) resonators. An SEM of the fabricated device is shown in Figure 2.15 with an inset showing the simulated mode shape in ANSYS. Device fabrication was performed at the Cornell Nanoscale Science and Technology Facility (CNF) following

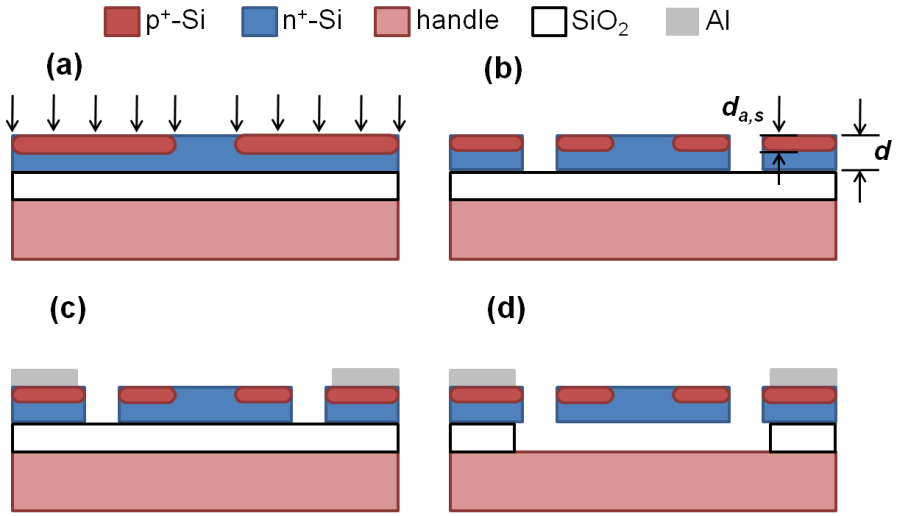

Figure 2.16. (a) The 1.3 μm device layer of an SOI wafer is selectively doped using boron implantation and annealed to achieve the desired junction depth of 0.65 μm. (b) The device layer is etched to define the resonator and pads. (c) Aluminum is deposited and etched to define the interconnect and pad structure. (d) The device layer is released via timed HF etch.

the steps outlined in Figure 2.16. Another benefit of pn-diode internal transduction is its very simple fabrication process. Furthermore, all process steps can find equivalent steps in a typical SOI CMOS process, making it possible to fabricate such devices in an integrated platform without additional masks and complicated post-CMOS processing steps.

Initially, we start with a custom n^+ doped SOI wafer with 1.3 μm thick, (100)-oriented device layer of resistivity < 0.006 Ω-cm. The device layer is then selectively doped using boron ion implantation and a photoresist mask to define the actuation and sensing junctions and create ohmic contacts to metal interconnects. The photoresist is removed via hot solvent bath and a subsequent rapid thermal anneal (300°C load temperature, 20 second ramp to 1100°C for 15 second soak) is performed for dopant activation and to create the junction at the desired depth of 0.65 μm with a roughly symmetric dopant concentration of 1×10^{19} cm^{-3}. This is followed by a reactive ion etch of the device layer using an oxide hard mask to define the resonator and anchors.

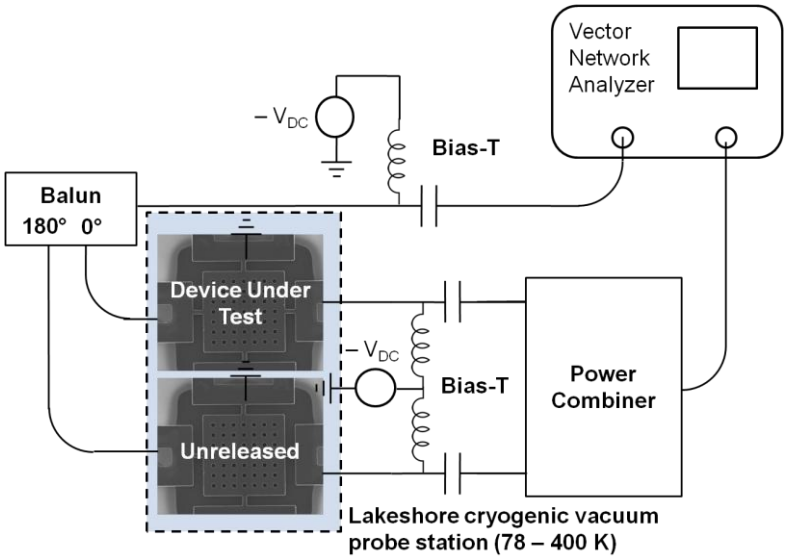

Figure 2.17. Pseudo-differential measurement setup to effectively characterize the mechanical resonance of the pn-diode transduced resonator by reducing capacitive loading.

Interconnect and pad structures are defined by sputter deposition and wet etching of 50 nm Cr (for adhesion and to prevent spiking) and 100 nm Al with photoresist mask. The device is finally released using a timed HF etch with a photoresist protective layer to prevent exposure of Al to HF, immediately followed by a critical point drying step to prevent stiction.

2.4 Experimental Setup and Results

The experimental setup used to make measurements of the pn-diode transduced resonators is shown in Figure 2.17. We utilize a pseudo-differential measurement technique by simultaneously driving out-of-phase an identical unreleased resonator fabricated next to the device under test [58]. This is done to eliminate the loading effects of feedthrough parasitics and to accurately measure the mechanical resonance. In this case, the feedthrough path consists of capacitance C_{ft} in Figure 2.14 and also

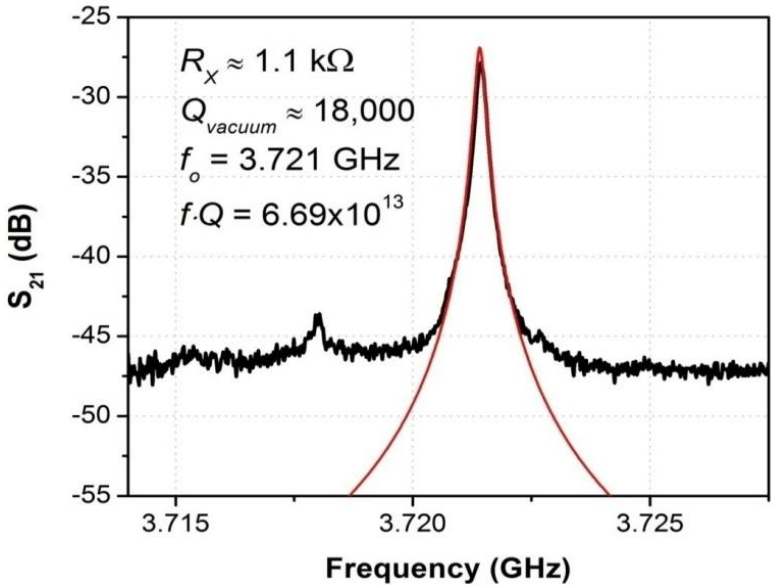

Figure 2.18. Measured S_{21} showing clear resonant peak with Q = 18,000 at approximately 3.72 GHz, resulting in an f-Q product of 6.69×10^{13} Hz and a motional impedance of 1.1 kΩ. Red line shows fit using equivalent circuit model and (65)-(67).

includes some contribution from the shunt capacitors since there is a finite routing resistance through the tethers to the ground plane.

The transmission magnitude is shown in Figure 2.18, indicating a mechanical quality factor of approximately 18,000 in vacuum for the fundamental mode. The motional impedance of this particular device is 1.1 kΩ and the f-Q product is 6.69×10^{13} Hz. The overlaid curve is the transmission response predicted using the equivalent circuit model shown in Fig. 2.13. A few parameters were allowed to vary in order to fit the data, in particular the device layer thickness and doping concentration. The values used, however, were well within the specified manufacturer tolerances for the device layer thickness (±0.5 μm) and the fabrication tolerances for the tools in the CNF. Other than the device shown here, we have successfully measured at least six other resonators all demonstrating $R_X < 2$ kΩ and $Q > 17{,}500$, highlighting the robustness of the proposed resonator to process variations. For these seven resonators, the frequency spread was about 24 MHz with an average frequency of roughly 3.718

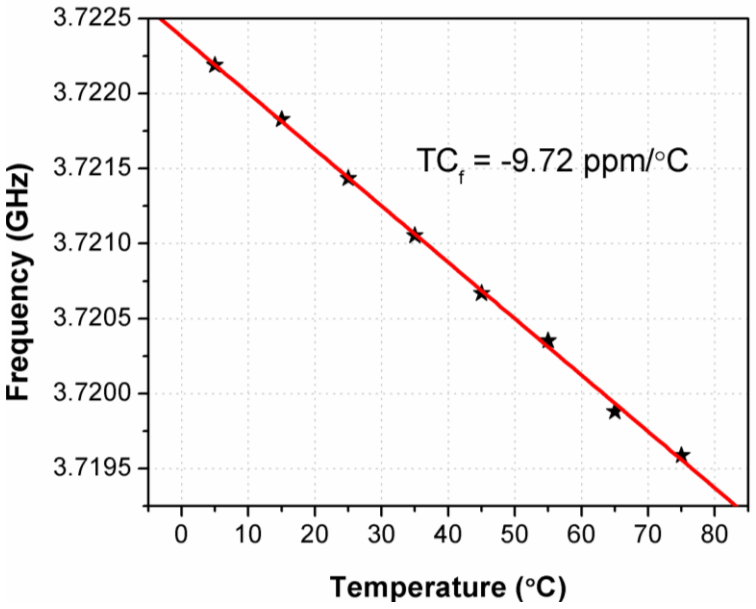

Figure 2.19. Resonant frequency as a function of temperature. This figure shows a linear dependence with a temperature coefficient of -9.72 ppm/°C over a temperature range of 5 - 75°C.

GHz, indicating a 0.65% spread in the resonant frequency across devices, which is illustrated in Figure 2.18. This can be improved by using SOI wafers with tighter device layer thickness tolerances.

We have also performed temperature measurements ranging from 5 - 75°C to determine the temperature sensitivity of the pn-diode transduced resonators. Figure 2.19 shows that the temperature coefficient of frequency (TC_f) in this temperature range is -9.72 ppm/°C, which is about a factor of 3 lower than that of typical silicon micromechanical resonators. This can be attributed largely to the effect of degenerate doping on the elastic constants of semiconductors, as discussed in [59].

Figure 2.20 shows a plot of the $f \cdot Q$ product of previously published high Q electrostatically transduced micromechanical resonators in addition to that of this work. The theoretical limit predicted by phonon-phonon dissipation [60] is indicated by the black curve, showing that this work approaches this limit. The resulting $f \cdot Q$ product is the highest ever reported in a silicon micromechanical resonator to date,

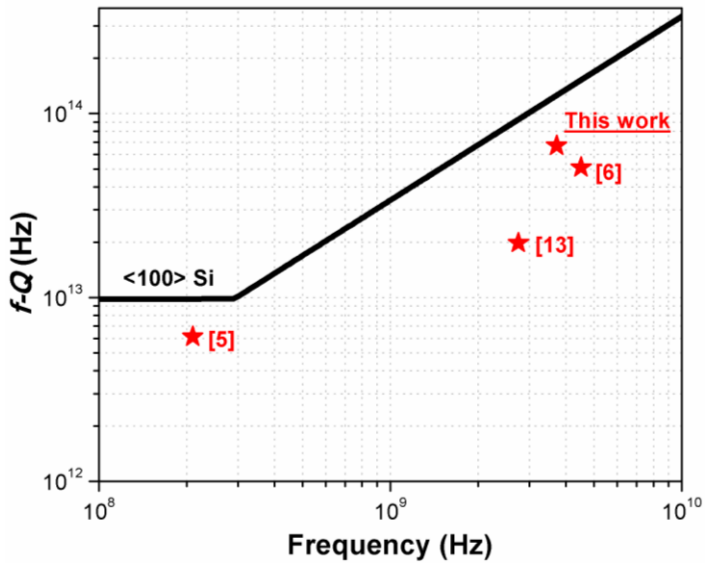

Figure 2.20. The $f{\cdot}Q$ product of previously published high Q micromechanical resonators shown in comparison to the theoretical limit for phonon-phonon scattering in (100)-Si (black line) from [18]. This work results in a value of 6.69×10^{13} Hz, which is approximately half of the theoretical value at 3.72 GHz.

demonstrating the feasibility of robust, ultra-high Q resonators in the UHF range integrated into a CMOS chip.

CHAPTER 3

STUDY OF INTRINSIC ACOUSTIC LOSSES IN UHF MEMS RESONATORS

3.1 Motivation

Due to the unique ability to efficiently excite resonance at frequencies exceeding 1 GHz without a separate transducer material, pn-diode internal transduction extends the operating frequency of micromechanical resonators to the UHF and SHF range while still achieving Q > 10,000. This was demonstrated using single-crystal silicon in the previous chapter to tap into the known low intrinsic acoustic attenuation of this material and demonstrate f-Q products approaching the material limit. While this capability is useful for achieving high-Q UHF resonators for narrow-bandwidth filters and low-phase noise frequency references, it is also valuable from a more theoretical standpoint since it allows us to directly investigate the acoustic loss mechanisms of semiconductor materials at these frequencies. The thickness extensional resonators presented in the previous chapter are particularly well-suited for investigating these intrinsic mechanisms since anchor losses are reduced due to Poisson ratio reduction of the longitudinal stress in the tethers.

In this chapter, we present experimental results of the temperature dependence of the mechanical Q of multi-GHz silicon longitudinal acoustic resonators, which allow us to peek into the dominant loss mechanisms most relevant for CMOS-integrated UHF MEMS resonators. We then fit the experimental data based on known theories of acoustic attenuation in doped semiconductors [61]-[65] and thus verify the impact of various acoustic loss mechanisms, which will be introduced in the following subsections, on resonator Q over a wide temperature range. This will provide insight into the practically achievable Q for UHF silicon MEMS resonators both at room and

cryogenic temperatures, having implications for a wide range of applications from filters and frequency references to quantum limited detection and ground state preparation, which have become topics of interest in the physics community as of late [66], [67].

3.2 Mechanisms of Acoustic Attenuation and Relationship to Q

Acoustic attenuation in micromechanical resonators is due to a number of mechanisms which can generally be grouped into two categories: extrinsic and intrinsic losses. Extrinsic losses are defined as losses that occur because of radiation of acoustic energy into regions outside of the main resonating structure. Such losses include acoustic energy lost through support structures (e.g., anchors, tethers, etc.) or friction caused by gas viscosity. These losses due to friction with the surrounding gas (typically air) are significant for lower frequency flexural mode but for higher frequency bulk acoustic modes, they become less important [68]. The reason for this is typically due to the smaller displacement and larger dynamic stiffness at higher frequency. For this reason, this source of acoustic damping will not be considered in this dissertation.

On the other hand, intrinsic losses are those that are due to friction or viscosity in the crystal lattice of the material itself. One such mechanism is what is known as thermoelastic dissipation (TED), originally postulated and experimentally verified by Zener [69], [70]. Due to the build-up of standing acoustic waves in the resonator structure, different regions of the resonator are simultaneously under tension or compression, resulting in heating or cooling of these regions. This causes an increase in entropy of the system and heat flow between these different regions. When the mechanical resonant mode is such that the resultant temperature distribution coincides

with a particular thermal eigenmode of the structure, the thermal and mechanical behavior of the resonator become strongly coupled, thus leading to temperature-induced forces which must be included in the equation of motion. Solving this system of equations allows one to find the theoretical Q limited by TED. The thermal relaxation time τ_{TED}, which is effectively the time it takes for the system to reach thermal equilibrium after perturbation, is very important in this formulation. It is when the mechanical resonant frequency coincides with this value $1/\tau_{TED}$ that the heat flow is maximized and the Q is minimized. Previous work has used this understanding to boost the Q of double-ended tuning fork resonators by increasing τ_{TED} via disrupting heat flow through slits in the resonant structure [71] or by offsetting the thermal eigenmodes from the mechanical ones by inducing static temperature gradients in the structure [72]. These methods are effective in boosting the Q for lower frequency flexural mode resonators where TED is dominant. It has been determined, however, that TED is relatively insignificant in bulk mode resonators [73], so it will also not be discussed here in depth.

Although TED does also appear in a quantum mechanical formulation based on the phonon Boltzmann transport equation [63], the initial derivation by Zener was based completely on classical theory. This is possible because of the long time and length scales involved with both flexural modes and heat transport. Other intrinsic acoustic attenuation methods such as phonon-phonon dissipation and phonon-electron dissipation, however, are concerned with the interactions between acoustic waves and other quasi-particles in the crystal lattice on length scales where quantum considerations become necessary, at least in the consideration of thermal phonons. These mechanisms will be discussed in detail in the next section. It will be shown that at room temperature, the phonon-phonon dissipation mechanism is the main intrinsic Q-limiting factor for silicon micromechanical resonators operating at frequencies

greater than 1 GHz.

Much of the experimental work on internal friction and acoustic attenuation in the literature are based on traveling bulk acoustic waves inside an acoustic delay line using a piezoelectric transducer with a calibrated power input [74], [75]. The power of the wave is then measured at the opposite end of the line, which determines the attenuation constant $\alpha(\omega)$, typically given in dB/cm or Np/cm. This attenuation constant is directly related to Q by the expression

$$Q = 2\pi \frac{\text{Energy stored}}{\text{Energy dissipated per cycle}} = \frac{\omega}{2\alpha(\omega)c_{acoustic}} \tag{70}$$

where $c_{acousitc}$ is the appropriate acoustic wave velocity and $\alpha(\omega)$ in this expression is in Np/cm. Using this expression, we can find the expressions for theoretically obtainable Q due to each loss mechanism. The total Q of the system can then be found by

$$\frac{1}{Q_{total}} = \frac{1}{Q_{ph-ph}} + \frac{1}{Q_{anchor}} + \frac{1}{Q_{TED}} + \ldots = \sum_i \frac{1}{Q_i}. \tag{71}$$

We shall see that different Q_i are significant at different frequencies and temperatures and knowing the unique characteristics of each will allow us to identify the significant acoustic loss mechanisms in UHF silicon MEMS resonators.

3.3 Phonon-phonon Scattering Mechanisms

The concept of phonons is a quantum mechanical description of the normal modes of a lattice, which are vibrational eigenmodes of a crystal lattice found by modeling the atoms and their interatomic potentials as mass-spring systems. Phonons are bosons, meaning that their equilibrium distribution follows Bose-Einstein statistics:

$$\langle n \rangle = \frac{1}{e^{\hbar\omega(\mathbf{q},m)/k_B T} - 1}, \tag{72}$$

and each one carries energy equal to $E = \hbar\omega(\mathbf{q},m)$, where $\hbar$ is the reduced Planck constant, k_B is the Boltzmann constant, T is the temperature, and $\omega(\mathbf{q},m)$ is the frequency of a normal mode with wavevector $\mathbf{q}$ and mode m, which will be discussed in more detail in the following subsection. Just as photons are quanta of light energy, phonons are quanta of elastic energy and by the same analogy may also be considered as quasi-particles. In any case, (72) indicates that phonon occupation and thus the behavior of phonon systems will depend strongly on temperature. In fact, the heat conduction properties of most common materials near room temperature are dominated by phonon processes. This is important to note, since phonon-phonon scattering can be described in two separate regimes depending on the interaction between the excited acoustic wave in the resonator and the thermal phonons which carry most of the thermodynamic energy of the system. But before we go into further detail regarding the specific mechanisms of phonon-phonon acoustic attenuation, we must understand the link between the seemingly macroscopic phenomenon of acoustic waves and the quantum mechanical concept of phonons.

3.3.1 Acoustic Waves and Phonons

As previously discussed, modeling the crystal lattice of a material as a mass-spring system yields the vibrational eigenmodes of the lattice, which are called the lattice normal modes. These normal modes are important because they form the basis for describing any arbitrary lattice vibration. By solving the coupled equations of motion assuming this basis, we are able to find the dispersion relation between the frequency of the normal mode ω and the wavevector $\mathbf{q}$. In a three dimensional lattice with monatomic basis, there are in fact three independent types of lattice vibrations that can

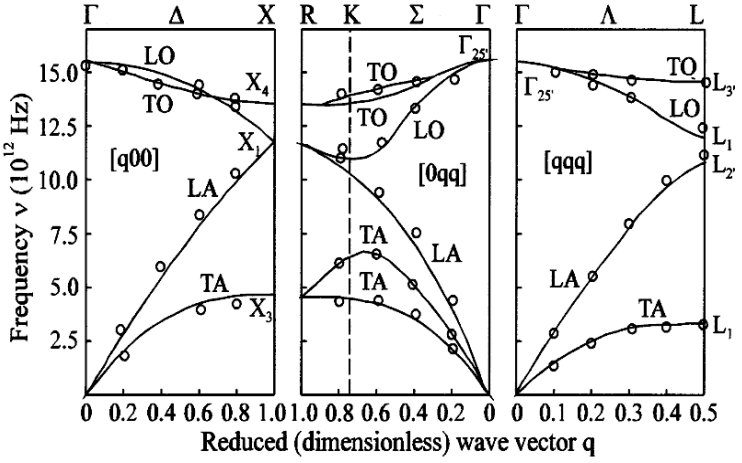

Figure 3.1. Full phonon dispersion curves in different orientations in k-space. The acoustic phonon modes are characterized by zero frequency at **q** = 0. For low frequencies, the acoustic phonon dispersion is nearly linear with slope equal to the acoustic wave velocity for the corresponding acoustic mode and orientation. Reproduced from [76].

exist: two transverse and one longitudinal. The discrete parameter '*m*' (for mode) will be assigned to distinguish between the three modes as they arise in equations, as in (72). Specifically, $m = 1$ indicates a longitudinal mode and $m = 2, 3$ indicate either one of the transverse modes. Each of these three modes has a different dispersion relation, making the frequency of a particular normal mode a function of both **q** and *m*.

In a material with a diatomic basis like silicon, each type of mode that was just described can now support an additional degree of freedom for a total of six distinct phonon modes ($m = 1$ to 6). This is illustrated more clearly in Figure 3.1 which shows the full phonon dispersion relation of silicon [76]. We see two distinct types of branches: three (some are degenerate in certain directions) that start at $\omega = 0$ for $\mathbf{q} = 0$ and another three that have $\omega \neq 0$ for $\mathbf{q} = 0$. The first set of modes is named the acoustic phonon modes since they are actually lattice sound waves, as we shall see later. They have a linear dispersion relation for small **q** (i.e., long wavelength) and can exist at frequencies of concern for mechanical resonators and thermodynamic phenomenon. In fact, acoustic phonons with $\omega \sim 1.6k_BT/\hbar$ (10 THz in silicon at 300 K) are the primary carriers of thermal energy and can mostly account for the

thermodynamic behavior of materials [77]. The second set of modes is the optical phonon modes. They are named so due to their mode shapes, where atoms within the same basis move in opposite directions, creating a time-varying electrical dipole moment. This property makes them easily excitable using infrared photons. While these phonon modes have their own very interesting properties, they are of little consequence for micromechanical resonators and therefore will not be discussed in further detail.

Again looking at the long-wavelength acoustic phonon modes near $\mathbf{q} = 0$, it becomes apparent that the motion of the atoms in these modes exactly corresponds to those of bulk acoustic waves in mechanical resonators. In fact, the dispersion relations for all acoustic phonon modes are relatively linear with phase and group velocities equal to the bulk acoustic wave speed of the particular mode. These observations yield insight into the nature of excited bulk acoustic waves: they are simply single lattice excitations (distinct ω and m) with a number of *coherent* phonons in much larger quantities than would exist at thermal equilibrium. In micromechanical resonators, this coherence is ensured at the desired frequency by geometry and appropriate boundary conditions which ensure that the reflected phonons add in phase, in addition to excitation by a coherent source. From a quantum mechanical standpoint then, acoustic attenuation is really just any process that results in a reduction of coherent phonons, either by reducing their number or by reducing their coherence. For $\omega_{acoustic} << k_B T/\hbar$, which is true even for silicon resonators operating at up to 20 GHz at temperatures as low as 10 K, this phenomenon can be described in two distinct regimes based on whether or not the bulk acoustic wave interaction with the surrounding lattice must be considered quantum mechanically. These two regimes will be discussed in the following subsections.

3.3.2 Landau-Rumer Regime

As a continuation of the previous discussion linking acoustic waves and phonons, we present here a scenario where we consider such phonons constituting a bulk acoustic wave as quasi-particles. A simple analogy that can then explain the scattering of acoustic wave phonons to phonons of different modes and frequencies is the classic example of the scattering of billiard balls. Phonons of an acoustic wave – each with energy $\hbar\omega_{acoustic}(\mathbf{q}_{\mathbf{acoustic}},m_{acoustic})$ – traveling through a lattice can be thought of as shooting a cue ball (acoustic wave phonon) into a table full of moving billiard balls (thermally excited phonons, mostly at $\omega_{thermal} \sim k_B T/\hbar$). Omitting for now certain selection rules that limit the interaction between phonons of specific modes and frequencies, these billiard balls are free to collide with each other and the cue ball. Eventually, the cue ball will collide with another moving ball, changing its energy and momentum. By direct analogy, the original acoustic wave phonon after a collision with thermal phonons will now end up with an energy $\hbar\omega'(\mathbf{q}',m')$ and is thus no longer a phonon of the original acoustic wave, i.e. the original wave has been attenuated. At this point, the analogy starts to break down because unlike billiard balls, phonons can be annihilated and created. However, just as in the case of the billiard balls, the total energy for phonon collisions is always conserved. This means that when one phonon with frequency $\omega_1(\mathbf{q_1},m_1)$ collides with another phonon of frequency $\omega_2(\mathbf{q_2},m_2)$, the resulting phonon must have frequency $\omega_3(\mathbf{q_3},m_3) = \omega_1 + \omega_2$, even though m_i does not necessarily have to be the same.

Another difference with the billiard ball analogy is that momentum – proportional to the wavevector $\mathbf{q}$ – does not necessarily have to be conserved. For the majority of cases, momentum conservation will also occur and these collision processes are called normal processes. However, due to the unique periodicity of the crystal lattice, there is

a quantity known as the crystal momentum **G** that can act as a "source" of momentum for the interaction such that certain collisions where momentum is not strictly conserved are also permissible. Such processes are called Umklapp processes.

In summary, we see that in collisions between two phonons resulting in a third (also referred to as three-phonon processes), energy conservation must be obeyed and momentum conservation must also be obeyed either strictly or by "borrowing" the crystal momentum. These rules can be summarized as

Energy conservation:

$$\omega_{acoustic} + \omega_{th,1} = \omega_{th,2} \text{ or } \omega_{acoustic} = \omega_{th,1} + \omega_{th,2} \tag{73}$$

Normal processes:

$$\mathbf{q}_{\mathbf{acoustic}} + \mathbf{q}_{\mathbf{th,1}} = \mathbf{q}_{\mathbf{th,2}} \text{ or } \mathbf{q}_{\mathbf{acoustic}} = \mathbf{q}_{\mathbf{th,1}} + \mathbf{q}_{\mathbf{th,2}} \tag{74}$$

Umklapp processes:

$$\mathbf{q}_{\mathbf{acoustic}} + \mathbf{q}_{\mathbf{th,1}} + \mathbf{G} = \mathbf{q}_{\mathbf{th,2}} \text{ or } \mathbf{q}_{\mathbf{acoustic}} = \mathbf{q}_{\mathbf{th,1}} + \mathbf{q}_{\mathbf{th,2}} + \mathbf{G} \tag{75}$$

Here, the subscript "*th*" indicates thermal phonons. The first equations on the left in each of (73)-(75) correspond to the cases where the acoustic phonon collides with a thermal phonon and produces a different thermal phonon of higher energy. The second equations correspond to the case where an acoustic phonon degenerates into two lower frequency thermal phonons. Since, we are in the regime $\omega_{acoustic} << k_B T/\hbar = \omega_{thermal}$, the latter is not as likely to occur and thus we will focus our attention on the former case.

Based on detailed analysis by prominent researchers in the area of internal friction, most notably Maris [63] and Herring [78], the conservation laws of (73)-(75) combined with consequences of $\omega_{acoustic} << k_B T/\hbar$ restrict the interaction between

certain acoustic and thermal phonon modes in a lattice. In general, three-phonon processes are restricted to collisions where the two thermal phonons are of the same mode, e.g. both longitudinal or both transverse. For longitudinal modes, which are of primary interest in UHF MEMS resonators, the allowable three-phonon processes are

$$L + L \rightarrow L$$

$$\left.\begin{aligned} L + T_F &\rightarrow T_F \\ L + T_S &\rightarrow T_S \\ L + T_F &\rightarrow T_S \\ L + T_S &\rightarrow T_F \end{aligned}\right\}$$

where 'L', 'T_F', and 'T_S' refer to longitudinal, fast transverse, and slow transverse modes. In all of these interactions, the leftmost mode is that corresponding to the acoustic mode. Specifically for the case of longitudinal acoustic waves traveling in the (100)-direction, zero-dispersion and isotropy may be assumed to greatly simplify the analysis, since we see from Figure 3.1 that the fast and slow transverse modes are degenerate in this direction and that the LA mode is very nearly linear up to 6 or 7 THz, where the majority of the thermal phonon population resides. Thus, the four processes bracketed above can be described simply as $L + T \rightarrow T$ without distinction between the fast and shear modes. Note that these assumptions may lead to oversimplification of the problem and are not valid for acoustic waves in other directions making exact predictions of *Q* based on these expressions difficult, but they do at least provide insight into the effect of different material parameters on the acoustic attenuation and a ballpark number of the theoretical limits in silicon and other materials.

With the possible phonon-phonon interactions identified, the question now is how to find the rate of interaction between these three phonon modes. This is a classical problem in quantum mechanics and is usually solved by application of Fermi's second

golden rule. This was applied to the case of three-phonon processes to give

$$\Gamma_{3ph} = \frac{2\pi}{\hbar}\sum_{f}\left|\left\langle \psi_f \left| \hat{H}_3 \right| \psi_i \right\rangle\right|^2 \delta\left(E_f - E_i\right) \tag{76}$$

In this expression, ψ_i corresponds to the initial state where the phonon occupation of the acoustic mode is given by $n_{acoustic}(\mathbf{q}_{\mathbf{acoustic}}, m_{acoustic})$ and ψ_f corresponds to the final states after scattering where $n_{acoustic}$ is either incremented or decremented by 1. Here, $\hat{H}_3$ is the perturbation Hamiltonian for three-phonon processes given by the cubic term in the Taylor expansion of the crystal Hamiltonian. This perturbation Hamiltonian represents the crystal free energy due to terms with a cubic dependence on atomic displacement.

Using this formulation, an expression for the total attenuation of (100)-longitudinal acoustic waves from both L + T → T and L + L → L processes can be given by [63]

$$\alpha_{LR,(100)} = \frac{\pi^2\hbar\omega}{15\rho}\left(\frac{k_B T}{\hbar}\right)^4\left[\frac{\gamma_{LL,L}^2}{2c_l^6}\tan^{-1}(2\omega\tau_{th}) + \frac{\gamma_{LT,T}^2}{c_l^2 c_t^4}\tan^{-1}\left(\frac{2\omega\tau_{th}c_t/c_l}{1+\omega^2\tau_{th}^2(1-c_t^2/c_l^2)}\right)\right]. \tag{77}$$

The resulting theoretical Q for (100)-longitudinal mode acoustic resonators in silicon in the Landau-Rumer regime is then given by

$$Q_{LR,(100)} = \frac{15\rho\hbar^3}{2\pi^2 k_B^4 T^4 c_l}\left[\frac{\gamma_{LL,L}^2}{2c_l^6}\tan^{-1}(2\omega\tau_{th}) + \frac{\gamma_{LT,T}^2}{c_l^2 c_t^4}\tan^{-1}\left(\frac{2\omega\tau_{th}c_t/c_l}{1+\omega^2\tau_{th}^2(1-c_t^2/c_l^2)}\right)\right]^{-1}. \tag{78}$$

Here, c_l and c_t are the longitudinal and transverse acoustic velocities and $\gamma_{LL,L}$ and $\gamma_{LT,T}$ are the effective Gruneisen parameters for the two phonon collision processes L + L → L and L + T → T. These parameters are defined as the fractional change in phonon frequency of a particular mode for a given strain. Also, τ_{th} is the average thermal phonon relaxation time, which is the mean time between collisions of thermal phonons. After collisions, the thermal phonons decay into other phonon modes, and therefore this parameter is also known as the thermal phonon lifetime.

This parameter τ_{th} appears in this expression due to some caveats regarding energy conservation at quantum time scales, which is very important in understanding the

region of validity of this theory. Imagine a specific phonon mode with ω, $\mathbf{q}$, and m. Since phonons in this mode can spontaneously decay due to collisions with other phonons within an average time τ_{th}, the fluctuations in energy for this mode averaged over a single period of acoustic oscillation is $\Delta E = \hbar\omega \mathrm{T}/\tau_{th} = h/\tau_{th}$. Surprisingly, rearranging this returns the famous Heisenberg uncertainty principle for energy and time: $\Delta E \tau_{th} = h$. This is far from coincidental; it means that the uncertainty in the energy of a single thermal phonon is in fact given by $\hbar/\tau_{th}$. However, recall that this derivation by Landau and Rumer is dependent upon energy conservation to determine the applicable selection rules for three-phonon processes. What this means is that the energy of the acoustic wave $\hbar\omega_{acoustic}$ must be significantly greater than any uncertainty in energy of these thermal phonon modes for these selection rules to be valid. In other words, it is required that

$$\hbar\omega_{acoustic} \gg \hbar/\tau_{th} \longrightarrow \omega_{acoustic}\tau_{th} \gg 1. \tag{79}$$

Only when this is true will the theory presented in this subsection be an accurate illustration of phonon-phonon based attenuation of acoustic waves. One should be careful lest they interpret this to mean that energy conservation does not occur when $\omega_{acoustic}\tau_{th} < 1$. All that is stated here is that in this case, a "collision" with a *single* thermal phonon is no longer physically meaningful. Since the original thermal phonon decays into other thermal phonon modes such that energy conservation does occur, the total energy integrated over all thermal phonons is still conserved. Otherwise, energy conservation on the macroscale would also be violated, which cannot be true. Thus, when considering acoustic attenuation for the case where $\omega_{acoustic}\tau_{th} < 1$, we must consider the interaction of the acoustic wave with the whole collection of thermal phonons. This theory has been worked out in the limiting case $\omega_{acoustic}\tau_{th} << 1$ and is known as the Akhiezer theory of acoustic damping in solids, which will be discussed

next.

3.3.3 Akhiezer Regime

As mentioned in the previous subsection, Akhiezer damping is concerned with the interaction of the phonons in the acoustic wave with the whole collection of thermal phonons. Recall that TED was a consequence of energy drawn from the resonator as a result of heat flow between strain-induced hot and cold regions of the resonator, which is a macroscopic thermal relaxation process. Similarly, we shall see that the Akhiezer effect can be thought of as the quantum mechanical analog of this phenomenon: the strain of the acoustic wave causes perturbations of the local thermal phonon distribution and the consequent microscopic relaxation of these excited phonon modes generates entropy and draws energy from the acoustic wave. But to understand this, we must first look at how the strain and the thermal phonon bath are coupled in a crystal lattice. Although a more detailed derivation using the phonon Boltzmann transport equation was presented by Akhiezer [79] and modified by Woodruff and Ehrenreich [62], a more intuitive – albeit less rigorous – explanation which still captures the essential details will be presented here.

In order to simplify the derivation of the phonon dispersion relations and other properties of the lattice, one key assumption is made: the Lennard-Jones interatomic potential – normally a very complicated function of interatomic distance – is approximated as a simple spring. This is done by taking a Taylor expansion of the internal energy to second order in the displacement; the effective interatomic spring constant k can then be approximated as twice the coefficient of this second-order term. However, due to the strong nonlinearity of this potential, even a 0.2 Angstrom displacement in the silicon lattice (roughly 4% of the lattice constant) results in about

a 10% deviation from the simple spring constant approximation. The displacement between atoms in a crystal lattice due to an elastic wave is roughly within the same range as this amplitude, which means that such strains can significantly influence the interatomic elastic energy storage and thus the phonon dispersion relation. In fact, this nonlinearity is the origin of the thermal expansion coefficient. We have already introduced a physical parameter illustrating this concept in the previous discussion of Landau-Rumer theory: the Gruneisen parameter, named after Eduard Gruneisen. He studied the relationship between volumetric changes and vibrational properties of a crystal lattice in detail [80] and showed that the phonon frequencies are related to a volumetric strain (otherwise known as dilatation) by

$$\begin{aligned}\omega'(\mathbf{q},m) &= \omega(\mathbf{q},m)(1-\gamma(\mathbf{q},m)(\varepsilon_{xx}+\varepsilon_{yy}+\varepsilon_{zz})) \\ &= \omega(\mathbf{q},m)(1-\gamma(\mathbf{q},m)\Delta).\end{aligned} \tag{80}$$

Here, $\omega'(\mathbf{q},m)$ and $\omega(\mathbf{q},m)$ are the phonon frequencies for wavevector $\mathbf{q}$ and mode m in the presence and absence, respectively, of dilatational Δ. We see from this expression that the Gruneisen parameter $\gamma(\mathbf{q},m)$ is specific to the phonon mode and wavevector. What is actually seen here is a quantum mechanical definition of the mode-dependent Gruneisen parameter. Frequently, what is referred to as just the Gruneisen parameter is actually the average of $\gamma(\mathbf{q},m)$ over all phonon modes weighted by the contribution of that mode to the specific heat. This is also the case for the Gruneisen parameters $\gamma_{LL,L}$ and $\gamma_{LT,T}$ in (77) and (78). Theoretically, this parameter is a combination of second and third-order elastic constants. The difficulty in accurately measuring the latter contributes to the wide range of reported experimental values for the Gruneisen parameter in silicon [81]-[83].

In any case, we see that a strain in the lattice with a non-zero dilatation (which is the case for any longitudinal strain) will shift the frequencies of the thermal phonons in the strained regions. In the case of RF MEMS resonators, the periodic, local strain

variations due to the acoustic standing wave will result in regions throughout the resonator where the phonon mode frequencies are shifted. The direction of the frequency shift will mirror the strain distribution in the resonator. If we look closely into one of these strained regions, we see that the n_1 phonons normally present at thermal equilibrium with frequency ω will now become phonons of frequency $\omega(1+\gamma)$. However, at thermal equilibrium, there should only be n_2 phonons with frequency $\omega(1+\gamma)$. Therefore, the system will attempt to relax to this quasi-equilibrium state through increased collisions with other thermal phonons. Such collisions increase the entropy of the system, leading to effective heat flow between different *phonon modes* (not regions of the solid, as in the case of TED). Another way that this has been described in the literature is that different phonon modes have different effective temperatures, which depend on the deviation from the equilibrium phonon population. The total heat flow is found by the weighted average over all phonon modes and the resulting energy equals the amount drawn away from the acoustic wave. Here, the subtlety that γ is mode-dependent is important: if all phonon mode frequencies shifted by the same relative amount, then all phonon modes would have the same increase or decrease in the number of thermal phonons, which is equivalent to simply increasing or decreasing the temperature of entire regions of the resonator depending on the magnitude and direction of strain. The total dissipation in this case would simply degenerate to that given purely by TED (i.e., heat flow between different *regions of the resonator*). To be exact, there will always still be macroscopic heat flow between different regions of the resonator – and thus TED-based losses – since certain regions will expand while others contract. But as mentioned previously, for the case of bulk mode resonators, the thermal eigenmodes typically do not strongly overlap with the strain distribution of the acoustic resonant modes, leading to low acoustic attenuation due to TED.

Finally, we arrive at the expression for attenuation due to the Akhiezer effect:

$$\alpha_{AKE} = \frac{C_v T}{2\rho c_l^3} \frac{\omega^2 \tau_{th}}{1+\omega^2 \tau_{th}^2} \left(\left\langle \gamma^2(\mathbf{q},m) \right\rangle - \left\langle \gamma(\mathbf{q},m) \right\rangle^2 \right) \tag{81}$$

where C_v is the volumetric heat capacity and τ_{th} is the thermal phonon relaxation time, which was mentioned in the previous section on Landau-Rumer theory. Interestingly, an effective variance of the Gruneisen parameter is used in (81). This is a result of the mode and wavevector dependence of the Gruneisen parameter. The resulting theoretical *Q* limit due to Akhiezer damping is then

$$Q_{AKE} = \frac{\rho c_l^2}{C_v T} \frac{1+\omega^2 \tau_{th}^2}{\omega^2 \tau_{th}} \left(\left\langle \gamma^2(\mathbf{q},m) \right\rangle - \left\langle \gamma(\mathbf{q},m) \right\rangle^2 \right)^{-1}. \tag{82}$$

This expression is significantly different from the *Q* limit predicted by Landau-Rumer theory given in (78). While both (78) and (82) have very complex dependencies on a number of different parameters including Gruneisen parameter, acoustic wave velocity, specific heat, and thermal phonon relaxation time, it is difficult to directly investigate the dependence of *Q* on these parameters since they cannot be controlled experimentally. Temperature, on the other hand, can be readily controlled in a well-designed experimental setup. In addition, since both (78) and (82) show distinctly different dependencies on temperature, such measurements would allow us to draw meaningful conclusions regarding acoustic attenuation without *a priori* knowledge of the dominant loss mechanisms. These methods will be applied to the high-*Q* resonators demonstrated in Chapter 2 and the resulting data will be used to arrive at conclusions regarding the theoretically attainable *Q* in gigahertz frequency silicon MEMS resonators.

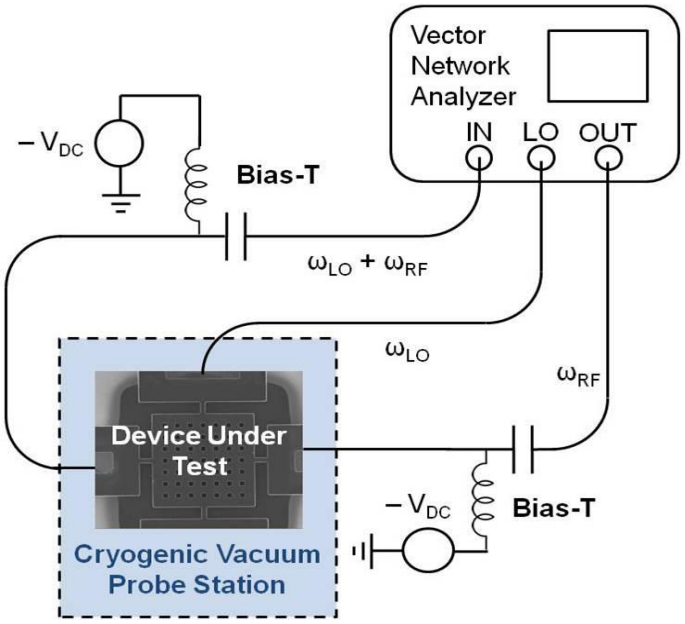

Figure 3.2. Scalar mixing measurement setup to avoid the effects of parasitic feedthrough paths and obtain the purely mechanical response of the resonator. Device under test is placed in a controlled cryogenic vacuum chamber cooled with liquid helium is used for temperature measurements. Calibration using an impedance standard substrate is performed at every temperature step throughout the measurement.

3.4 Temperature Study of Quality Factor in 3.72 GHz Degenerately-Doped, Single-Crystal Silicon Longitudinal Mode Resonator

To investigate how phonon-phonon interactions in single-crystal silicon limit the intrinsic *Q* of MEMS resonators, we performed a temperature sweep over a wide range from 1.5 to 373 K. In interpreting this data, we look specifically for the characteristic temperature dependencies exhibited by either Landau-Rumer (~$1/T^4$) or Akhiezer theories (~$1/T$). For these measurements, we use a scalar mixing technique illustrated in Figure 3.2. This technique uses the inherent nonlinearity of capacitive actuation to apply the input stimulus at a frequency greater than that of the resonant frequency and obtain the output at the resonant frequency by using an external carrier. Such methods enable the application of a purely mechanical force without the effects of capacitive feedthrough. This allows for accurate measurement of mechanical *Q*

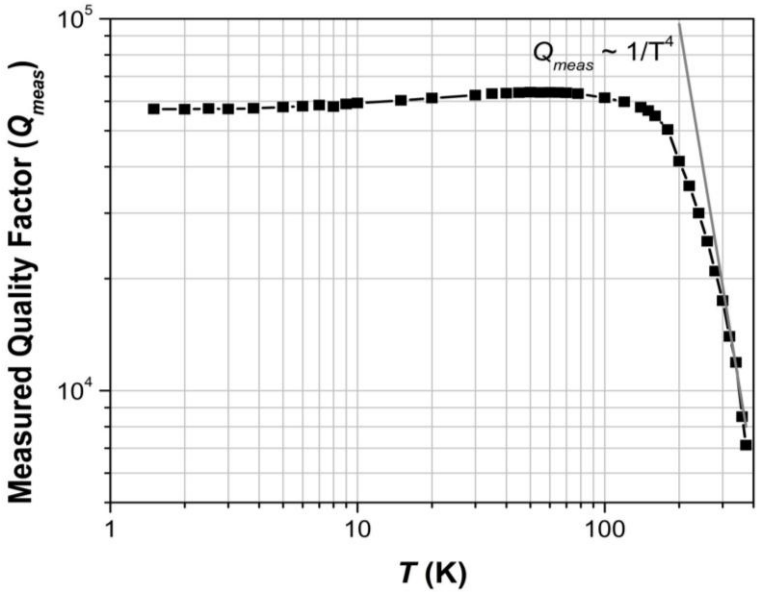

Figure 3.3. Measured quality factor of pn-diode internally transduced resonators as a function of temperature. The Q peaks to a value of roughly 63,000 at around 50 K and slowly decreases to roughly 57,000 at 1.5 K.

even in cases where $k_t^2 \cdot Q < 1$. A Lakeshore cryogenic vacuum probe station with liquid helium supply is used to cool the chamber to the low temperatures required for this study. The measured Q as a function of temperature is plotted in Figure 3.3 and it shows that at temperatures near 300 K, the Q follows a roughly $1/T^4$ trend in agreement with Landau-Rumer theory. At lower temperatures, the Q steadily tapers off and peaks to a value of roughly 63,000 at T ~ 50 K. Interestingly, below this point, the Q slowly drops off to roughly 57,000 at 1.5 K. At first glance, there may be a number of explanations, the seemingly obvious hypotheses including the temperature coefficient of the parasitic electrical resistance loading the resonator or support losses induced by the tethers as they undergo thermal contraction. In order for the first hypothesis to be correct, the resistivity of the degenerately-doped silicon (donor concentration $>1\times10^{19}$ cm^{-3}) interconnect must be inversely proportional to temperature, at least in the range of 1.5-50 K. Previous studies in the literature, however, indicate that the resistivity in such degenerately-doped silicon monotonically

increases with temperature [84], making this hypothesis invalid.

The second hypothesis is concerned with how temperature changes in the support tethers may either shift the tether length away from the optimal quarter-wavelength [85]. Considering the coefficient of thermal expansion of silicon is 2.6 ppm/K at room temperature and assuming that this value is constant with temperature (it actually decreases with temperature, but assuming a constant value will provide a conservative estimate of the shift from quarter-wavelength which will still prove the point), the total length shift for a 5 μm support tether (5^{th} harmonic of the quarter-wavelength support) will be roughly 4 nm. This corresponds to 0.4% shift with respect to the wavelength. Based on the transmission line model of mechanical coupling springs by Konno [86], it can be assumed that the support loss will increase more or less sinusoidally with increasing deviation from a perfect quarter-wavelength support. Since the effect of thermal expansion is very small in this case, we can approximate this sinusoidal dependence as linear and conclude that the *Q* will also change very slightly over the entire temperature range. In addition, these devices also exhibit a negative temperature coefficient of frequency (TCF) of roughly -10 ppm/K as seen in Figure 2.19, meaning that the resonant wavelength should also decrease as temperature decreases, thus slightly mitigating the mismatch from quarter-wavelength. Therefore, for simplicity, we will assume that the *Q* due to anchor loss is relatively insensitive to temperature. This assumption is checked by simulation and will be presented in the following sections for a more complete temperature dependent model of *Q*.

With this assumption, we can follow a method of analysis similar to that of El Habti *et al*. who investigated the phonon-phonon losses in quartz crystal resonators [87]. They assume that all other losses in their system are temperature independent

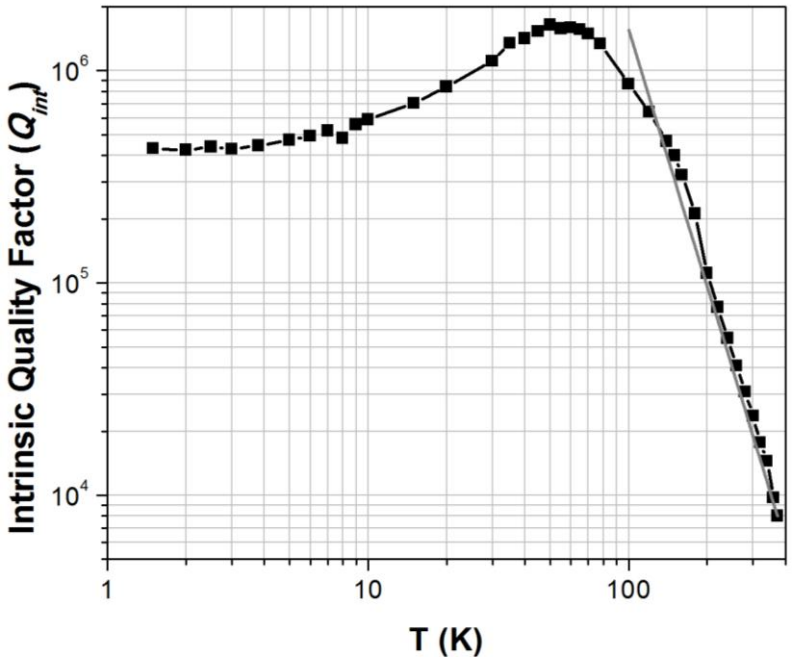

Figure 3.4. Intrinsic quality factor extracted using Matthiessen's rule in a manner similar to that of [87]. The $1/T^4$ dependence on Q for temperatures greater than 100 K indicates that Landau-Rumer based phonon-phonon dissipation is dominant in these temperatures.

and use Matthiessen's rule shown in (71) for the total Q of a system to find the intrinsic $Q_{intrinsic}$

$$\frac{1}{Q_{intrinsic}(T)} = \frac{1}{Q_{total}(T)} - \frac{1}{Q_{anchor}}. \tag{83}$$

The results of this extraction are shown in Figure 3.4 indicating a $1/T^4$ dependence for temperatures greater than 100 K. At lower temperatures, other mechanisms cause the Q to gradually decrease with temperature. As discussed in the previous paragraph, immediately obvious reasons such as the temperature coefficient of series resistances and support losses have been eliminated as they are unable to account for the significant (~10%) changes in Q. This opens up the search for other candidates that may be significant in degenerately-doped silicon at such low temperatures to explain this decrease in Q.

Before moving on, one comment regarding the thermal phonon relaxation time τ_{th} will be made here. Traditionally, the MEMS community had been in agreement in

regarding the intrinsic *f*-*Q* product to be a constant value for a given material. This is indeed the case when acoustic attenuation is governed by Akhiezer phonon-phonon scattering, as is typically the case for lower frequency (10-100 MHz) bulk-mode resonators near room temperature. It was also previously thought that this was valid for frequencies as high as 100 GHz, effectively meaning that practical RF MEMS resonators would all be limited by this constant *f*-*Q* restriction. However, there has been both experimental and theoretical work presented in the literature suggesting that the thermal phonon relaxation is on the order of 100 ps, yielding a crossover frequency (where $f = 1/2\pi\tau_{th}$) on the order of 100 MHz [75], [88], [89]. In fact, Ilisavskii and Sternin found in [75] the silicon thermal phonon relaxation time at room temperature to be roughly 225 ps corresponding to a crossover frequency of roughly 700 MHz. This supports our conclusion that the *Q*-limiting phonon-phonon scattering mechanism in the 3.72 GHz pn-diode internally transduced resonators can be described by the Landau-Rumer theory discussed in 3.3.2.

More recent results use a similar method to find the crossover temperature where the measured *Q* exhibits a kink. This is seen in Figure 3.5, which shows experimental data from a 61 MHz wine-glass disk resonator [90]. The solid line represents the theoretical limit due to phonon-phonon scattering in both the Landau-Rumer and Akhiezer regimes, as given by (78) and (82). In this work, they find that the *Q* is strongly dependent on the position and number of tethers, indicating that the device is still anchor loss limited. In spite of this, however, there is a distinct minimum at around 150 K, which corresponds very closely to the value predicted by theory when the thermal phonon relaxation times provided in [75] are used. These experimental results all seem to corroborate the presented measured results and indicate that

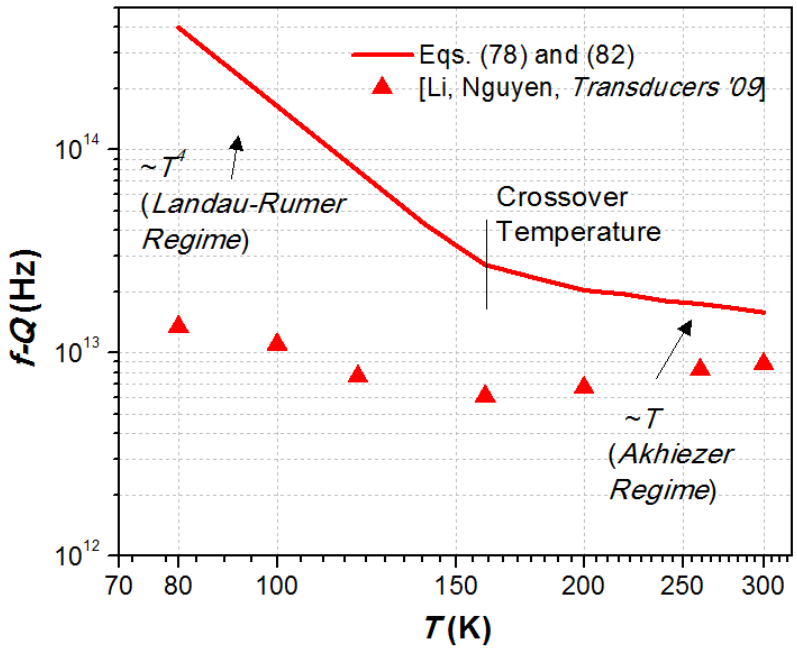

Figure 3.5. *f-Q* product as a function of temperature for 61 MHz wine-glass disks from [90]. Data shows a distinct kink in the *f-Q* product at temperatures around 150 K, which is near where (78) and (82) predict the crossover temperature between Akhiezer and Landau-Rumer phonon-phonon scattering to lie. Data reproduced from [90].

gigahertz frequency silicon MEMS resonators are limited by Landau-Rumer phonon-phonon scattering near room temperature.

3.5 Electron-Phonon Interactions in Degenerately Doped Silicon

Based on the experimental data presented in the previous section, the dominant *Q* limiting mechanism at low temperatures must have an acoustic attenuation that is actually inversely proportional to temperature. This is rules out phonon-phonon scattering as the dominant acoustic loss mechanism at such low temperatures. This makes sense, as the number of thermal phonons – and thus, quasi-particles with which the acoustic wave could interact – decreases with temperature. Any other quasi-particles (i.e., electrons and holes) also decrease exponentially with temperature for intrinsic silicon. However, in degenerately-doped silicon where the dopant

concentration is so high that free carriers are present in large quantities even at very low temperatures, the attenuation due to these carriers may not be negligible. It may then be worth investigating the impact of electron-phonon dissipation in order to understand the observed experimental behavior presented in Section 3.4.

3.5.1 Low Temperature Thermal Conductivity

A large amount of theory developed for the interaction between thermal phonons and electrons has been in the context of thermal conductivity and as such, we shall start our discussion here. Thermal conductivity is also relevant to our investigation of acoustic attenuation since both phenomena are different manifestations of the same phenomenon, as will be discussed briefly. In solids, there are two main carriers of thermal energy: electrons and phonons. Thermal transport via electrons arises from fact that the Fermi function describing the occupied energy states of electrons is temperature dependent. Thus, the total energy of the free carriers in a solid will change with temperature and this incremental change is known as the electron specific heat. This same fact is true of phonons, but the population is now given by the Bose-Einstein distribution, yielding a separate quantity known as the phonon specific heat. In fact, the phonon contribution to the overall thermal properties of solids is orders of magnitude larger than the electron contribution in semiconductors and insulators, which are the primary materials of interest for micromechanical resonators; as such, only phonon thermal conductivity will be discussed here. When a temperature difference is applied across a material, the thermal phonons at the end with the higher temperature will start to increase in energy and a net flow of these quasi-particles will travel down the length of the solid. They will scatter with other thermal phonons, defects in the lattice, or boundaries and impart some of this thermal energy to the

lattice, raising the temperature of the surrounding regions as well. This heat conduction process continues down the length of the solid until the temperature distribution reaches an equilibrium state. This process can also be described classically through the following equation for the heat flux Q_H

$$Q_H = -\kappa \nabla T. \tag{84}$$

where κ is the thermal conductivity and T is the temperature. This is analogous to Ohm's law, which gives the relationship between the current density flowing through a material and the applied potential. Not surprisingly, the physical origin of both thermal conductivity κ and electrical conductivity σ is the scattering of the energy carrying elements.

A classical treatment of scattering can be applied if we treat the thermal phonons as a gas of particles. Under this assumption, we can apply findings from the kinetic theory of gases to express the thermal conductivity as

$$\kappa = \tfrac{1}{3} C_v \langle v \rangle \Lambda = \tfrac{1}{3} C_v \langle v \rangle^2 \tau \tag{85}$$

where C_v is the volumetric heat capacity, $<v>$ is the average phonon velocity, and Λ is the phonon mean free path. The second equality in (85) is obtained by defining the mean free path as

$$\Lambda = \langle v \rangle \tau \tag{86}$$

where a scattering time τ is used to characterize the scattering behavior. This scattering time is actually the aggregate effect of all phonon scattering mechanisms and their associated scattering times τ_i and can be expressed as

$$1/\tau = \sum\nolimits_i 1/\tau_i \tag{87}$$

where 'i' indicates a particular source of phonon scattering, e.g. other phonons, electrons, crystal impurities, etc. Effectively, this total scattering time τ is equivalent to the thermal phonon lifetime τ_{th} that was introduced in the previous sections. At this point, the main difference between thermal conductivity and acoustic attenuation

becomes clear. As previously discussed, acoustic attenuation is determined by how the coherent phonons in an acoustic wave – a very specific phonon mode – scatter with other quasi-particles in the solid; thermal conductivity, on the other hand, is determined by how the ensemble of thermal phonons clustered around $\omega_{thermal} \approx k_B T/\hbar$ scatter with quasi-particles (including themselves) to limit heat flow in a solid. Regardless of this difference, though, both phenomena have the same origins. Thus, any mechanisms that may limit thermal conductivity may also be relevant for explaining acoustic attenuation.

Looking at the experimental data of thermal conductivity in doped silicon available in the literature (Figure 3.6, [91]), three distinct temperature regions become apparent. In the high temperature region (T > 100 K), the approximately $1/T$ dependence and the apparent independence on doping of the thermal conductivity indicates that phonon-phonon scattering limits the thermal phonon lifetime. Around T = 60 K, we observe peaks in thermal conductivity with the peak temperature dependent on the doping concentration, in this case indicating that scattering due to dopant impurities is dominant. Dopant impurities cannot, however, fully explain the reduction in thermal conductivity at temperatures lower than 60 K, since thermal conductivity limited by impurity scattering should exhibit a $1/T^{\alpha}$ dependence, where $\alpha \sim 1$ to 3/2 [92]. In other words, if impurity scattering were the dominant mechanism at low temperatures, the thermal conductivity should increase with decreasing temperature, which is not what is observed in the experimental data. Other work attributes the reduced thermal conductivity at temperatures below the peak to boundary scattering and scattering to due charge carriers [93]-[95]. Figure 3.6 indicates that for lightly doped silicon films, the thermal conductivity is nearly identical to that of the nearly pure silicon sample and follows T^3, which is expected since the phonon lifetime limited by boundary

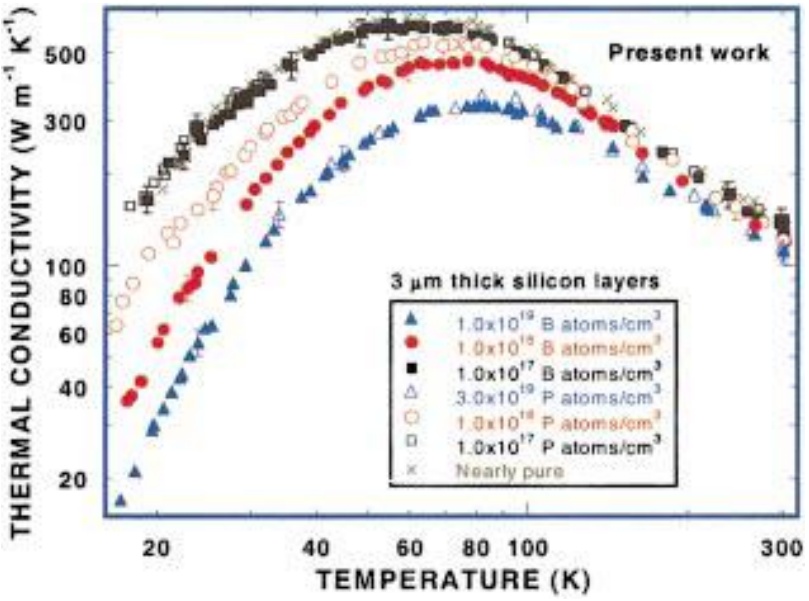

Figure 3.6. Experimental thermal conductivity data from [91] for 3 μm thick single-crystal silicon layers on SOI with different doping levels and polarity.

scattering should be determined only by geometric properties (i.e., layer thickness) for low temperatures [93]. The remaining difference between doped samples has been modeled by the scattering of thermal phonons due to both free and bound charge carriers with good agreement with experimental results at low temperatures [94], [95]. Other clues that might suggest interactions between electrons and phonons in these devices at low temperature include the measured resonant frequency shifts with temperature shown in Figure 3.7(a). Interestingly, it is observed that the resonant frequency reaches a maximum value at T ~ 50 K and then slowly decreases with temperature. This type of behavior was also observed in highly doped silicon samples by Mason and Bateman [96], reprinted here in Figure 3.7(b) to illustrate the similarities. Mason and Bateman specifically measured acoustic velocity shifts through time-of-flight experiments in bulk silicon samples with ultrasonic transducers. Thus, their measurements were not affected by tethers or other supporting structures,

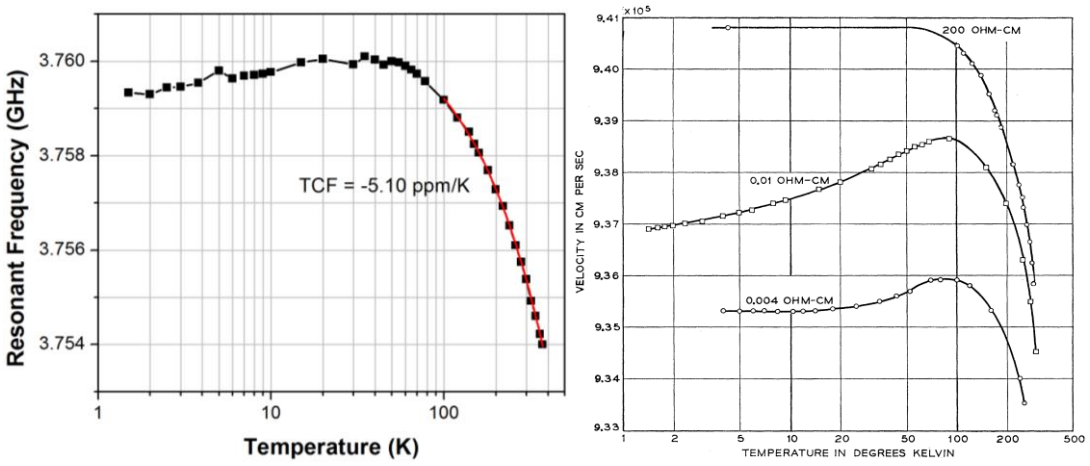

Figure 3.7. (a) Measured resonant frequency as a function of temperature for the pn-diode transduced resonator and (b) acoustic velocities of doped silicon obtained via time-of-flight measurements as a function of temperature for different values of resistivity (from [96]). The data for pn-diode transduced resonator exhibits properties that qualitatively are very similar to the velocity change with temperature from [96].

like those present in the resonators in this dissertation. The similarities between both the temperature dependence of acoustic velocity and resonant frequency shifts seen in Figure 3.7 provide additional evidence that the effect of tethers on the acoustic behavior of the resonators is very small and suggest that electron-phonon interactions are significant.

It becomes evident from this discussion that electron-phonon scattering may contribute significantly to the low temperature acoustic attenuation of micromechanical resonators using degenerately doped single-crystal silicon. However, due to an incomplete understanding of the interactions between charge carriers and phonons in the MEMS community, many researchers have dismissed this mechanism as a significant source of acoustic attenuation. While this may be true for resonators limited by anchor losses and other extrinsic mechanisms at low temperature [90], this incorrect assumption arises from only considering the theory of electron-phonon dissipation in metals [97]. This is obviously not applicable for commonly used semiconductor resonator materials such as silicon, where the electron states are

described by a more complex theory. A brief qualitative review of the established theory surrounding electron states in semiconducting crystals and their interactions with phonons will be presented next.

3.5.2 Electrons and Acoustic Phonons in Degenerately Doped Silicon

It may seem unlikely for free carriers to exist at all in silicon at low temperatures due to thermal freeze-out. This is indeed true for intrinsic or doped silicon below a critical degenerate doping concentration. However, for degenerately doped semiconductors, electrical conduction does indeed occur even at low temperatures where freeze-out would be expected [84], indicating very clearly that free carriers do indeed exist under such conditions. In fact, if carrier freeze-out did occur in the pn-diode transduced resonators of Chapter 2, there should not be any response at these low temperatures. The fact that transmission measurements exist and quality factors can be extracted provides further evidence for this argument. But to understand why free carriers can still exist at such low temperatures, one must again look at the band structure of the crystal and how it changes with dopant impurities. We will restrict our attention to group III (acceptor, e.g. boron) or V (donor, e.g. phosphorus) impurities since they hold the most relevance for this work and silicon-based devices in general.

Without loss of generality, we will discuss what happens when a phosphorus atom is placed in a substitutional lattice site in an otherwise perfect silicon crystal. The theory is almost exactly the same for acceptor impurities in silicon, such as boron. In this scenario, only 4 of the 5 electrons available from the phosphorus atom are needed to form covalent bonds with the surrounding silicon atoms. Thus, there is an extra electron and a phosphorus ion P^+, which provides a perturbation to the periodic potential of the lattice. By applying the effective mass theorem to find the

wavefunction of the extra electron, it is found that the behavior is very similar to that of an electron in a hydrogen atom. In particular, the energy states are quantized with respect to the conduction band and are spaced in a similar fashion but with a different equivalent Rydberg constant. The only difference is that the vacuum permittivity ε_0 and electron rest mass m_0 in the Rydberg constant are now replaced by the relative permittivity of silicon $\varepsilon_{si}\varepsilon_0$ and the effective electron mass in silicon m_e^*, respectively. In addition, for the equivalent 1*s* quantum state, there is an effective Bohr radius a_B, which is also identical to its simple hydrogen counterpart except that the relative permittivity and electron mass are again different. The effective Bohr radius for silicon is 17.2 Angstroms, which is significantly larger than the silicon lattice constant of 5.43 Angstroms and the effective donor ground state for a phosphorus donor is 45 meV. This means that at T = 0 K, the extra electron provided by a single phosphorus atom is confined to a radius of 17.2 Angstroms from the center of the impurity ion and the ionization energy of this electron is 45 meV. Essentially, the electron will "orbit" a region encompassing a number of silicon atoms rather than being confined to a single atom.

What is important here are not the actual numbers but the fact that the extra electrons left over from the phosphorus impurities have spatially confined wavefunctions corresponding to discrete donor levels in the band diagram (e.g., ground state level 45 meV below the conduction band for the case of phosphorus). The same is true for acceptors: for example, boron has a ground state acceptor level which is 45 meV above the valence band. This is true when the impurity concentration is low enough such that the impurities are too far from each other (>> effective Bohr radius) for the carrier wavefunctions to overlap. However, as the doping density increases, these wavefunctions will start to overlap, eventually giving rise to a continuous *band*

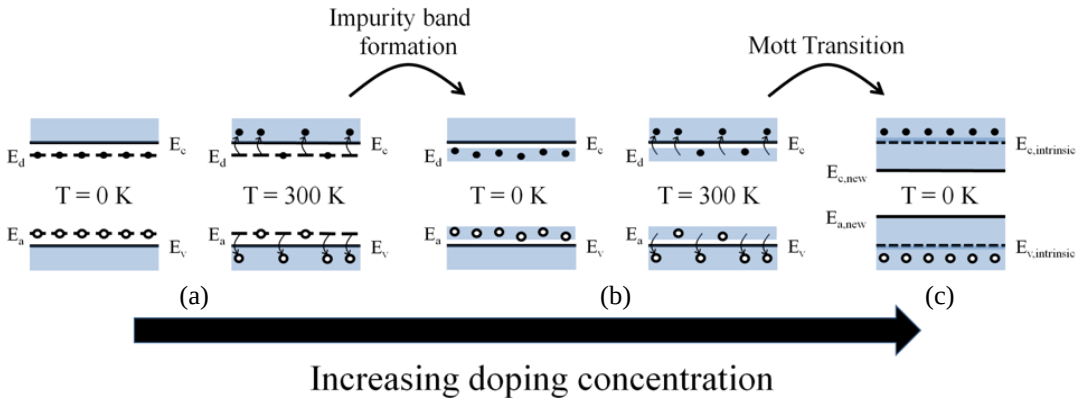

Figure 3.8. Illustration of electronic band structure of a semiconducting material and how it changes as the doping concentration increases. (a) Typical band structure and donor/acceptor states with light to moderate doping at zero-Kelvin and room temperature. (b) Formation of impurity band centered around original donor/acceptor states. (c) After Mott transistion, where impurity band merges with the conductance/valence bands to result in free carriers even at absolute zero.

of energies centered around the original discretized level. The width of the band will continue to increase until it merges with the original conduction band at a critical concentration [98]. Also, in this regime, the Fermi level is observed to be inside the conduction or valence bands and a transition occurs to a metallic state where the semiconductors become "semi-metals." Most notably, in this state, free carriers exist even for T = 0 K since all states below the Fermi level are filled. These changes in electronic band structure due to doping concentration are illustrated in Figure 3.8. For such semi-metals, Mikoshiba presents an inhomogeneity model for the relative concentration of free carriers to carriers still bound to their impurity ions as a function of the doping concentration [99]. Others have included Mikoshiba's model to refine predictions of electron-phonon and impurity scattering on the low temperature thermal conductivity of silicon [91], [94], [95]. This inhomogeneity model is based on approximating the distribution of dopant ions using a Poisson distribution, which then yields a probability that the electron wavefunctions will overlap. According to this model, for doping concentrations greater than 3×10^{18} cm^{-3}, the free carrier concentration is nearly equal to the doping concentration, assuming that all dopants

can find their way into substitutional lattice sites of the underlying crystal. This value is also confirmed experimentally by a kink in the number of Hall carriers and sharp drop in resistivity above this doping concentration [84], [99]. Thus, for the devices in Chapter 2 which make use of degenerate doping levels greater than 1×10^{19} cm^{-3}, we can assume that the free electron concentration is roughly equal to the doping concentration, even at temperatures as low as 1.5 K.

Ziman has developed a theory concerning the scattering of phonons by free charge carriers [64]. For reasons previously explained, the relevant interactions between phonons and charge carriers in the resonators presented in this dissertation are limited to scattering due to free carriers. The scattering rate of a phonon with wavevector **q** and mode *m* due to free electrons as calculated by Ziman is

$$\Gamma_{el-ph,\,free} = \frac{(m_e^* E_D)^2 k_B T}{2\pi\hbar^4 \rho c_{acoustic}} \ln\left[\frac{1+\exp\left\{\eta^* - N/T - PTx_\omega^2 + x_\omega/2\right\}}{1+\exp\left\{\eta^* - N/T - PTx_\omega^2 - x_\omega/2\right\}}\right] \tag{88}$$

where

$$N = \frac{m_e^* c_D^2}{2k_B},\quad P = \frac{k_B}{8m_e^* c_D^2},\quad \eta^* = \frac{\pi^2\hbar^2(3N_m/\pi)^{2/3}}{2m_e^* k_B T},\quad x_\omega = \frac{\hbar\omega}{k_B T}. \tag{89}$$

Here, c_D is the Debye average phonon velocity, N_m is the free electron concentration, and m_e^* is the density of states effective mass. Ziman's work, however, is valid only for interactions between electrons and phonons of wavevector $\mathbf{q} < 2\mathbf{K_F}$, where $\mathbf{K_F}$ is the Fermi wavevector. For a doping concentration of 1×10^{19} cm^{-3}, the Fermi wavevector $\mathbf{K_F} = 6.67\times10^8$ m^{-1}, which corresponds to a longitudinal acoustic wave in the <100> plane of approximately 90 GHz. This limit is due to energy and momentum conservation constraints. Kosarev added the contribution of the large electric field in the vicinity of the dopant ions and showed that interactions can also occur for $\mathbf{q} \geq 2\mathbf{K_F}$ [65]. This added contribution explains some of the discrepancies between Ziman's model and the thermal conductivity due to degenerately doped silicon. Kosarev's theory, however, will not be explicitly discussed here because it is not applicable to

the devices presented in this dissertation. In the multi-GHz frequency range, (88) should suffice in predicting the quality factor due to phonon scattering by free carriers. From (88), the Q due to electron-phonon scattering in the resonators presented in this dissertation can be found to be

$$Q_{el-ph,\,free} = \frac{2\pi\hbar^4 \rho c_{acoustic}\omega}{(m_e^* E_D)^2 k_B T} \ln\left[\frac{1+\exp\left\{\eta^* - N/T - PTx_\omega^2 + x_\omega/2\right\}}{1+\exp\left\{\eta^* - N/T - PTx_\omega^2 - x_\omega/2\right\}}\right]^{-1} \tag{90}$$

This expression is incorporated into the model for Q for the pn-diode transduced resonators with degenerate doping, which will be presented in the next section.

3.6 Model of Temperature Dependent Acoustic Loss in GHz Frequency Single-Crystal Silicon Resonators

Knowledge of the various phonon scattering mechanisms discussed in the previous sections now allows the development of a temperature dependent model for Q. We will first start by modeling the extrinsic mechanism most relevant for these devices: support losses. Support loss simulations were performed using COMSOL, a 3-D finite element modeling software. Typically, mechanical losses are modeled by introducing a lumped loss parameter in the material properties. This method, however, is overly simplistic and is not relevant in terms of finding anchor-related acoustic losses which are only geometry-dependent. One method of simulating support losses that is becoming increasingly widespread is introducing perfectly matched layer (PML) boundary conditions in frequency response simulations to find the acoustic energy flux through the support structures. These PMLs employ a mathematical transformation of the spatial variable in the specified region such that any acoustic wave traveling in this region will exponentially decay. This prevents such waves from reflecting back and affecting the resonant mode shape while simultaneously allowing the acoustic energy

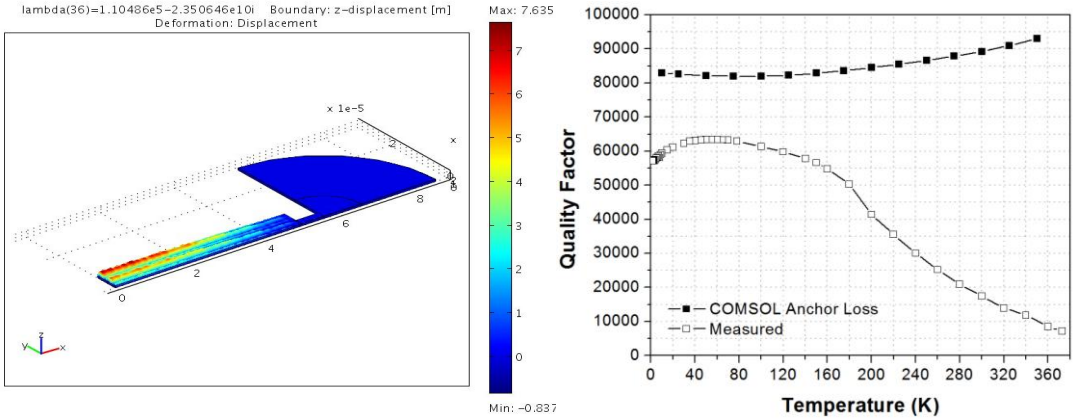

(a) (b)

Figure 3.9. (a) Geometry used for COMSOL simulations to extract support losses using matched layer boundary conditions. (b) Simulation results from COMSOL showing Q limited by support loss (black squares) and measured Q (white squares).

leaving the resonator to be calculated. These simulations, however, are extremely time-consuming. Others have used the underlying principle behind these PMLs to estimate anchor losses using faster modal simulations [100]. Such methods define imaginary elastic constants and densities for the surrounding material in such a way that the acoustic impedance still remains the same. This results in a complex eigenfrequency from which the Q can be defined. Steeneken uses this method to obtain the Q of stem-supported disks with reasonable accuracy [100]. This method was also employed here to approximate the anchor losses in the resonator structure.

Figure 3.9(a) shows the structure used in the COMSOL simulations for extracting support losses. We make use of the symmetric boundary conditions in COMSOL and thus simulate only one quarter of the resonator structure to reduce computation time. The extracted support loss Q_{anchor} is shown in Figure 3.9(b) as a function of temperature. This simulation assumes a completely linear silicon thermal expansion coefficient of 2.6 ppm/K, resulting in an overall conservative estimate. We also incorporate the temperature coefficients of the silicon elastic constants c_{ij} as given by [101]. These simulations show Q_{anchor} varying between 82,000 and 93,000 for

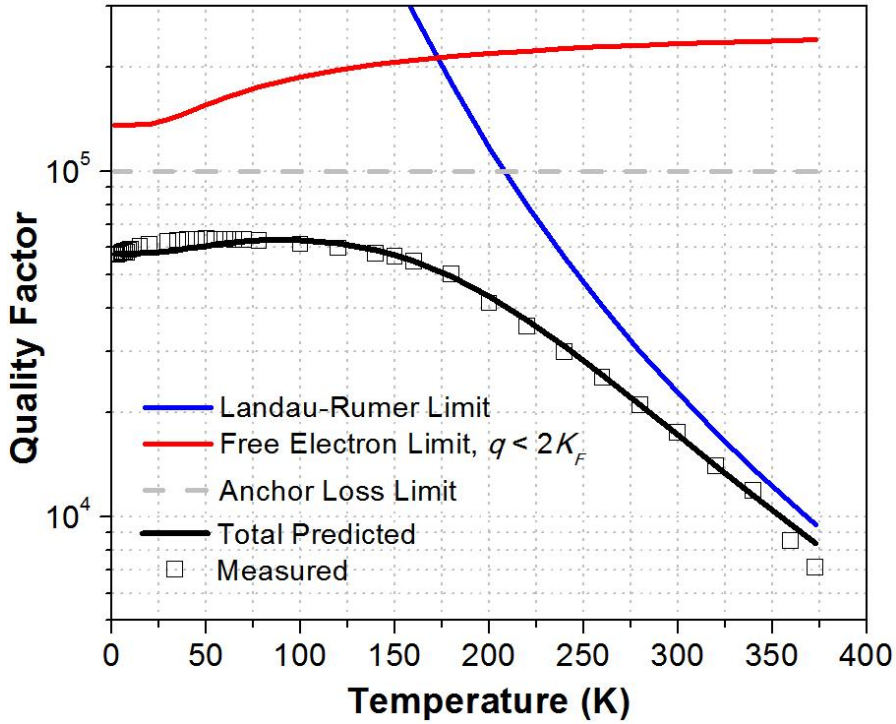

Figure 3.10. Theoretically predicted *Q* (black) based on all the different acoustic energy dissipation mechanisms discussed in this chapter: support loss, phonon-phonon scattering, impurity scattering, and free electron scattering. Individual contributions of each mechanism are also plotted. Impurity scattering curves are not shown here since their contribution is negligible to overall *Q* but is included in the model.

temperatures between 1.5-300 K. More importantly, however, we see that the concavity of the COMSOL-based values for Q_{anchor} and that of the measured *Q* do not align at low temperatures. Also, the rate of change of Q_{anchor} from COMSOL is significantly lower than the measured data for temperatures below 20 K. It is concluded based on this evidence that the low temperature *Q* reduction is not due to acoustic energy loss through the support tethers.

Having modeled the support losses in the structure and investigated the theory behind the various sources of acoustic attenuation in silicon, a full model predicting the *Q* over a range of temperatures may be presented. The different components of the model and the corresponding expressions for the *Q* limited by each are given in Table 3.1. These expressions are plotted together with the experimental data in Figure 3.10

Table 3.1. Various acoustic loss mechanisms included in the model shown in Figure 3.1 and their analytical expressions

Impurity Scattering [61]	
$Q_{imp} = \frac{\pi n^2 {c_D}^3}{3N_D}\left[\left(\frac{M}{\Delta M}\right)^2 + 2\left(\frac{G}{\Delta G}\right)^2\right]^{-1} \frac{1-e^{-\hbar\omega/k_B T}}{\omega^3}$	(91)
Phonon-Phonon Scattering [62], [63]	
Akhiezer Effect	$Q_{AKE} = \frac{\rho c_l^2}{C_v T}\frac{1+\omega^2\tau_{th}^2}{\omega^2\tau_{th}}\left(\left\langle\gamma^2(\mathbf{q},m)\right\rangle - \left\langle\gamma(\mathbf{q},m)\right\rangle^2\right)^{-1}.$ (82)
Landau-Rumer Effect	$Q_{LR,(100)} = \frac{15\rho\hbar^3}{2\pi^2 k_B^4 T^4 c_l}\left[\frac{\gamma_{LL,L}^2}{2c_l^6}\tan^{-1}(2\omega\tau_{th}) + \frac{\gamma_{LT,T}^2}{c_l^2 c_t^4}\tan^{-1}\left(\frac{2\omega\tau_{th}c_t/c_l}{1+\omega^2\tau_{th}^2(1-c_t^2/c_l^2)}\right)\right]^{-1}$ (78)
Free Electron-Phonon Scattering [64]	
$\boldsymbol{q < 2K_F}$	$Q_{ep,q<2K_F} = \frac{2\pi\rho {c_l}^2\hbar^4\omega}{m_e^{*2}E_D^2 k_B T}\left(\ln\left(\frac{1+e^{\eta^*-N/T-PTx^2+x/2}}{1+e^{\eta^*-N/T-PTx^2-x/2}}\right)\right)^{-1}$ (90) $N = \frac{m_e^* c_D^2}{k_B}$, $P = \frac{k_B}{8m_e^* c_D^2}$, $\eta^* = \frac{\pi^2\hbar^2(3N_m/\pi)^{2/3}}{2m_e^* k_B T}$

ρ = density	τ_{th} = thermal phonon lifetime
n = atomic density	C_v = volumetric heat capacity
N_D = dopant density	E_D = dilatational deformation potential
M = host atomic mass	γ = Gruneisen parameter
ΔM = mass difference	κ = thermal conductivity
G = host crystal interatomic force constant	m_e^* = effective electron mass
ΔG = interatomic force constant difference	N_m = metallic electron density $\approx N_D$ (in this work)
c_l = longitudinal velocity	q = acoustic wave vector magnitude
c_t = shear velocity	a = effective Bohr radius
c_D = Debye velocity	

and show relatively good agreement with measured results. This plot clearly shows different temperature regions in which particular attenuation mechanisms are dominant. For instance, we see that near room temperature, phonon-phonon scattering as described by Landau-Rumer theory is dominant, while at lower temperatures, anchor losses and electron-phonon scattering together to limit the resonator *Q*. While the *Q* limited by free carrier scattering is still a factor of 2 greater than the predicted anchor loss at low temperatures, it is definitely not negligible, as was assumed to be the case throughout most of the MEMS community.

In fitting the data with the different attenuation mechanisms, a few physical parameters were varied. These include the mode specific Gruneisen parameters ($\gamma_{LL,L}$ and $\gamma_{LT,T}$) and the dilatational deformation potential E_D. These parameters were chosen largely because of the lack of consistent experimentally extracted values in the literature. To be fair, extraction of such parameters is not simple and is highly sensitive to a wide array of factors, including the properties of the acoustic wave itself. To minimize the number of fitting parameters and reduce the burden on the fitting algorithm, we assume $\gamma_{LL,L}$ and $\gamma_{LT,T}$ are roughly equal to an equivalent Gruneisen parameter γ. The values we obtain are $\gamma^2 = 0.2116$ and $E_D = 0.19$ eV and 0.05 eV for phosphorus-doped Si and boron-doped Si, respectively. Since the resonator can be divided into two distinct n-type or p-type regions, the total scattering rate due to charge carriers is the average of the two rates due to scattering by electrons and holes, separately. The values used for these fitting parameters all fall within the spread of reported values in the literature [81]-[83], indicating that the scenario presented here is entirely feasible. This new understanding of electron-phonon scattering and how it limits Q at low temperatures along with the verification of Landau-Rumer limited Q at room temperature provide us with a more complete picture of acoustic attenuation for silicon micromechanical resonators operated at frequencies higher than 1 GHz.

CHAPTER 4

THE RESONANT JUNCTION TRANSISTOR

4.1 Motivation

In Chapter 2, the use of pn-diodes to efficiently actuate and sense mechanical motion at UHF and SHF frequencies has been demonstrated. Such resonators use a very simple SOI process to achieve resonators with extremely high *Q* approaching the silicon material limits at room temperature, resulting in a record-high silicon *f*-*Q* product. While the high *Q* is certainly of interest for certain applications, there are a few drawbacks associated with the use of pn-diode internal transduction. Many of these drawbacks are inherent to electrostatic transduction and also appear in similar resonators (e.g., air-gap or dielectrically transduced resonators). The most significant of these is the large parasitic feedthrough signal which desensitizes the output current to the acoustic resonance. As we have seen in Chapter 2, many transduction methods become increasingly inefficient at high frequencies, resulting in large motional impedances. When a resonator is operated in an ideal two-port configuration as in Figure 4.1(a), this large motional impedance shows up simply as insertion loss, but the typical second-order resonant response is still retained. However, if there are any routing parasitics between the body of the resonator and the ground plane, a direct feedthrough path from input to output is formed through the transduction capacitances (Figure 4.1(b)). The ratio of impedances between this feedthrough path Z_o and the motional impedance R_X determines whether or not a clear resonant response will be seen. At high frequencies, the impedance of the feedthrough path becomes much smaller than that of the motional impedance, since it is mostly capacitive and thus decreases with frequency, while the motional impedance tends to increase, hiding the

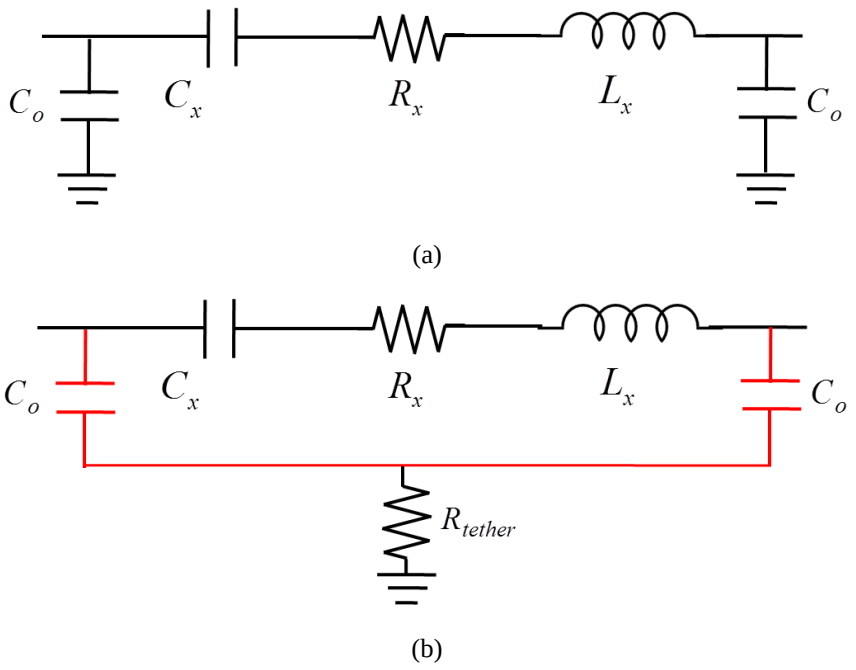

Figure 4.1. (a) Equivalent circuit model for ideal two-port configuration. (b) Equivalent circuit model including feedthrough path through the transduction capacitors (highlighted in red) when resistance is added on the ground plane.

resonant peak in the feedthrough signal, as seen in Figure 4.2. The solution to the problem, however, is not to simply reduce the transduction capacitances, since they also need to be large for efficient electromechanical transduction. Herein lies the main drawback of electrostatic transduction and its limitations for high frequency operation. This is also true for the pn-diode internally transduced resonators, as (53) and (58) indicate that a high symmetric doping concentration and subsequently large depletion capacitance is necessary for efficient transduction.

One possible way to mitigate this feedthrough is to use differential signaling or some variation thereof to cancel these currents at the output [102], [103]. Indeed, a similar pseudo-differential method was used to observe the resonant peak for the devices in Chapter 2. However, there are certain cases where single-ended signaling is desirable for a number of reasons, such as in extremely area or power-limited systems. Also, generating differential signals at RF frequencies on-chip is quite complicated.

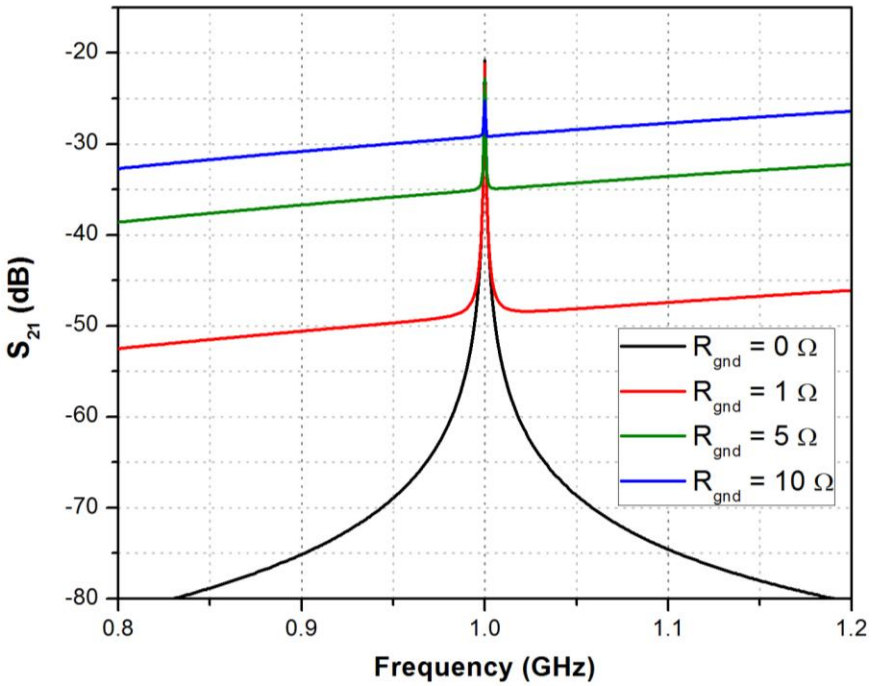

Figure 4.2. S_{21} plots of equivalent circuit model shown in Figure 4.1, illustrating the effect of ground plane resistance on increasing the feedthrough signal and decreasing the resonant peak height. These simulations use R_X = 1 kΩ, Q = 2500, and C_0 = 1 pF while ground plane resistance R_{gnd} varies between 0 and 10 Ω.

Therefore, a method of feedthrough mitigation suitable for single-ended signals is still needed. The main challenge in this case arises because a complimentary signal is not available, meaning that any means of reducing the feedthrough must employ changes to the feedthrough path. With the typical two-port setup, this problem largely becomes a fabrication challenge in trying to minimize the routing resistance to the ground plane because of the tradeoffs involved with modifying the transduction capacitances. In response to this problem, recent work has focused on using different methods for both actuation and sensing to break the feedthrough path. A large majority of this work uses optical signals for transduction, either by using optically-induced forces to actuate mechanical motion [104], [105] or by using mechanical motion to modulate the characteristics of an optical system [106]. While these examples demonstrate very good performance for RF MEMS resonators, the requirement of an optical source

currently limits their utility in monolithically integrated systems. For such applications, electrical actuation and sensing methods are still necessary.

One method of breaking the direct feedthrough path while still using electromechanical transduction is to use the piezoresistive effect to sense the output motional current, as in [107]. The piezoresistive effect is the phenomenon where an applied mechanical strain causes a change in the electrical resistivity of a crystalline material [108]. This effect has been employed in many types of sensors, most notably pressure sensors [109], [110]. To make use of this effect in resonators, such devices will typically have an actuation capacitor through which mechanical motion is induced using electrostatic excitation and a current channel located in a region of large mechanical strain, where one end is grounded and the other end is the output node. A DC voltage bias is applied across the channel so that the desired current can flow. A schematic of such a device is shown in Figure 4.3. It can be seen from this schematic that the main feedthrough path is through the actuation capacitance and piezoresistive channel. Since the channel resistance can be made large, the feedthrough signal is now both substantially reduced and nearly independent of frequency, resulting in substantially less feedthrough current at frequencies greater than 1 GHz compared to typical electrostatically transduced two-port resonators. In addition, the channel current can be controlled by introducing a transistor gate and may allow for the possibility of self gain, as briefly introduced in Chapter 1. The phase properties of a piezoresistive sensing also offer another method of electrically rejecting the feedthrough signal. Since the phase difference between the electromechanically actuated strain – and consequently the output motional current – and the input voltage signal is 90 degrees, a quadrature demodulation scheme may be used to distinguish the mechanical signal from the feedthrough. This is not possible with the conventional

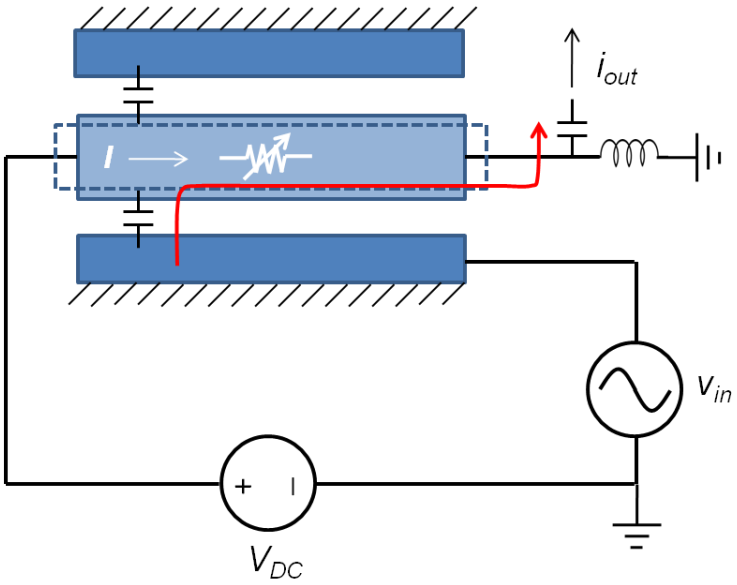

Figure 4.3. Schematic of a capacitively actuated, piezoresistively sensed longitudinal bulk acoustic resonator. Deformed mode shape is outlined with the dotted line. A DC bias is applied across both orthogonal ends to induce static current and this current is modulated by the change in resistivity of the material due to strain from mechanical actuation. The direct feedthrough path in this case is shown in red.

two-port electrostatic resonators because the feedthrough and mechanical signals both have the same phase.

In this chapter, we present a pn-diode actuated, piezoresistively sensed silicon RF MEMS resonator that maintains the high *Q* and high efficiency at UHF frequencies of pn-diode internal transduction. Experimental results show that the resonant peak is clearly seen even when measured in a completely single-ended environment, indicating that the feedthrough signal is significantly reduced compared to typical capacitive two-port measurements of RF MEMS resonators. In addition, as a means of controlling the channel current, a p^+-Si gate is incorporated into the structure to create a junction field effect transistor (JFET). This has a number of benefits over using MOSFETs to control the current, the most significant being that JFETs generally have much lower noise and larger piezoresistive coefficients [111], [112]. This is primarily due to the fact that the majority of current flow in JFETs occurs in bulk silicon, as opposed to surface conduction in MOSFETs. In particular, it has been speculated that

trap states that form due to lattice discontinuities at the silicon-oxide interface contribute significantly to the flicker noise of MOSFETs [113]. Without such an interface, it has been verified that JFETs have much lower levels – theoretically zero – of flicker noise [114]. This is especially important in the context of oscillator design since flicker noise typically limits the close-to-carrier phase noise [115].

The remaining sections of this chapter will describe the principle of operation of the proposed resonant junction transistor (RJT). In particular, the theory of piezoresistive sensing will be discussed and a brief overview of the junction field effect transistor will be included. These principles will be applied specifically to the RJT presented in this dissertation to obtain an equivalent circuit model. This will be followed by the step-by-step fabrication process flow and finally, experimental results will be presented, showing the outstanding performance of such resonators at gigahertz frequencies.

4.2 Device Structure and Principle of Operation

The RJT utilizes pn-diode internal actuation to excite resonance in the mechanical structure and the resulting sinusoidal modulation of the JFET channel resistance via the piezoresistive effect is used to produce a time-harmonic output motional current which is sensed at the output node. An SEM and cross-section schematic of the device with all four terminals labeled is shown in Figure 4.4(a) and (b), respectively. In the case of the RJT, instead of a sensing junction, there is an embedded JFET structure shown on the right. A clear contrast can be seen between the lightly shaded p^+ gate and actuation junction input and the darker n^+ source and drain regions in Figure 4.4(a). This device is excited in the thickness extensional mode (Figure 4.4(c)) via the actuation junction on the left, as was the case for the pn-diode internally transduced

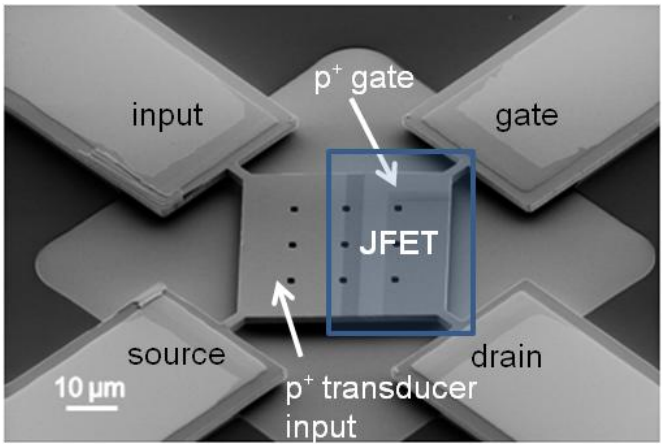

(a)

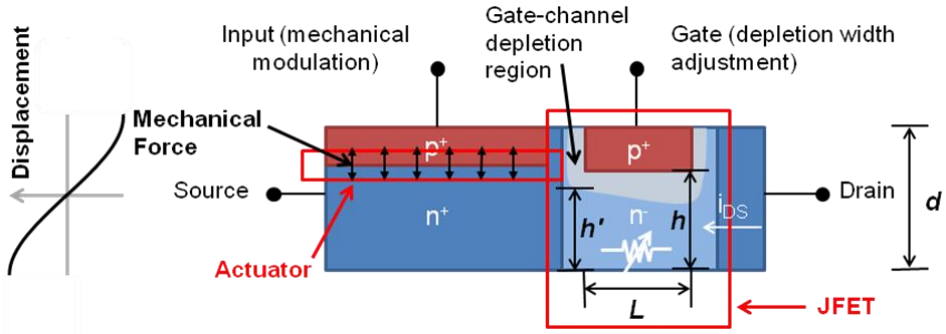

(b)

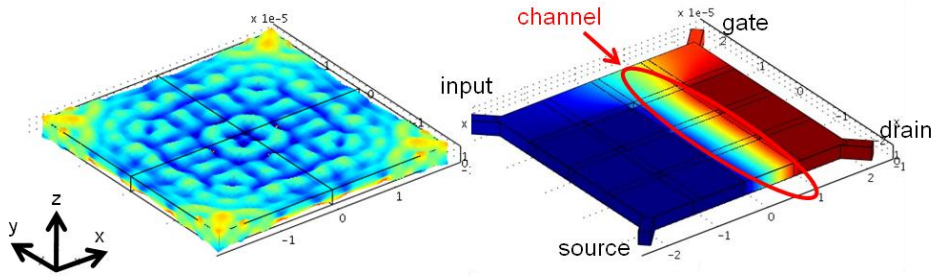

(c)

(d)

Figure 4.4. (a) Top view SEM with all four terminals labeled. Lightly contrasted regions denote areas of p-type doping. (b) Cross-section of resonator structure with embedded JFET showing the actuation junction on the left and the JFET sensing element on the right. Induced mechanical displacement is shown on the left. (c) COMSOL simulation results of the fundamental thickness extensional mode shape highlighting the z-displacement. Irregularities in mode shape are due to etch holes. (d) Voltage distribution between source and drain contacts indicating that current flow is confined to channel placed at location of maximum displacement.

resonators of Chapter 2. The distortion in the mode shape seen in Figure 4.4(c) is due to the etch holes included in the COMSOL simulation. The method of actuation has

already been described in detail in Chapter 2 and thus will not be discussed here. This section will instead focus on the piezoresistive sensing mechanism and JFET operation.

4.2.1 The Junction Field Effect Transistor

Although the MOSFET has emerged as the transistor of choice in many applications, other field effect transistors are still used in niche applications, especially those that require extremely low noise, high output power, high frequency, or any combination of the above. One such device is known as the junction field effect transistor, which finds use in a number of different applications, e.g., as op-amp input stages, in radiation-resistant systems, etc. The cross section of the n-channel JFET used in the RJT is shown in the right side of Figure 4.4(b). The device consists of a single junction between the highly doped p^+ gate and the underlying n^- channel. This structure can be placed above a p-type substrate if fabricated in a bulk silicon process or the buried oxide (BOX) layer of an SOI wafer, as in this particular case. The source and drain regions are also highly n^+ doped to create good ohmic contacts to their respective metal electrodes. The main conducting channel is nothing more than a silicon resistor between source and drain, with resistance determined by the transistor width *W*, channel length *L*, and the channel thickness taking into account the depletion region *h'*. While the width and length of the transistor are determined by lithography and are thus unchangeable for a given device, *h'* is dependent on the width of the depletion region, which can be tuned by the gate voltage. Therefore, for small drain biases, the JFET is simply a voltage controlled resistor. As larger reverse biases are applied to the gate ($V_{GS} < 0$), the depletion region of the gate-channel junction increases, narrowing the channel and resulting in a higher resistance between source

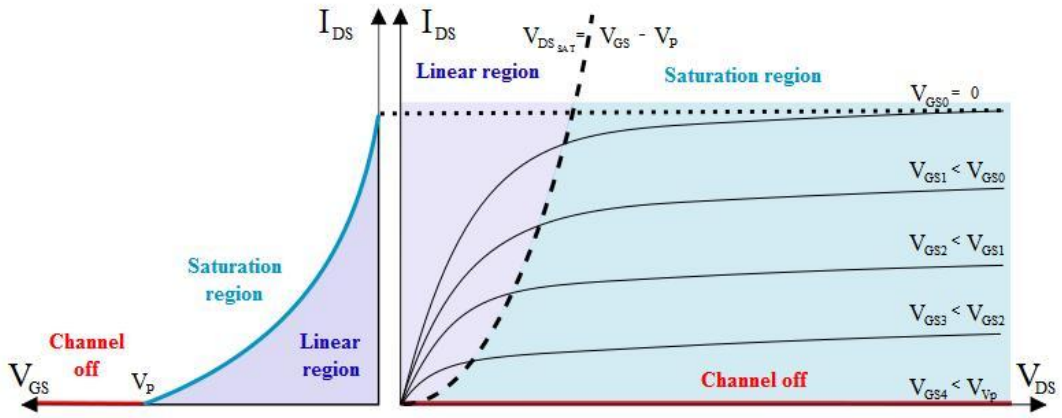

Figure 4.5. I_D-V_{GS} and I_D-V_{DS} characteristics of JFET for different values of V_{GS}. Note only magnitudes of V_{GS} are shown here; V_{GS} is normally negative for n-JFET with p-type gate.

and drain. This is clearly seen in the decreasing slope of the drain current I_D vs. V_{DS} characteristics of this device (Figure 4.5) near $V_{DS} = 0$.

When a bias is applied to the drain, current will begin to flow through the channel and the reverse bias at the drain end will now be larger than that at the source. This means that the depletion width will also be larger at the drain and gradually decrease down the channel. This increase in depletion width at the drain adds to the gate bias to reduce the effective channel thickness and increase the small-signal resistance. Thus, as seen in Figure 4.5, the slope gradually decreases as V_{DS} increases. Eventually, the slope will become zero, which physically means that the channel has now been completely "pinched-off." In other words, the drain bias is now so large that the channel region at the drain end is completely depleted of carriers. At this point, any additional drain bias will be dropped across this depletion region, and thus current will remain nearly constant for $V_{DS} > V_P$, where V_P is the pinch-off voltage (i.e., the drain bias required to just pinch off the channel). Of course, this pinch-off voltage and the saturation current I_{Dsat} depend on the gate reverse bias, since this sets the initial depletion width – higher V_{DS} will result in lower V_P and I_{Dsat}.

Based on the qualitative description above and the I-V characteristics shown in

Figure 4.5, two clearly distinguishable regions of operation can be seen: the linear region where the drain current increases with drain voltage and the saturation region where the current remains relatively constant. For the 1-D case where the potential varies only in the direction of the channel length, an analytic expression for the drain current in the linear region ($0 < V_{DS} < V_{Dsat} = V_P - V_{GS} - \phi_{bi,ch}$) is given by [116]

$$I_D = I_P\left[\frac{V_{DS}}{V_P} - \frac{2}{3}\left(\frac{V_{DS}+V_{GS}+\phi_{bi,ch}}{V_P}\right)^{3/2} + \frac{2}{3}\left(\frac{V_{GS}+\phi_{bi,ch}}{V_P}\right)^{3/2}\right]. \tag{92}$$

Here, I_P is given by

$$I_P = \frac{\mu_n e^2 N_{ch}^2 h^3}{2\varepsilon_{si}\varepsilon_0}\frac{W}{L_{ch}} \tag{93}$$

and V_P can be expressed as

$$V_P = \frac{eN_{ch}h^2}{2\varepsilon_{si}\varepsilon_0}. \tag{94}$$

In (92)-(94), N_{ch} is the channel doping concentration, h is the full thickness of the n-type channel (excluding the depletion region due to the gate-channel junction) as seen in Figure 4.4, μ_n is the electron mobility, L_{ch} is the channel length, and $\phi_{bi,ch}$ is the built-in potential of the gate-channel junction. Once V_{DS} increases beyond V_{Dsat}, the JFET enters the saturation region, where the current is nearly constant with V_{DS}. This saturation current is equal to

$$I_{Dsat} = I_P\left[\frac{1}{3} - \frac{V_{GS}+\phi_{bi,ch}}{V_P} + \frac{2}{3}\left(\frac{V_{GS}+\phi_{bi,ch}}{V_P}\right)^{3/2}\right]. \tag{95}$$

Ideally, this current will remain constant regardless of V_{DS}. However, for any practical device, there will be a slight dependence on drain bias, as seen in Figure 4.5. The origins of this effect are exactly the same as the channel length modulation in MOSFETs: increasing the drain bias beyond V_{Dsat} pushes the depletion region further into the channel, slightly reducing the channel resistance and increasing the drain current. For even higher drain biases, the current will rapidly increase beyond $V_{DS} = V_{BR}$, which occurs due to the reverse breakdown between the gate-drain junction

where the electric fields are highest. It should be noted that this reverse breakdown phenomenon is the main limiting factor in the spacing between the p^+ gate and the n^+ source/drain contacts. Some variations make use of an oxide trench or spacer placed between these two highly doped regions in order to increase the breakdown voltage. At the very least, this spacing must be larger than the channel thickness so that the reverse junction breakdown does not occur before the channel is pinched off. Other designs use a double gate structure to pinch off the channel from both sides before breakdown occurs, but this is not feasible for vertical structure such as the RJT. In any case, this spacing restriction limits the scalability of the JFET as compared to the MOSFET, especially for high frequency operation, and is the main reason why the MOSFET has been able to extend beyond low power digital to RF and mm-wave applications simply by scaling of device dimensions with each technology generation. Fortunately, the frequency of operation of the RJT is not limited by that of the embedded JFET. The JFET needs only to control a static current through its channel, which will be modulated and sensed by the piezoresistive effect as described in the next subsection.

4.2.2 Piezoresistive Sensing

The origins of the piezoresistive effect in semiconductors can be traced back to the electronic band structure of the crystal lattice. In Chapter 3, it was determined that strain in the crystal lattice could significantly affect the phonon dispersion relationships, resulting in phonon-phonon scattering. In a similar manner, mechanical stress or strain in the lattice can also change the electronic band structure of a semiconductor. Specifically for silicon, the energy levels of the normally degenerate six band minima – symmetrically positioned on each principle axis of the lattice – may shift under applied stress such that they are no longer degenerate. Depending on the

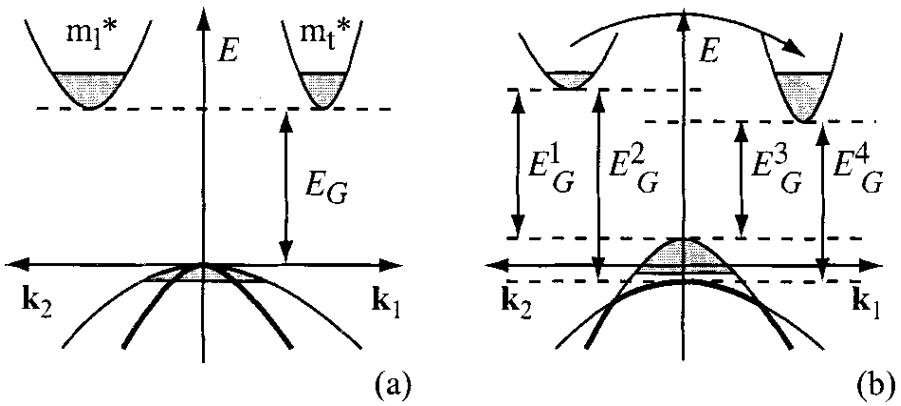

Figure 4.6. Illustration of the band structure of silicon (a) without stress and (b) with stress. The wavenumbers k_1 and k_2 point in the (100)-direction. E_G is the bandgap of silicon, which splits under applied stress resulting in a movement of charge from one valley (with effective mass m_l^* to another with effective mass m_t^*. This changes the overall effective mass and thus the carrier mobility. Reproduced from [108].

orientation of the stress, the band minima (also known as valleys) along a specific axis will slightly increase in energy, while those in the orthogonal directions will slightly decrease [108]. Since the distance between the Fermi level and the energies of the band minima determine the electron concentration, valleys that increase in energy will decrease in concentration, while valleys that decrease in energy will increase in electron concentration (Figure 4.6). The most immediately obvious consequence is a change in the total carrier concentration. Since the electrical conductivity σ of an n-type semiconducting material is given by $\sigma = e\mu_n n$, where n is the electron concentration, stress-induced changes in n will alter the conductivity of the material. However, this amount is small for doped semiconductors since overall charge neutrality requires that the electron concentration be approximately equal to the doping concentration.

More significant than possible changes in the electron concentration are changes in the electron mobility μ_n which may occur due to this shifting of electrons between valleys. The electron mobility for a semiconducting material is given by

$$\mu_n = \frac{e\tau_e}{m_e}. \tag{96}$$

In (96), τ_e is the electron scattering time and m_e is the conductivity effective mass. Both quantities are to be distinguished from the thermal phonon scattering (relaxation) time τ_{th} and density of states effective mass m_e^* presented in Chapter 3. The conductivity effective mass m_e is of interest here since its value is determined by the relative concentration of electrons in each valley. When there is no applied stress, all six valleys are degenerate and thus all have equivalent electron concentrations. In this case for silicon,

$$\frac{1}{m_e} = \frac{1}{3}\left(\frac{1}{m_l} + \frac{2}{m_t}\right). \tag{97}$$

Here, m_l and m_t are the longitudinal and transverse effective electron masses. As their names imply, they each represent the inertial effects of an electron in a single valley when the applied electric field is parallel or perpendicular, respectively, to its direction of motion. The expression in (97) is just a weighted average of the effective masses of each valley. When an external strain is applied and the degeneracy lifted, the electron concentration in each valley is now different, and thus the mass contribution of each valley to the total conductivity effective mass is different. This appears as a change in the electron mobility, which is the dominant contribution to the piezoresistive effect.

The fractional change in the resistivity per unit stress can be quantified by the piezoresistive tensor π_{ij}. For materials with cubic symmetry, this second-order tensor greatly simplifies to a 6×6 matrix with only 3 distinct values, such that

$$\begin{bmatrix} \Delta\rho_1/\rho_0 \\ \Delta\rho_2/\rho_0 \\ \Delta\rho_3/\rho_0 \\ \Delta\rho_4/\rho_0 \\ \Delta\rho_5/\rho_0 \\ \Delta\rho_6/\rho_0 \end{bmatrix} = \begin{bmatrix} \pi_{11} & \pi_{12} & \pi_{12} & 0 & 0 & 0 \\ \pi_{12} & \pi_{11} & \pi_{12} & 0 & 0 & 0 \\ \pi_{12} & \pi_{12} & \pi_{11} & 0 & 0 & 0 \\ 0 & 0 & 0 & \pi_{44} & 0 & 0 \\ 0 & 0 & 0 & 0 & \pi_{44} & 0 \\ 0 & 0 & 0 & 0 & 0 & \pi_{44} \end{bmatrix} \begin{bmatrix} T_1 \\ T_2 \\ T_3 \\ T_4 \\ T_5 \\ T_6 \end{bmatrix}. \tag{98}$$

In (98), T_j is the stress tensor and $\Delta\rho_i/\rho_0$ is a tensor representing the fractional change in resistivity. The values of π_{ij} depend on doping type, concentration, and temperature.

Table 4.1. Piezoresistive coefficients for low-doped silicon (< 10^{17} cm^{-3}) at room temperature [117]. Units are 10^{-11} Pa.

	π_{11}	π_{12}	$2\pi_{44}$
Si(p)	6.6	-1.1	138.1
Si(n)	-102.2	53.4	-13.6

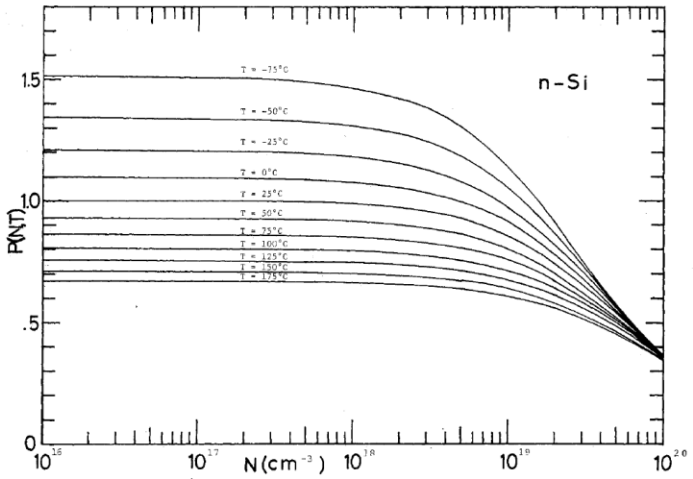

Fig. 8. Piezoresistance factor $P(N, T)$ as a function of impurity concentration and temperature for n-Si.

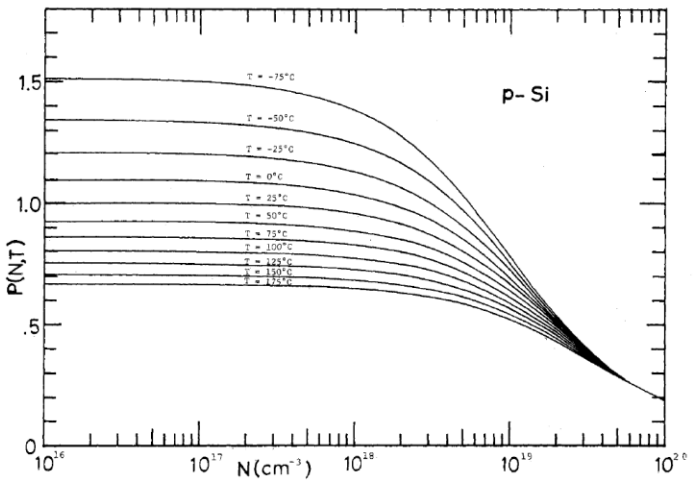

Figure 4.7. Piezoresistance factor $P(N,T)$ (where $P(N,T) = \pi_{ij}(N,T) / \pi_{ij}(\text{undoped},T = 300\text{ K})$; here $\pi_{ij}(N,T)$ is the doping and temperature dependent mobility) plotted as a function of doping concentration for various temperatures. The top figure is for n-Si and the bottom for p-Si. Data shows that $P(N,T)$ decreases with increasing temperature and with increasing doping concentration for both p-type and n-type silicon. Reproduced from [117].

The difference between n-type and p-type single-crystal silicon are shown in Table 4.1, while the dependence on doping concentration and temperature can be seen in Figure 4.7. This figure shows that piezoresistivity decreases with increasing doping

concentration for both n and p-type silicon [117], providing another reason to limit the channel doping in order to maximize the piezoresistive sensing efficiency. From (98), we can obtain simplified piezoresistive coefficients for the case of uniaxial stress: the longitudinal and transverse piezoresistive coefficients π_l and π_t. In the case of the RJT, the actuated stress is mostly in the (001)-direction, making π_t the dominant piezoresistive coefficient for in-plane current. In addition, π_t depends on the orientation of the current with respect to the uniaxial stress as seen in Figure 4.8. This figure shows that for n-Si with stress in the (001)-direction, the current flow should be parallel to another principle axis (i.e., (100) or (010) directions) to maximize the piezoresistive sensitivity. Thus, the RJTs are all designed such that the channels are oriented parallel to the (100)-direction, in which case $\pi_t = \pi_{12}$.

Eqs. (93) and (95) indicate that the saturation current in the JFET channel is directly proportional to μ_n, and thus modulation of the mobility via actuated stress would result in an output motional current. However, since the stress throughout the channel is not uniform but sinusoidal for the thickness longitudinal mode, the effective mobility modulation must be weighted by the stress at a particular position z in the thickness of the channel. Then the output motional current i_{out} can be expressed as

$$i_{out} = \frac{\Delta\mu_{n,eff}}{\mu_n} I_{Dsat} \tag{99}$$

and $\Delta\mu_{n,eff}/\mu_{n0}$ is the average change of the electron mobility throughout the channel thickness $0 < z < h'$. For small strains, the approximation $\Delta\rho_i/\rho_0 \approx \Delta\mu_{ni}/\mu_n$ is valid. Then the effective fraction change in mobility is given by the integral

$$\begin{aligned} \frac{\Delta\mu_{n,eff}}{\mu_n} &= \frac{1}{h'}\int_0^{h'} \pi_t T_1 dz \\ &= \frac{1}{h'}\int_0^{h'} \pi_{12} E_{[001]} \varepsilon_z(z) dz \end{aligned} \tag{100}$$

Eq. (100) shows the general response of the electron mobility to any arbitrary strain in

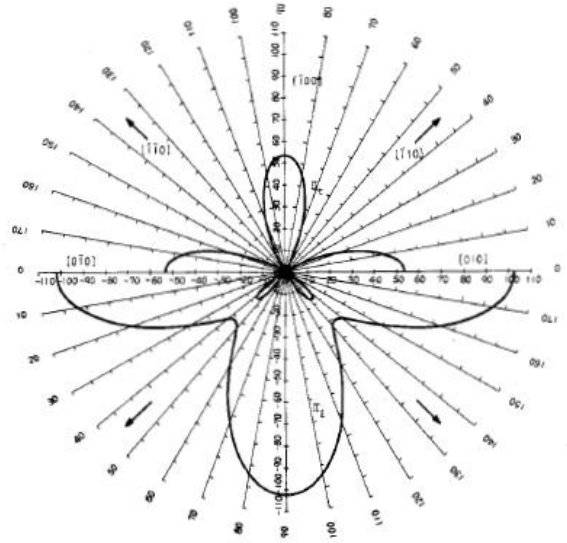

Figure 4.8. Piezoresistive coefficients in the (001)-plane of n-Si at room temperature. Units are in 10^{-11} Pa. The top half of the polar plot shows the transverse piezoresistive coefficient π_t while the bottom half shows the longitudinal piezoresistive coefficient π_l. Reproduced from [117].

the z-direction $\varepsilon_z(z)$. When the thickness longitudinal resonant mode is excited in the structure as in the pn-diode transduced resonators of Chapter 2, (100) can be expressed as

$$\frac{\Delta\mu_{n,eff}}{\mu_n} = \frac{1}{h'}\int_0^{h'} \pi_{12} E_{[001]} \frac{n\pi}{d} U_o \sin\left(\frac{n\pi z}{d}\right) dz \tag{101}$$

Here, U_o is the resonant displacement amplitude. The final result for the output motional current at resonance is then

$$i_{out} = 2\pi_{12} E_{[001]} \frac{U_o}{h'} \sin^2\left(\frac{n\pi}{d}\frac{h'}{2}\right) I_{Dsat} \tag{102}$$

Note in this expression the sinusoidal term containing *h'*. This term indicates that to maximize i_{out}, *h'* must be an odd number of half-wavelengths. For the fundamental thickness longitudinal mode, this means that *h'* should be as large as possible (i.e, equal to *h*). For this to be true, N_{ch} should be large and V_{GS} small. Of course, N_{ch} must be small enough so that the channel can be cutoff before the gate-drain junction breaks down. It should be noted also that this extra boost of i_{out} with *h'* is in addition to the increase in I_{Dsat}; increasing *h'* is more effective at increasing i_{out} than simply through

other means of increasing I_{Dsat} such as increasing W or reducing L. Increasing h' is therefore important for increasing the transconductance to bias current ratio, an important efficiency metric for low-power RF and analog systems.

Another important note to be made is that there is no phase shift between the displacement and the output current. This is in contrast to typical electrostatic sensing which detects the displacement current through a capacitor, which contributes the 90° phase shift between displacement and output current. This additional phase shift present in electrostatic sensing combines with the 90° phase shift between the input actuation voltage and the displacement to result in a total phase shift of 0°between the input actuation voltage and the output motional current. On the other hand, if piezoresistive sensing is used, the total phase shift between input actuation voltage and output motional current will be 90°. As previously mentioned, this may be used as a means of distinguishing between the electrostatic feedthrough signal and the motional current.

4.2.3 Equivalent Circuit Model

Combining the theories of pn-diode actuation and piezoresistive sensing, it is possible to create an equivalent circuit model of the RJT as shown in Figure 4.9. This model closely resembles a typical JFET equivalent small signal model with the electrical transconductance g_m and parasitic elements found in the embedded JFET structure. In normal operation, the gate is grounded to shut off the electrical transconductance to avoid overwhelming the mechanical response. In addition to these components, there are two additional elements in the RJT equivalent circuit model: a second dependent current source using the acoustic transconductance g_a and a third-order resonant circuit between the input and the source node. The acoustic

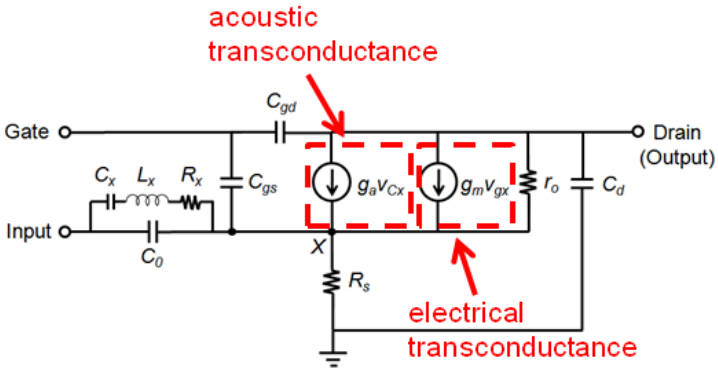

Figure 4.9. Equivalent circuit model of the RJT. The series RLC circuit at the input is an electrical model for the mechanical motion. The control voltage for the dependent current source modeling the acoustic transconductance is the voltage across C_X of the series RLC circuit. This implicitly takes into account the 90° phase shift and Q amplification of the motion.

transconductance is the main component of interest for the RJT and represents the output motional current that results from the input actuation voltage. The third-order resonant circuit models the mechanical resonance that is excited by the input actuation voltage. Note that the current source containing the acoustic transconductance is dependent on the voltage across the capacitance of the series RLC circuit v_{Cx}. Specifying the dependent current source in this way incorporates both the 90° phase shift between input actuation voltage and output motional current and the Q amplification due to resonance, as seen in the expression below.

$$v_{Cx} = \frac{v_{in}}{1 + j\,\omega/(Q\omega_o) - (\omega/\omega_o)^2} \tag{103}$$

This expression is equal to $v_{in}Q/j$ at resonance $\omega = \omega_o$. The acoustic transconductance g_a can then be expressed as

$$g_a = \frac{\pi_{12}}{h'}\frac{8d^2}{n^3\pi^3}\frac{A_{j,a}}{A}\frac{eN_a}{z_{d0,a}}\sin\left(\frac{n\pi d_a}{d}\right)\sin^2\left(\frac{n\pi}{d}\frac{z_{d0,a}}{2}\right)\sin^2\left(\frac{n\pi}{d}\frac{h'}{2}\right)I_{Dsat}. \tag{104}$$

The parameters of the actuation junction in Chapter 2 are again used here. As before, we see the sinusoidal terms with dependencies on d_a and $z_{d0,a}$ characteristic of internal transduction. There is now an additional sinusoidal term dependent on h', which indicates that for maximum transconductance, $h' = |2m\text{-}1|d/n$ should be satisfied,

where m is a non-negative integer less than the harmonic mode number n.

As a final note regarding the equivalent circuit model of the RJT, there is one subtlety that exists when comparing the efficiency metrics of piezoresistively sensed resonators and those of conventional electrostatic or piezoelectric resonators. Some may suggest that acoustic transconductance and motional impedance are just reciprocals of each other and that one might as well report $1/g_a$ as the equivalent motional impedance of the RJT or take $1/R_X$ of an electrostatically transduced resonator and call that its acoustic transconductance. While this may be useful when quick comparisons need to be made, it ignores the fact that piezoresistive sensing is inherently unidirectional: a voltage signal applied to the output node does not result in a motional current flowing out of the input node. This is clearly in contrast to typical two-port electrostatic or piezoelectric resonators, which are in fact reciprocal. This feature makes it necessary to formulate an equivalent circuit model in this way, since the behavior of the RJT is most accurately modeled by a frequency-dependent, voltage-controlled current source rather than a simple series RLC circuit.

4.3 Fabrication Process

The RJT devices were fabricated at the Cornell Nanofabrication Facility (CNF) using a six-mask fabrication process. The process flow is described visually in Figure 4.10. We start with an undoped SOI wafer with roughly 2.5 μm device layer thickness. This starting wafer receives a very low dose blanket phosphorus implant (190 keV, 1e12 cm^{-2} dose) to define the channel doping concentration N_{ch} (Figure 4.10(a)). This is followed by a 5 hour anneal in N_2 ambient at 1100°C to achieve a relatively uniform doping concentration of 5×10^{15} cm^{-3} throughout the device layer thickness. Following this anneal, alignment marks are etched through the device layer using a reactive ion

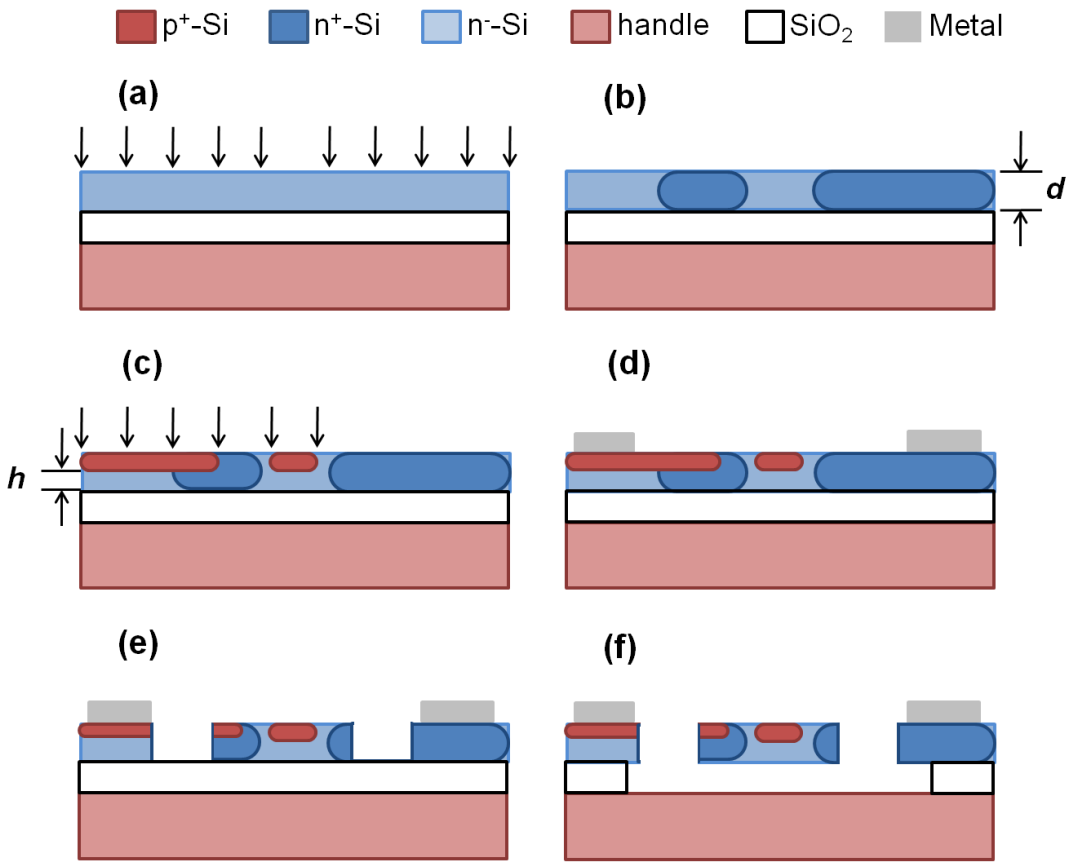

Figure 4.10. Simplified process flow of RJT. (a) Blanket phosphorus implant for channel concentration. (b) Phosphorus solid source diffusion for source/drain definition. (c) Boron implant for JFET gate and pn-diode actuator definition. (d) Metallization for interconnect and pad structures and (e) RIE etch to define resonator geometry. (f) timed HF release.

etch with photoresist mask (not shown). Next, an oxide hard mask is patterned and used to selectively n^+ dope the source and drain regions of the RJT in a phosphorus solid-source diffusion furnace. A pre-deposition diffusion is performed for 25 min. at 1000°C to introduce phosphorus into the doped regions after which a 120 min. soak at 1100°C is performed to drive in the dopants through the entire thickness of the device layer to reduce source and drain series resistance. A separate push-in anneal is performed to limit the donor concentration near the surface since compensation doping must be performed to form the p^+ region of the actuation junction. A surface concentration of less than 5×10^{19} cm^{-3} is thus desired to reliably form the actuation

junction. Figure 4.10(b) shows the wafer after this diffusion step and subsequent removal of the oxide hard mask.

Following this step, a boron implant is performed to simultaneously define both the JFET p^+ gate and the p^+ side of the actuation junction. This implant is a three-step recipe in order to create a continuous p^+ region up to the surface: (1) 90 keV, 4e15 cm^{-2} dose; (2) 45 keV, 3e15 cm^{-2}; (3) 10 keV, 3e15 cm^{-2}. Due to the high implant dose, an oxide hard mask is again used to prevent burning of the photoresist. A rapid thermal anneal (RTA) for 20 seconds at 1100°C (45 second ramp from 300°C) is performed immediately after the implant for dopant activation. The resulting wafer cross-section is shown in Figure 4.10(c). Once the p^+ regions have been defined, interconnects are patterned using lift-off of a 50 nm Cr (for adhesion) and 100 nm Al metal stack as seen in Figure 4.10(d). Both metals are deposited via DC magnetron sputtering with a short ion beam clean beforehand to remove any native oxide that may degrade the electrical contact. This step is followed by a reactive ion etch using a 100 nm Cr hard mask to define the resonator geometry (Figure 4.10(e)). This Cr hard mask is again patterned via lift-off. The reason a Cr hard mask is used is because very small features (i.e., etch holes) and very large regions must be cleared using this etch. If a conventional photoresist mask is used, the tall mask thickness (~2 μm for 2 μm opening) makes the etch rate of the smaller features drastically slower than that of the larger windows, requiring large overetch times that the photoresist mask may not be able to handle. Thus, a thinner masking material that can hold up to long etches is necessary. Characterization of this Cr as a masking material shows that the etch rate of the smaller features is nearly the same as that of the wider openings.

Once the device layer has been patterned and the Cr hard mask removed, a timed buffered oxide etch is used to undercut the buried oxide layer and suspend the mechanical structure and is immediately followed by critical point drying to prevent

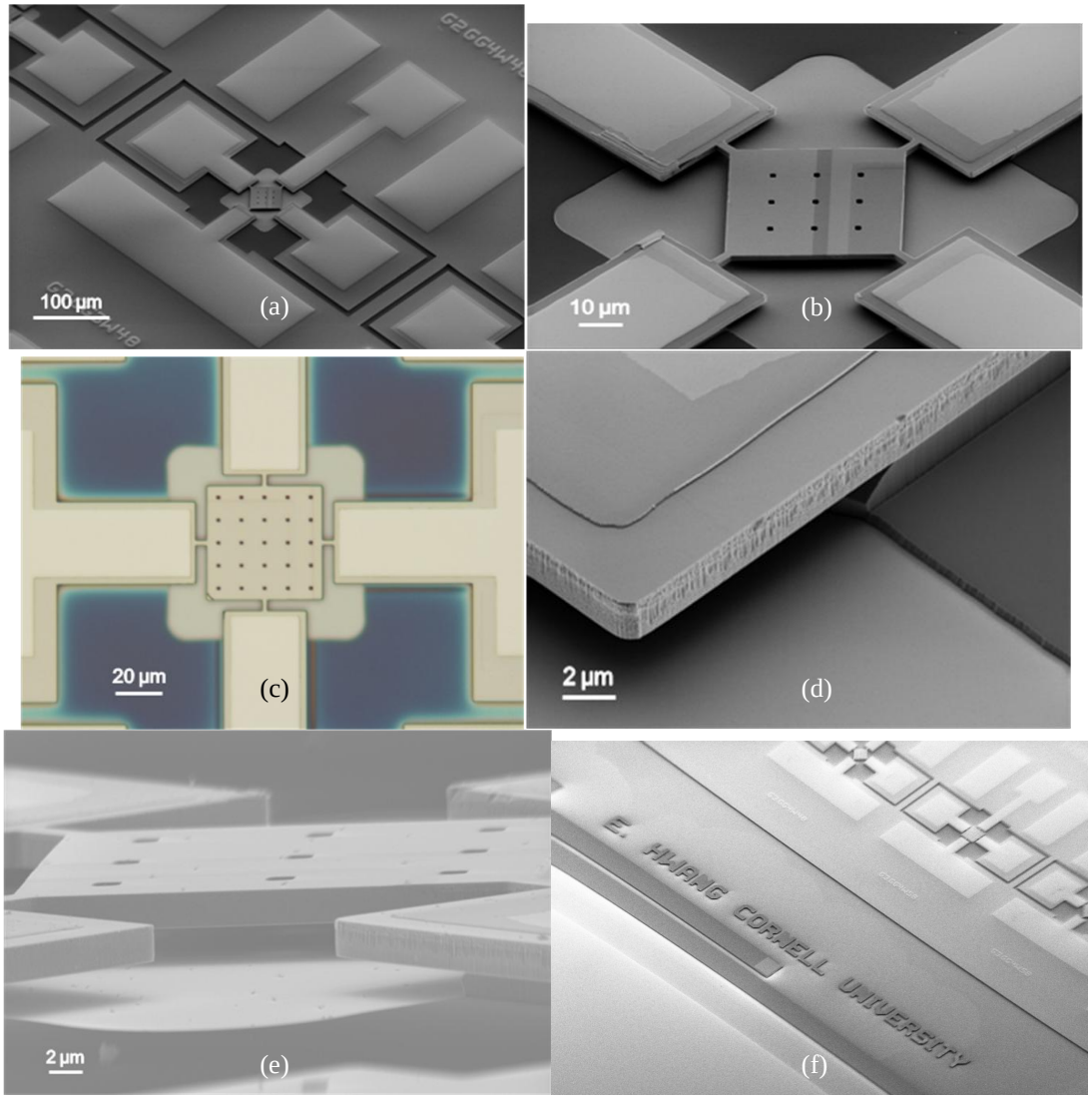

Figure 4.11. SEMs and optical micrographs of the RJTs fabricated in the CNF.

stiction. A photoresist mask is used during this etch to protect the Al interconnect and is removed prior to the critical point drying step. The final process cross-section is shown in Figure 4.10(f). SEMs of the completed RJTs are shown in Figure 4.11, showing clear contrast between the n-type (darker) and p-type (lighter) regions of the device. The undercut buried oxide layer is also clearly seen away from the device. The discoloration of the metal interconnects on the four electrodes are due to slight exposure to HF during the release step. Also, some residue from the interconnect lift-

off is seen at the corners of these electrodes, particularly on the source electrode. While unsightly, this residue does not interfere with the electrical behavior of the device. A large angle tilt SEM (Figure 4.11(e)) is also shown to verify that the mechanical structure was fully undercut by the timed oxide etch.

4.4 Experimental Setup and Results

The experimental verification of the RJT can be divided into two types of measurements: DC measurements for characterization of the JFET I-V characteristics and RF measurements for characterization of the acoustic resonance of the RJT. The experimental setups and results for each will be shown in the following subsections.

4.4.1 DC Measurements

The experimental setup for extracting the I-V characteristics of the embedded JFET in the RJT is shown in Figure 4.12 and is quite straightforward. Data is obtained using wafer-level probing. The source is connected to ground through the GSG probes and all measurement grounds are connected on the wafer in order to minimize ground noise. All three device terminals are connected via triaxial cables to different source measurement units (SMUs) on a Keithley 4200-SCS semiconductor parametric analyzer. The tool is configured to wait 10 ms between measurements to allow any transients to settle before recording the data.

The I_D vs. V_D characteristic for a representative device (L_{ch} = 3 μm, W = 30 μm, L = 30 μm, $x_{S,D}$ = 4 μm) is shown in Figure 4.13(a). Also drawn on the same figure are predicted curves for the drain current based on analytical models (92)-(95) using h = 0.78 μm and N_{ch} = 5.4×10^{15} cm^{-3}. Agreement with experimental data is within 10% when a field-dependent electron mobility model is included [118]. This is necessary

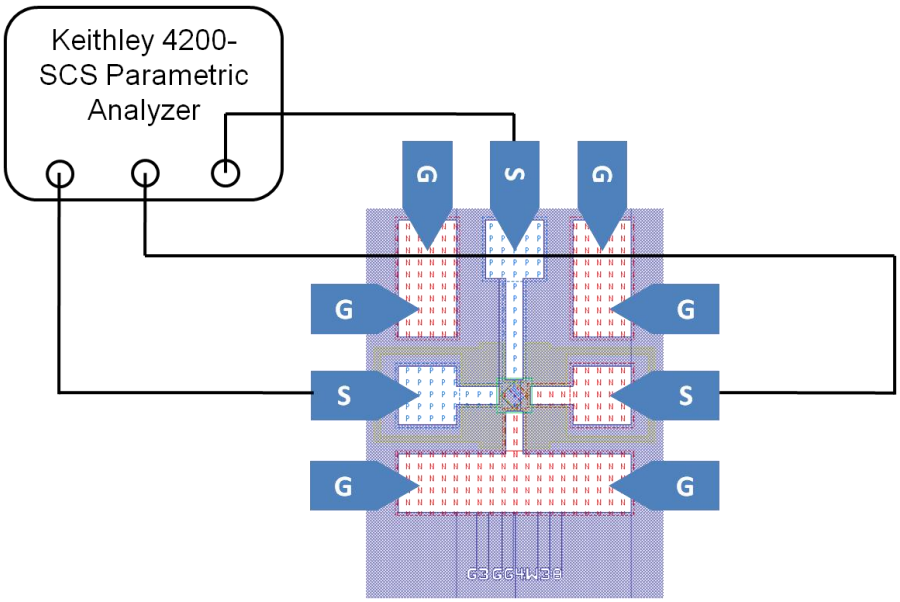

Figure 4.12. DC measurement setup for performing I-V measurements to characterize the embedded JFET in the RJT.

since the electric field within the channel reaches values greater than 1×10^4 V/cm, which is approaching the critical field where velocity saturation occurs. According to Figure 4.13(a), the low-frequency output impedance in saturation is roughly on the order of 70-80 kΩ, while at around V_{DS} = 0 V, the channel resistance varies from 4.5 kΩ for V_{GS} = 0 V to 10.9 kΩ for V_{GS} = -1 V. Figure 4.13(b) shows I_D as a function of V_{GS}, which follows a nearly quadratic relationship. This is also indicated by the nearly linear relationship between the electrical transconductance g_m (= $\partial I_D/\partial V_{GS}$) of the JFET and V_{GS}, as shown in Figure 4.13(c). Figure 4.13(a) and (b) show a change in curvature for I_D vs. V_{GS} and sign for g_m vs. V_{GS} for $|V_G| > 1.25$ V when the drain is biased at 4 V. This is due to reverse breakdown of the gate-drain junction causing an increase in current flowing into the drain node and through this junction rather than through the channel to the source. This analysis shows that accurate prediction of the bias current – a key component of the piezoresistively detected output signal – can be made simply with knowledge of the process parameters and device geometry. This facilitates the

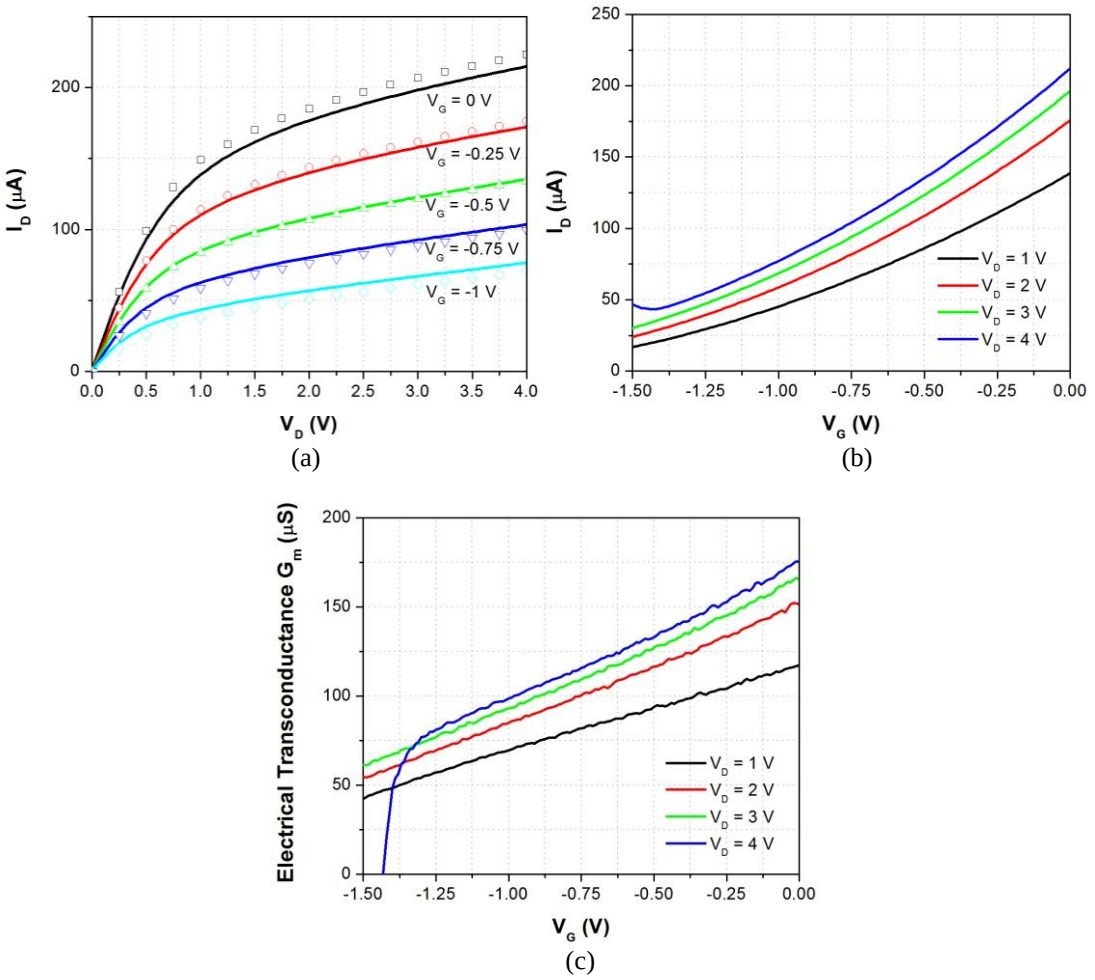

Figure 4.13. (a) I_D vs. V_D measurements for JFET with -0.25 V gate voltage bias step from 0 to -1 V. Plot indicates pinch-off of channel occurs around 1 V for V_G = 0 V. (b) I_D vs. V_G measurements for different values of V_D showing quadratic dependence of I_D on V_G. (c) Electrical transconductance g_m as a function of V_G showing a linear relationship with gate bias.

design and modeling of the RJT for use in larger systems.

4.4.2 RF Measurements

The experimental setup for extracting the acoustic transconductance of the RJT at the resonant frequency is shown in Figure 4.14. In this setup, wafer probing is performed with the DUT placed in a temperature controlled vacuum chamber.

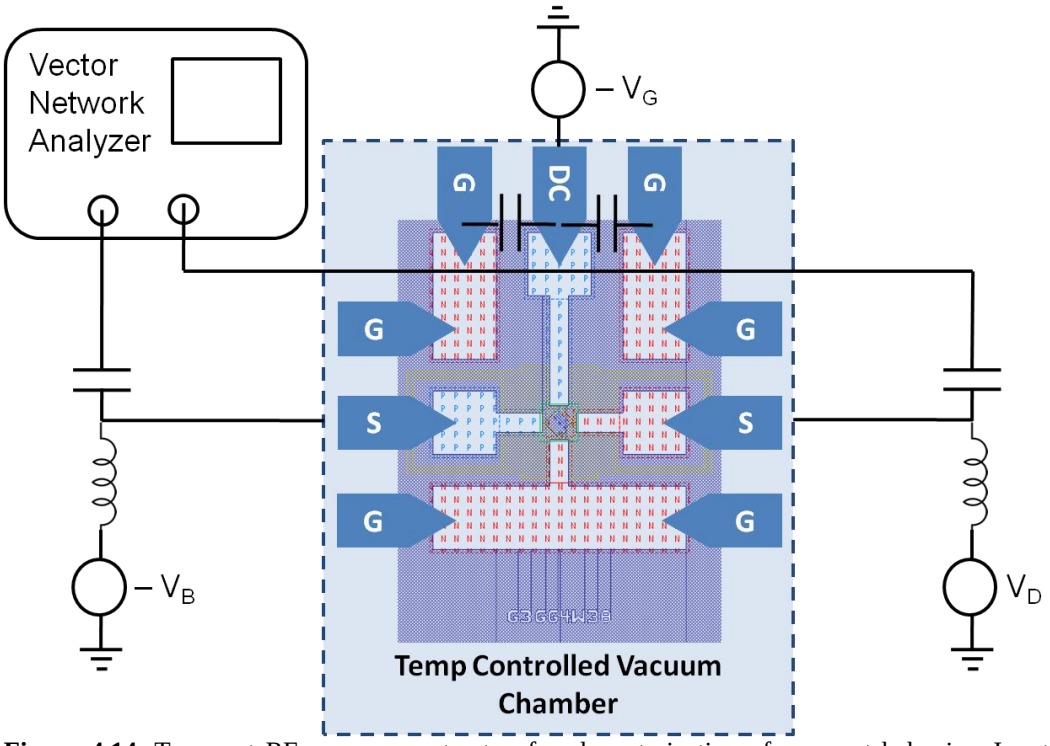

Figure 4.14. Two-port RF measurement setup for characterization of resonant behavior. Input and output (drain) biases are applied through bias-Ts and the gate connection uses controlled impedance probes with ac coupling capacitors placed at the tip. V_B, V_D, and V_G indicate transducer bias voltage, drain bias, and gate bias, respectively.

Calibration using a ceramic calibration substrate is performed to eliminate the loading effects of cables and the probes. SOT de-embedding is applied after measurement to remove the effects of pad capacitance and resistance. Both correction procedures are performed before measurement at each temperature. A vector network analyzer is used to obtain scattering (S) parameters of the DUT, which can be translated into admittance (Y) parameters and then converted to acoustic transconductance using the expression $g_a = Y_{21} - Y_{12}$. The JFET gate is biased through a controlled impedance DC probe with AC coupling capacitors placed at the probe tip. Actuation junction and drain biases are applied through bias-Ts. Measurements results are shown in Figure 4.15. These results show a clear resonant peak at 1.61 GHz with a maximum value of 171 µS. This value is obtained with V_G = -0.3 V and V_D = 2.8 V for a bias current of 143 µA and an actuation junction bias of V_B = -5 V. The resulting acoustic

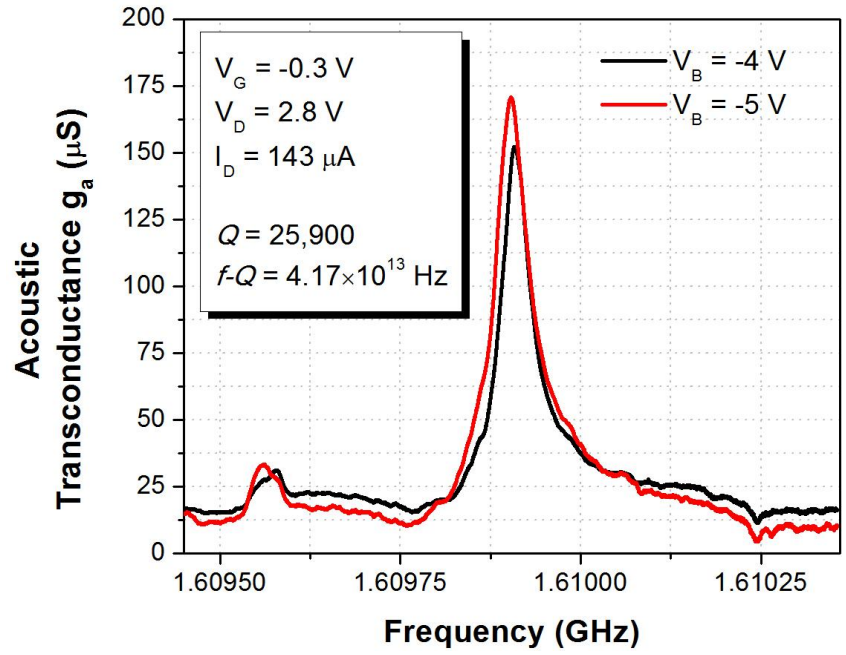

Figure 4.15. Measured acoustic transconductance showing clear resonant peak with Q = 25,900 at approximately 1.61 GHz, showing clear dependence on actuator bias voltage V_B.

transconductance to bias current ratio g_a/I_D = 1.2. Changing V_B to -4 V shows a small shift in the resonant frequency of 4.6 kHz and a reduction in the transconductance to 150 μS, verifying that the resonant peak is due to acoustic resonance excited by the actuation junction. The resonant peaks for V_B = -4 V and -5 V each exhibit Q ~ 28,200 and 29,500, respectively, resulting in f-Q products of 4.54×10^{13} Hz and 4.17×10^{13} Hz (Figure 4.15).

Along with the f-Q products observed from the two-port pn-diode internally transduced resonators from Chapter 2 (6.67×10^{13} Hz), these results provide further experimental verification of the linear dependence of f-Q product with frequency for silicon above 1 GHz (i.e., operation in the Landau-Rumer regime). Questions may arise as to why the f-Q product is not reduced by exactly the ratio of frequencies (1.61/3.72 = 0.43) as would be expected from theory. As such, some may alternatively argue that these devices are operating in the Akhiezer regime (constant f-Q product

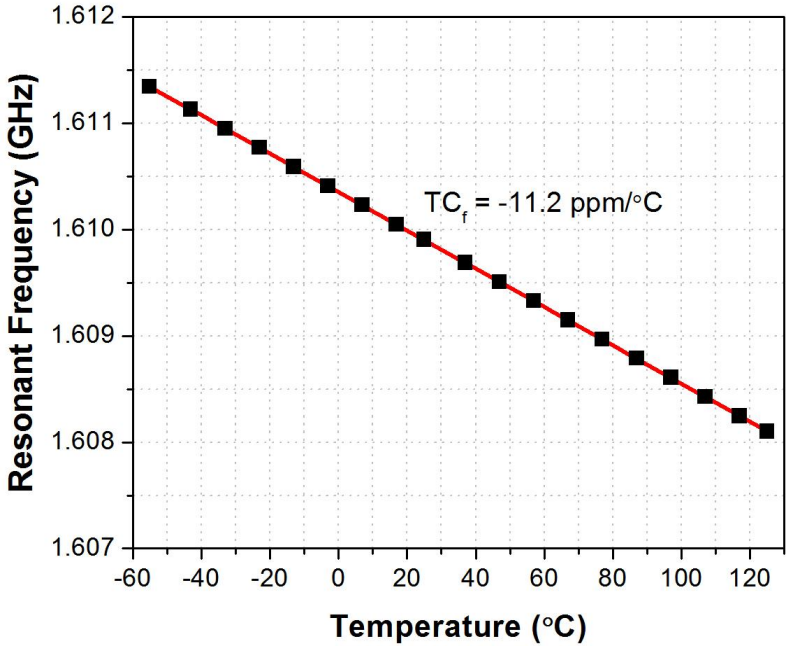

Figure 4.16. Measured resonant frequency as a function of temperature from -55 to 125°C showing a temperature coefficient of roughly -11.2 ppm/°C.

with frequency) with additional acoustic loss in the RJT causing the *f*-*Q* product to be lower. This, however, does not seem like a feasible explanation given knowledge of the other acoustic loss mechanisms that could contribute to the overall *Q*. Electron-phonon dissipation should be reduced since the channel region is not highly doped, in contrast to the devices of Chapter 2 where the entire device layer is highly doped. Since the device layer is thicker in the RJT, surface scattering mechanisms should also be reduced. In addition, the anchors are now located at the four corners of the resonant structure, which should also result in less anchor loss. Thus, the more feasible explanation would be that both devices follow the linear frequency dependence of *f*-*Q* product in the Landau-Rumer regime – the primary acoustic loss mechanism – but the other secondary mechanisms are reduced in the RJT, resulting in a slightly higher *f*-*Q* product.

Temperature dependence of the resonant frequency is also measured from -55ºC to 125ºC and plotted in Figure 4.16. A linear dependence is observed with a negative

slope of -11.2 ppm/K, which is just slightly larger than the temperature coefficient of the pn-diode internally transduced resonators of Chapter 2 (-9.72 ppm/K). Again, the nearly 3× reduction in temperature coefficient relative to typical silicon micromechanical resonators is due to degenerate doping compensation as discussed in Chapter 2. In the RJT, this value may be slightly higher because certain regions (e.g., the JFET channel) of the resonating structure are not as highly doped.

4.5 Conclusion

We have introduced in this chapter a new type of resonant transistor which uses pn-diode actuation and JFET-based sensing to reduce parasitic feedthrough signals that would otherwise overwhelm the signal due to acoustic resonance. The combination of these two methods allows the device to be designed purely by selective doping, which preserves the single-crystal silicon structure and its high *Q*. In addition, the use of a bulk conduction device for FET sensing also increases the piezoresistive properties of the device and thus the acoustic transconductance, which at 171 μS is the highest value for resonant transistors reported to date. Furthermore, the overall efficiency is also improved, indicated by the largest acoustic transconductance to bias current ratio of 1.2 also reported to date. While the performance reported for the current RJT design is impressive in itself, several modifications to the process could further increase the output signal and overall efficiency.

To minimize the number of process steps for the RJT, this work uses the same boron implantation step to define both the p^+ JFET gate and the p^+ input of the actuation junction. The p^+ implant must overcome the already high phosphorus donor concentration in the actuation junction, thus requiring a very high dose implant. This high dose also means, unfortunately, that the p^+ gate will extend very deeply into the

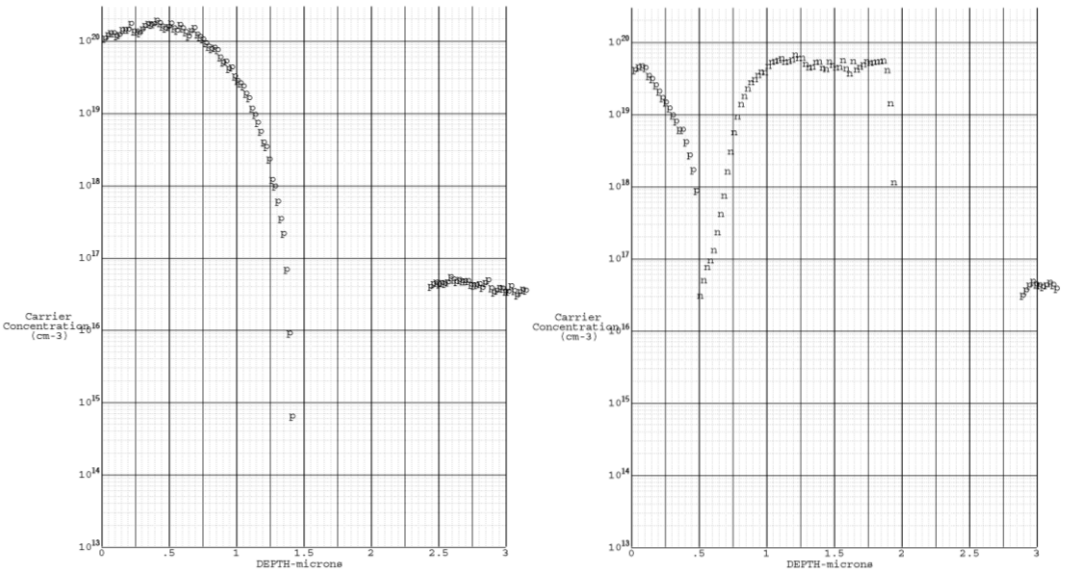

(a) (b)

Figure 4.17. Dopant profiles of (a) JFET gate and (b) input actuator pn-junctions using spreading resistance probe measurements. Measurement results show that the gate implant extends much further into the device layer than for the input actuator with degenerate n-doping. Measurements performed by Solecon Labs.

thickness of the channel, reducing *h'*. This is seen in Figure 4.17 which shows the dopant profile resulting from boron implantation into both n^+ and lightly n-doped silicon, as would be the case for boron implantation into the actuation junction and channel regions, respectively. The value of *h'* = 0.78 μm used in fitting the JFET I-V measurements matches very closely with the results obtained from this dopant profile (for an approximately 2.5 μm device layer). This is undesirable since large *h'* is critical to maximizing g_a/I_D, as discussed previously in this chapter. If it is desired to keep a single implant step, then the possible solutions include increasing the channel doping concentration, reducing the symmetric doping concentration for the actuation junction, or using an actuation junction closer to the surface. The first of these solutions makes it more difficult to pinch off the channel before the gate-drain junction breaks down, while the others both reduce the actuation transduction efficiency. The last method, in fact, is the one used for the current designs.

Immediately, a tradeoff between actuation transduction efficiency and output motional current can be seen here, which limits the overall performance. If instead two separate implants are performed – one for the actuation junction and another for the JFET gate – then this problem can be largely resolved since each implant can be optimized separately. Splitting this into two separate masks also makes it easier to lithographically define and etch these patterns since the very fine JFET gate patterns are now separated from the large actuation junction input patterns. This is, of course, at the expense of increased process steps and alignment layers.

In summary, this chapter has outlined the modeling, design, fabrication, and characterization of the resonant junction transistor, which demonstrates performance that is in the feasible range for use in practical RF systems. A clear path towards improving this performance has also been identified. This may allow for use of the RJT in RF applications that require both high performance and low power consumption such as low-power, high performance oscillators.

CHAPTER 5

FUTURE WORK AND CONCLUSIONS

5.1 Laterally Driven pn-Diode Resonators and RJTs

In addition to the large solution area of quartz or SAW resonators and filters, a related drawback of such off-chip components is that each individual component can only be designed for one specific frequency. It is thus common to see printed circuit boards for mobile communication systems that consist of four or five different quartz or SAW components. In many cases, these external components take up more than half of the total board area. Integrated RF MEMS has been highly touted as a possible solution to shrink the overall solution area due to the possibility of incorporating many different frequencies on a single-chip through lithographic definition of resonator lateral dimensions [17].

In order to make this possible for the devices presented in this dissertation, they must be redesigned to operate in their length or width extensional modes. For the pn-diode internally transduced resonators, this may be achieved by doping through the entire thickness of the device layer and operating in the 3^{rd} order length extensional mode, a configuration which is used in [20]. It is not as straightforward, however, for the RJT due to the greater number of terminals that need to accessed for this device. One might envision a design such as Figure 5.1, which is almost identical to the design in Chapter 4 but with the actuation junction shortened so that there is a source connection for the JFET. Again, this is necessary since the entire thickness of the device layer is p^+-doped to form the junction for lateral actuation. One consideration is that such a design requires two separate boron implants since the JFET gate should not be doped all the way through. Also, this design becomes harder to implement as the

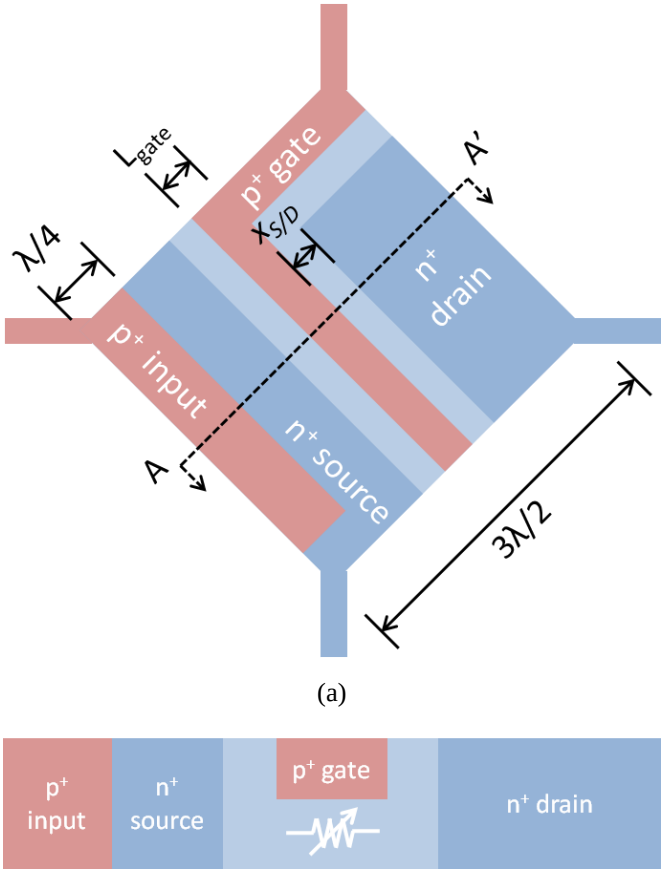

Figure 5.1. (a) Top view illustration of a possible device geometry for exciting the lateral 3rd harmonic length extensional mode for the laterally driven RJT. (b) Cross-section A-A' of the device geometry in (a) showing doping through the thickness of the resonator for the actuation junction but not the JFET gate.

frequency increases since the lateral dimensions must also shrink. Specifically, the bottleneck to scaling of these devices is the spacing between the source/drain regions and the gate $x_{S/D}$, which must be greater than a certain value so that the gate-drain junction does not breakdown before the channel is completely pinched off. In addition, lithography tolerances become increasingly critical at these smaller dimensions, making the design overall more sensitive to process variations. Alternatively, operating at higher harmonics of the length extensional mode may help keep the total device dimensions constant and thus allow the device to fit the minimum required spacing between the gate and source/drain regions, but since the wavelength will still

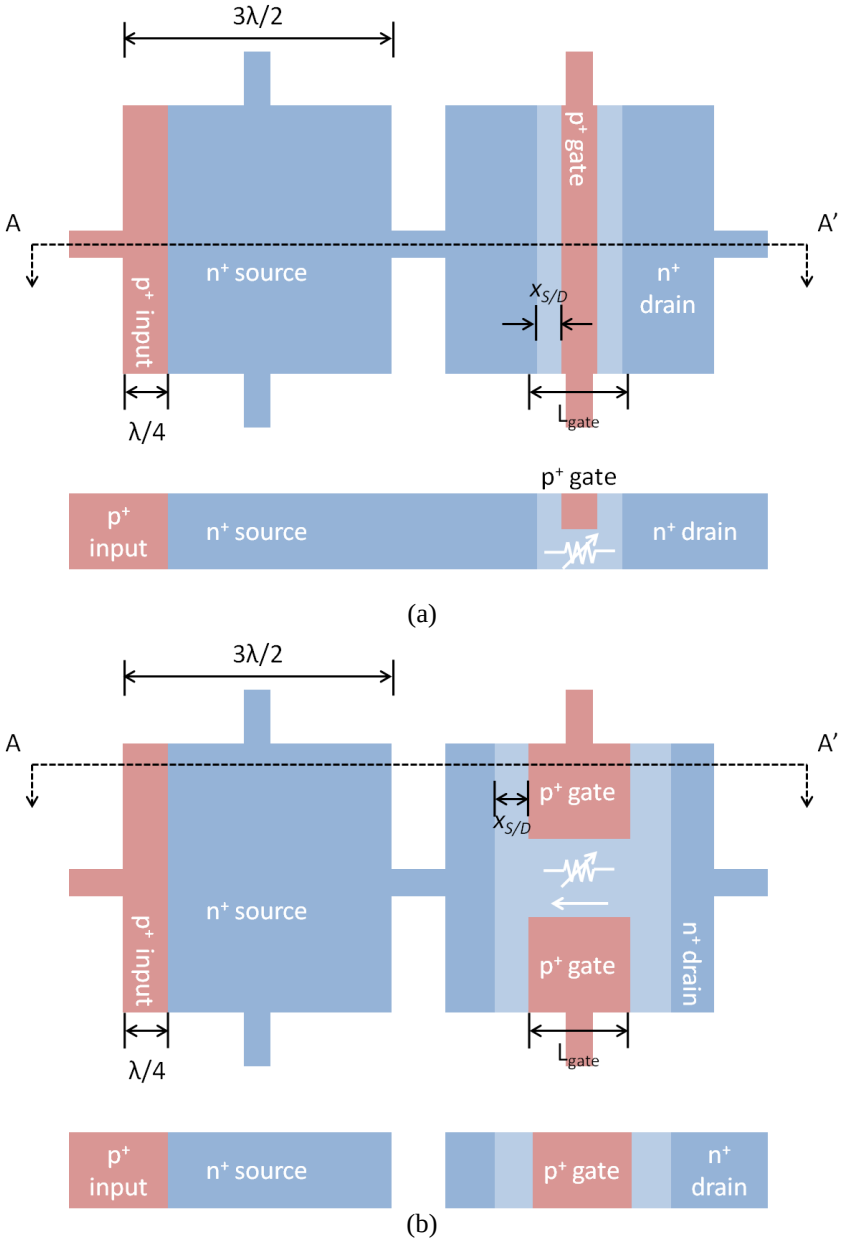

Figure 5.2. (a) Top view illustration and cross-section A-A' of a strongly-coupled dual-resonator device geometry for exciting the lateral 3rd harmonic length extensional mode for the laterally driven RJT. (b) Modified geometry for strongly-coupled dual-resonator RJT requiring only a single boron implant step and using dual-gate configuration for channel pinch-off.

scale with frequency, the placement of the actuation junction will still be just as sensitive to the alignment tolerances of the photolithography tool. In addition, once a target frequency is set, operating at higher harmonics than necessary reduces the actuation transduction efficiency, which is undesirable.

If it is too hard to fit all of these connections into one resonator, it may be possible to get around this by strongly coupling two or more lateral resonators to obtain one single resonant peak while spreading out the terminals between the them. A possible device structure is shown in Figure 5.2(a). Here, the mechanical motion of the left resonator is excited by a lateral pn-diode transducer. This motion is then transferred via the coupling beam to the right resonator, which contains the JFET sensing element. In this structure, it is still necessary to use two separate implant steps. However, it may also be possible to flip the channel to pinch off in an in-plane direction (instead of in the thickness of the device layer) and use a double gate layout to reduce the pinch-off voltage, as shown in Figure 5.2(b). This will reduce the number of implants to one single implant through the device layer thickness. Another benefit of using two coupled resonators is that it is now possible to orient the current flow in the channel and the actuated stress in the resonant structure to be in parallel, which boosts the effective piezoresistive coefficient. These modifications will allow for lithographically defined resonant frequencies without a significant reduction in performance or power efficiency.

5.2 Monolithic Integration of RF MEMS Resonators in SOI CMOS Process

In the introduction, we had delineated the research goals for this dissertation: to identify and develop a high efficiency, high-*Q*, UHF micromechanical resonator technology that can be integrated into a generic, mixed signal technology platform with a minimum number of extra processing steps. The resonators developed in this dissertation are useful for realizing complete RF SoCs only if it can be inexpensively integrated into a process that holds promise for digital, analog, and RF design. Currently, SOI CMOS technology seems to be the only technology that is capable of

high performance across all three categories. As described in Chapter 1, it exhibits lower parasitic capacitances and is capable of integrating higher quality passives due to the use of high resistivity substrates. With the inherent isolation between devices due to the buried oxide layer which reduces crosstalk between digital and RF/analog circuitry, SOI CMOS is a promising mixed-signal technology. If lateral pn-diode internally transduced resonators and RJTs with lithographically defined resonant frequency can be combined with this technology, it could become an even more powerful tool for RF designers to realize integrated, low-power mixed-signal SoCs.

Figure 5.3 shows side-by-side the process steps of a generic SOI CMOS front end process modified from [119] and how the RJT can be incorporated into this process flow. Before discussing the process flow, it should be noted that the device incorporated here is the thickness extensional mode RJT of Chapter 4. Incorporation of a laterally resonant RJT is simple and does not require any changes to the process flow, only a change in the device layer etch mask in CAD. Also, in this process flow an n-JFET is used, but p-JFETs are also possible if the device layer doping is reversed by modifying the p and n implants in CAD. The first step shown is the deposition of a thin pad oxide and nitride layer on top of an SOI wafer with undoped device layer. This is used as a hard mask to achieve straight sidewalls during the device layer RIE step shown as step 2. After the photoresist is stripped, a thick CVD oxide is deposited (step 3) and the wafer is then planarized using chemical-mechanical polishing (CMP) to polish down to the device layer (step 4).

In steps 5 and 6, the active regions (channel doping) for NMOS and PMOS devices are defined through selective ion implantation. These steps may also be used to achieve the desired channel doping for the n-JFETs and p-JFETs. In step 7, the gate oxide is grown and the polysilicon gate layer is deposited. The MOSFET gates are defined in the next RIE step (step 8). For the RJT and JFET devices, the polysilicon

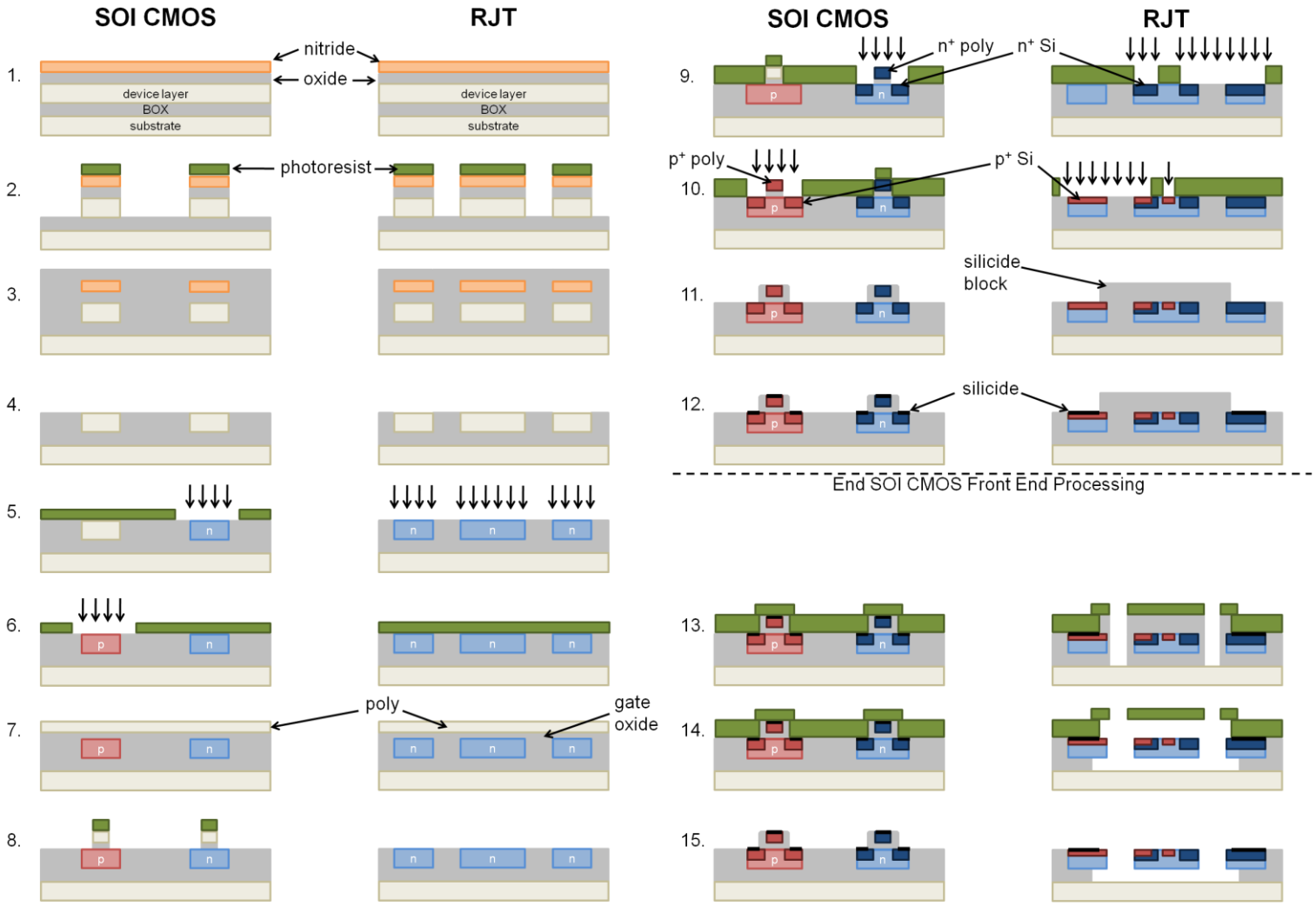

Figure 5.3. Fabrication process flow of SOI RF CMOS process (with silicide block) and RJT showing how the RJT can be completely integrated without modifications to the existing process flow.

and gate oxide layers are completely etched away to maintain the homogeneous single-crystal silicon structure. In step 9, the NMOS source/drain and gate implant is performed. Simultaneously, the n-JFET source/drain regions and interconnects are also defined through this step. Step 10 is the PMOS source/drain and gate implant, which is also used to define the JFET gate and actuation junction input for the RJT. The next step (step 11) creates the MOSFET spacer oxide by CVD oxide deposition and RIE etch. During this step, the silicide block layer typically available in most SOI RF CMOS processes for creating polysilicon resistors is used to keep the oxide on top of the RJT to prevent silicidation, which may cause shorting between the different terminals. Not shown in the process flow here is the source/drain anneal that takes place before the silicide step. In this step (step 12), a metal such as nickel or tungsten is deposited and then annealed to react with silicon and form a silicide. The unreacted metal is then removed using an isotropic wet etch. While silicide is not formed on the RJT due to the silicide block layer, it should be formed on the anchor regions as close to the resonator as design rules allow in order to reduce interconnect resistance. With this, the front end SOI CMOS process is concluded.

After deposition of a few back-end metal interconnect layers, we can proceed with step 13. The figure does not explicitly show the back-end metal layers above the CMOS devices, but they are not relevant here since this portion of the chip will be protected by photoresist for all subsequent processing steps. In step 13, the gap between the resonator and the anchor for the RJT (and etch holes, not shown) is exposed in the photoresist mask and the oxide is etched all the way down to the substrate. This opens up the window for vapor HF release of the resonator structure shown in step 14. Finally, the photoresist mask is removed using an oxygen ash.

It has been shown that the pn-diode internal resonators and RJT devices can be completely integrated into an SOI RF CMOS process without modification to any of

the front end process steps. The only additional processing required is an additional photolithography and etching step followed by a timed vapor HF etch and a final oxygen ash step. It should be noted that this vapor HF etch is not a critical release step since there are no narrow gaps present in the resonator designs. This shows that it is indeed possible to integrate high-*Q*, high frequency resonators in a high volume mixed-signal technology without greatly increasing the manufacturing cost. This technology provides an alternative to typical RF solutions using multiple chips and components for certain applications that require extremely small size and weight.

5.3 On-Chip High Performance MEMS UHF Oscillators and Mixers

As mentioned in Chapter 1, one of the main bottlenecks to completely monolithic RF systems is the lack of a reliable on-chip frequency reference. This function is usually provided by a quartz crystal reference, which cannot be integrated into commercial CMOS processes. In addition, the frequencies of quartz crystals are limited to a few 100 MHz, requiring a phase locked loop (PLL) with relatively large frequency division ratios, adding significantly to the power consumption of the frequency synthesizer. An on-chip frequency reference that can directly output local oscillator (LO) signals up to a few gigahertz, with low power consumption and good stability (phase noise and drift) is thus highly desirable.

All these characteristics can potentially be achieved when the RJT is used as the on-chip frequency reference for such oscillators. Its potential for high frequency and *Q* on an integrated platform has been experimentally demonstrated in this dissertation. The remaining challenge is designing the circuitry around it to sustain oscillations. The possibility of integration into an existing SOI RF CMOS process, as demonstrated in the previous subsection, allows the use of all the knowledge built up around RF

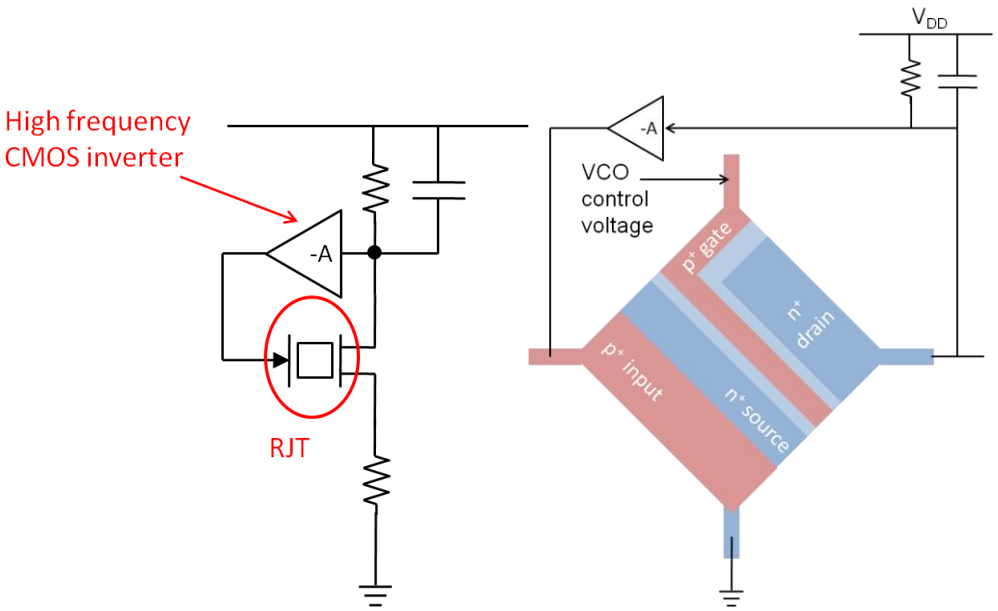

Figure 5.4. (a) Possible schematic and (b) more detailed illustration of the RJT-based UHF low-power oscillator. The high frequency inverter gain stage can easily be implemented in SOI CMOS technology with f_T on the order to tens of gigahertz.

CMOS design in a proven technology, making this problem significantly more tractable. A possible implementation is shown in Figure 5.4. Recall that there is a 90° phase shift between input and output of the RJT. This is taken into account in this schematic by the RC load connected to the output. The resistor here is simply for biasing and the main load presented to the output current at high frequency is the capacitive impedance. The signal then goes through another RF inverting gain stage and then is fed back to the input of the RJT to complete the oscillator loop. Again, we benefit from the fact that there is no need to drive signals off-chip, thus largely eliminating any impedance mismatch and parasitic loading issues in the signal path, especially between the reference and the sustaining circuitry. Also shown in Figure 5.4(b) is a method of tuning the oscillator frequency by adjusting the gate or drain voltage. As we have seen in Chapter 4, it is possible to tune the resonant frequency by adjusting the actuator bias voltage, the tuning in this case is due to a change in the static stress applied to the resonating structure. There are also other ways of achieving

voltage tunability, including adjusting the gate or drain voltage. When these voltages are changed, the drain current as well as the heat dissipated in the structure are also changed. The resulting thermal expansion is small, but is enough to slightly tune the resonant frequency of the RJT. This may prove useful for use in temperature controlled oscillators.

Another RF block that can be easily implemented by the RJT is a mixer, which takes the desired RF signal and demodulates it to baseband or intermediate frequency (IF) to perform signal processing at a lower frequency. Typically, an IF frequency as low as possible is desired. One challenge in RF front end design is frequency planning and maximizing the image rejection ratio (IMRR), which for a commonly used superheterodyne receiver shown is limited by the bandwidth and stopband rejection of available RF filters. This problem arises because mixing also folds in noise from the other image sideband $f_{IM} = f_{LO} + f_{IF}$ into the IF frequency in addition to the signal of interest $f_{RF} = f_{LO} - f_{IF}$ in the process of frequency conversion, as illustrated in Figure 5.5(a). This places a limit on the lower bound of the IF depending on the amount of noise that can be tolerated. The easiest solution is to place a narrowband filter to select just the channel of interest and reject all other spectral components (Figure 5.5(b)). If an ideal brickwall filter is possible, then the IF can be chosen arbitrarily low, making subsequent signal processing easier. Of course, such filters are not practical. If off-chip components are permitted, then higher rejection, narrow bandwidth filters may be available, but this adds significantly to the total size, weight, power, and cost of the system. While RFIC designers have proposed a wide range of solutions to this problem, including I/Q mixing and/or multiple frequency conversion and direct conversion architectures [120], these solutions significantly increase the design complexity. In addition, there are other issues that can be solved by using very narrowband filtering before frequency conversion that may not be possible (or even

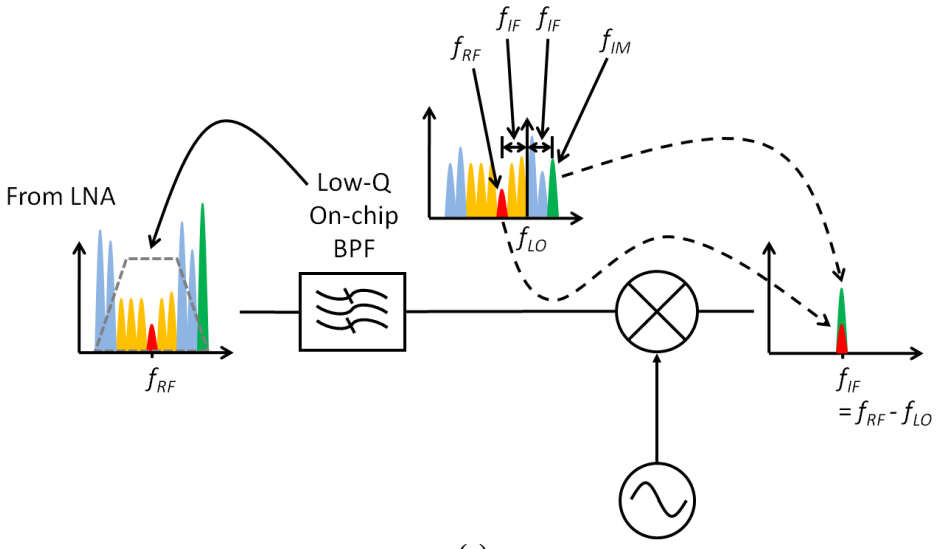

(a)

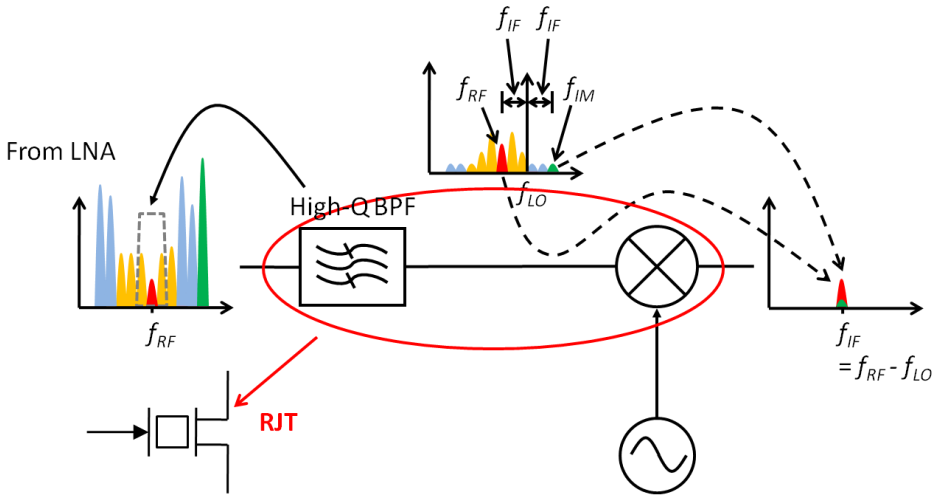

(b)

Figure 5.5. System-level illustration of the frequency conversion blocks of typical superheterodyne receiver using a (a) low-*Q*, on-chip bandpass filter and (b) high-*Q* bandpass filter for image rejection filtering before the mixer. When a low-*Q* bandpass filter with limited stopband rejection and form factor is used as in (a), a lower bound is placed on IF selection, since the image signal (green) also folds into the IF on top of the signal of interest (red). Using a high-*Q* bandpass filter as in (b) can alleviate this image filtering problem while still allowing low IF to simplify signal processing down the chain. Such high-*Q* bandpass filters are usually only available as off-chip SAW/BAW devices, but the RJT can be configured to replace both.

made worse) by using such solutions, including susceptibility to jammers and linearity problems down the signal path.

Electrostatic MEMS resonators have already demonstrated this combined narrowband filter plus frequency conversion using the inherent second-order

nonlinearity in the actuation force [121], [122]. The conversion loss, however, has been unacceptably high, in the range of 40 to 50 dB. This is because the frequency conversion relies on the generation of electrostatic force by the interaction of two relatively small signals – the RF and LO signals – resulting in a very small force at the desired IF. Typically electrostatic actuation relies on a very large bias voltage (in some cases > 100 V) to obtain reasonable efficiency. In many systems, the LO signal cannot be made this large, significantly limiting the transduction efficiency between input and output. If the RJT is used as a mixer, however, it does not need to generate a force at the IF frequency to obtain frequency conversion; this can be done by simply modulating the JFET gate, effectively amplitude modulating the output motional current signal. This will result in greatly improved conversion loss and may make narrowband filtering and frequency conversion using MEMS resonators feasible for certain RF applications. Having this capability monolithically integrated with other receiver blocks will greatly simplify the design and enhance the performance of radio front ends.

5.4 Opto-electromechanical Transduction and Optical Coupling

The devices presented in this dissertation are all based upon the seemingly simple pn-diode. While simple in structure, its many interesting properties give it a wide variety of uses as evidenced by its many variations, each optimized for a specific application (e.g., Zener diodes, tunnel diodes, light emitting diodes, laser diodes, photodiodes, etc.). One of these interesting properties is its sensitivity to light, which has garnered a large amount of interest recently due to the increasing focus on green energy and photovoltaics. Since the devices presented in this dissertation are built upon pn-diodes, it is reasonable to assume that they will exhibit a degree of photo-

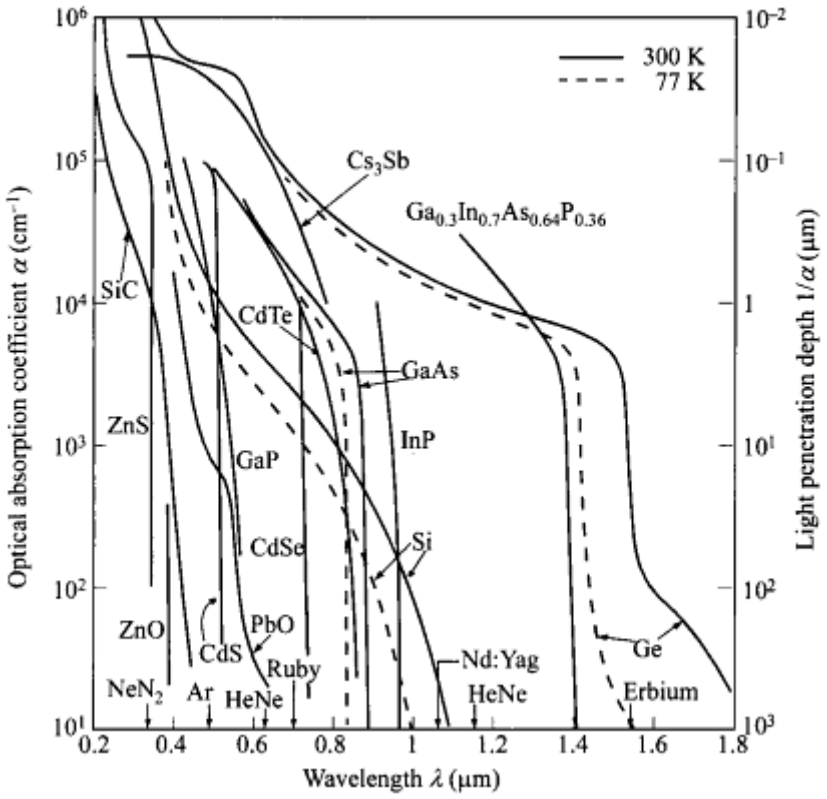

Figure 5.6. Optical absorption coefficient (left) and equivalent light penetration depth (right) of commonly used optical materials at 300 K and 77 K showing the dependence on the optical wavelength. Reproduced from [123].

sensitivity as well. In particular, it may be possible to use optics to actuate or detect motion in the pn-diode internally transduced resonators or the RJT.

When light is incident upon a bulk semiconducting material, photons may collide with the electrons in the valence band of the semiconductor and excite them into the conduction band. This occurs if the photon energy $E_{ph} = h\nu$ is greater than the semiconductor bandgap. For such photons, the power absorbed per unit area as the light travels through the semiconducting material is dictated by the absorption coefficient α. This coefficient is in general very dependent on the wavelength of light, as seen in Figure 5.6 [123]. The photon flux as the light travels through the semiconducting material is then given by

$$\Phi(x) = \Phi_o e^{-\alpha x}. \tag{105}$$

In (105), Φ_o is the incident photon flux at the surface of the semiconductor, which can be found by dividing the incident power by the area and the photon energy. This expression indicates that photons are absorbed at an exponential rate as the light travels through the material, resulting in the generation of free carriers. A photoconductor exploits this simple principle to convert optical energy into a change in resistivity, making this device in essence an optically-controlled resistor. When a voltage is applied across the semiconductor, the current flowing through the material is then proportional to the incident optical power. One issue with the photoconductor is that the bandwidth of operation is limited by the minority carrier lifetime, which can be relatively large for silicon (1 ms to 1 μS), thus precluding its use at frequencies about 1 MHz.

For higher frequencies, a junction may also be used for opto-electric transduction. When light is incident on a reverse biased pn-diode, photons that get absorbed in the depletion region will generate electrons and holes, which each get swept away to the anode and cathode, respectively, due to the large electric field inside the depletion region. This results in a photo-generated current through the junction, which is the main principle behind photodiodes and photovoltaic cells. The speed in this case is limited by the transit time across the depletion region and a long minority carrier lifetime is actually desirable so that the carriers do not recombine while in the depletion region. The build-up of photo-generated charge carriers for an open junction will result in a voltage across the junction. If this photodiode is the input actuation junction of the pn-diode transduced resonator or RJT and the optical modulation frequency corresponds to its mechanical resonant frequency, then this induced voltage signal will excite resonant motion in the resonator. In this scenario, optical energy is

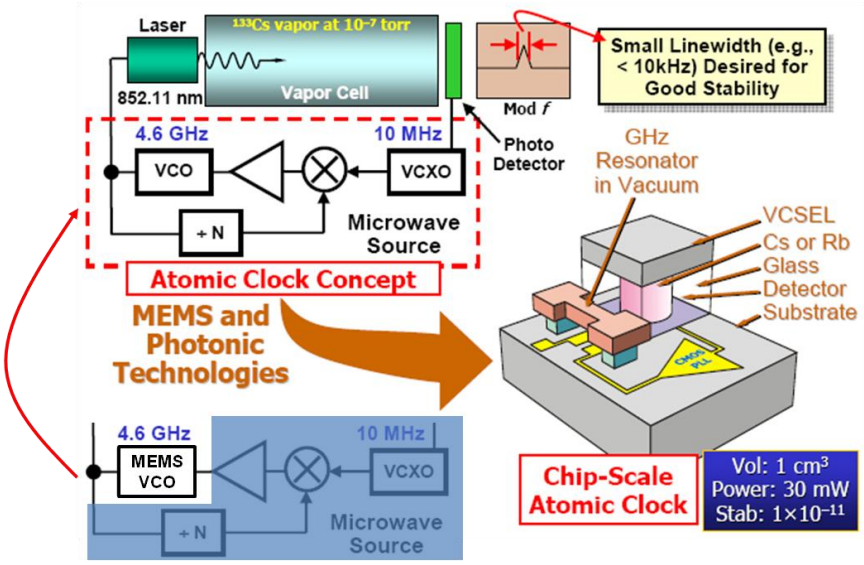

Figure 5.7. System-level schematic of a Chip-Scale Atomic Clock using a Cesium vapor cell. Reproduced from [124]. A low phase noise, MEMS-based monolithic oscillator may replace the large crystal oscillator and surrounding PLL circuitry to significantly reduce power consumption.

converted to an electrical voltage, which by the process described in Chapter 2 will result in mechanical motion, hence the term opto-electromechanical transduction.

The more complex signal path taken will undoubtedly decrease the efficiency of transduction. But with recent developments in integrated photonics, the capability to couple between all three domains – electrical, mechanical, and optical – may prove useful as systems become more integrated and complex. The chip-scale atomic clock (CSAC), which has been investigated in great detail here at Cornell, is an example of an application that may benefit from this coupling. A cartoon showing the system architecture of the CSAC is shown in Figure 5.7 [124]. The CSAC uses the energy difference between the hyperfine states of alkali metal atoms in a vapor cell to determine the transmission of an incident laser through this cell. The transmitted optical power is detected by a photodiode and fed back to the microwave frequency synthesizer that modulates the laser. The feedback loop aims to lock to the maximum transmission through the vapor cell, which occurs when the laser modulation frequency exactly matches the hyperfine frequency. Currently, the only frequency synthesizers that can achieve the required frequency stability to lock at the hyperfine

frequencies in the multi-GHz range (approximately 6.8 GHz for Rubidium and 9.2 GHz for Cesium) are electrical LC VCOs (for high output frequency) phase-locked to a low-frequency off-chip crystal reference oscillator (for low phase noise far from the carrier frequency) through a PLL. In addition to increasing the solution area, the crystal oscillator output is limited to the range of 10 MHz, necessitating a very large divide-down ratio, which is the current bottleneck to lowering the total power consumption. In [124], using a tunable, low-phase noise MEMS reference LO to directly synthesize a reference signal at the multi-GHz hyperfine frequency is suggested to eliminate the frequency divider circuitry and substantially reduce the power consumption. MEMS-based oscillators are especially well-suited for CSAC due to the small tuning range requirements compared to other systems, e.g. radio transceivers. As shown in the previous subsection, this is possible using pn-diode transduced resonators or RJTs as the high-*Q* resonant element in an oscillator loop with the frequency tuning voltage applied to the gate.

While this method of directly replacing components would itself result in better performance, the possibility of optical transduction may enable new techniques that make the overall system even more efficient. As one specific example, it may be possible to greatly simplify the LO control loop (Figure 5.8(a)) using such methods. In order to move the signal away from 1/f noise present near baseband and to provide direction information for the LO control voltage to lock onto the transmission peak from the vapor cell, a small frequency modulation signal switched at 3 kHz is added to the LO control voltage, resulting in amplitude modulation of the laser power at 3 kHz. In order to sense this modulation, the output current of the photodiode is converted to a voltage signal using a transimpedance amplifier and is filtered with a bandpass filter centered at 3 kHz. This signal is then fed into a lock-in amplifier to demodulate this 3 kHz signal and output the DC level of the control voltage, which is dependent on the

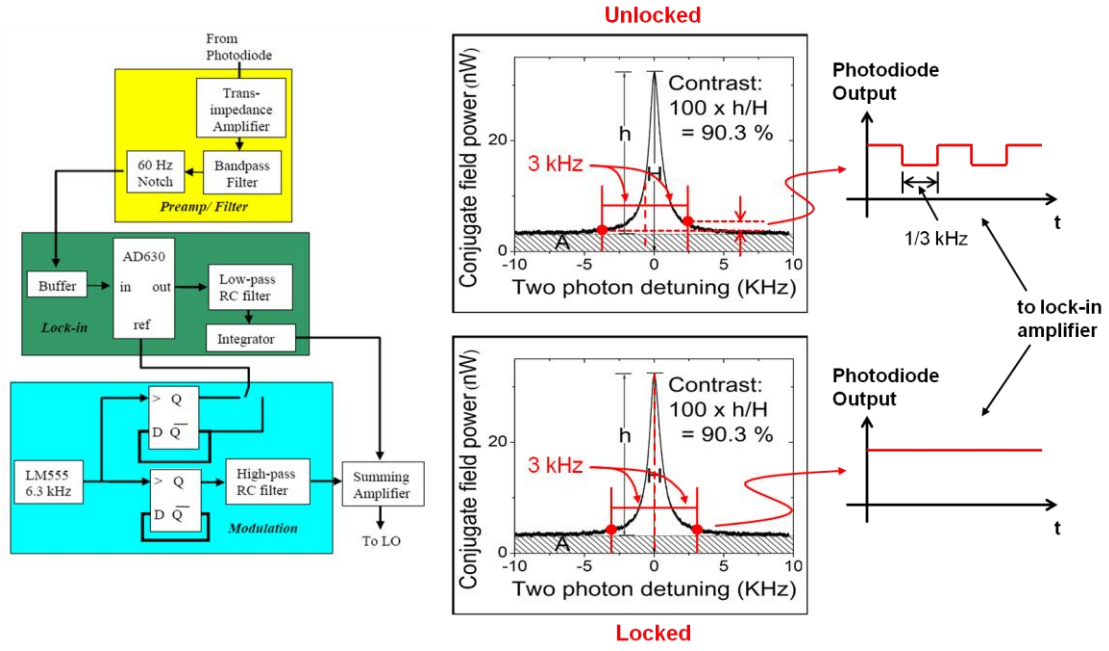

(a) (b)

Figure 5.8. (a) Block diagram of the LO control loop for a typical CSAC. Reproduced from [125]. (b) Plots showing the optical transfer function through the atomic vapor cell as a function of detuning from the hyperfine frequency [126]. Top plot shows the scenario where the output of the lock-in amplifier is such that the LO is not tuned to the hyperfine resonant peak and there is a difference between optical transmission through the vapor cell at the 3 kHz modulation frequency of the LO control voltage. Bottom plot shows the case where the LO is tuned to the resonant peak and there is no modulation of the photodiode output and the output of the integrator remains constant.

amplitude of the sidebands. This is combined with the original 3 kHz modulation and fed into the VCO, closing the LO control loop. When the LO frequency is perfectly aligned to the transmission peak through the vapor cell (locked condition), the laser power incident on the photodiode is the same for both phases of the modulation clock as illustrated in Figure 5.8(b), meaning there is no signal at 3 kHz from the photodiode, and the output of the integrator stays constant. On the other hand, when the LO control loop is not locked, the incident laser power during each phase of the modulation clock will be different, resulting in a signal at 3 kHz at the output of the photodetector and a near DC voltage at the output of the lowpass filter. This voltage is fed into the integrator, which adjusts the VCO control voltage to drive the loop towards lock.

Surprisingly, it may be possible to use a single RJT in a closed-loop oscillator configuration to fulfill all the functions of the VCO, photodiode, and preamp/filter, as illustrated in Figure 5.9. Frequency tuning of the RJT-based oscillator can be achieved by adjusting the gate or drain biases, as discussed in the previous subsection, serving as a means of adjusting the frequency as a function of the modulation sideband amplitude. These modulation sidebands may be generated in the first place by exploiting the photosensitive conductivity of semiconductors discussed earlier in this subsection: shining the transmitted light through the vapor cell onto the channel region will cause modulation of the drain current via carrier generation and thus oscillator amplitude, resulting in AM sidebands around the oscillator frequency. The sidebands may also be generated by shining the light on the actuation junction, resulting in a photosensitive actuation voltage which was also discussed previously. Simply adding an envelope detector to demodulate the amplitude modulated oscillator output should result in a signal similar to that at the input of the lock-in amplifier in Figure 5.8(a). Note that a structure similar to the 'modulation' block in Figure 5.8(a) is still necessary to create the initial modulation signal.

As illustrated by this discussion, the sensitivity of the RJT to optical signals can provide benefits beyond simple direct replacement of components (in this case, the LC VCO of the conventional CSAC design for the RJT-based oscillator), including greatly reducing the number of components needed and the solution area. This is only one specific example of how the photosensitivity of pn-junctions and semiconducting materials may be utilized in the RJT to enable coupling between optical, electrical, and mechanical domains. This interdomain coupling can be used to enhance the performance of existing devices and systems and even enable new ones in the future.

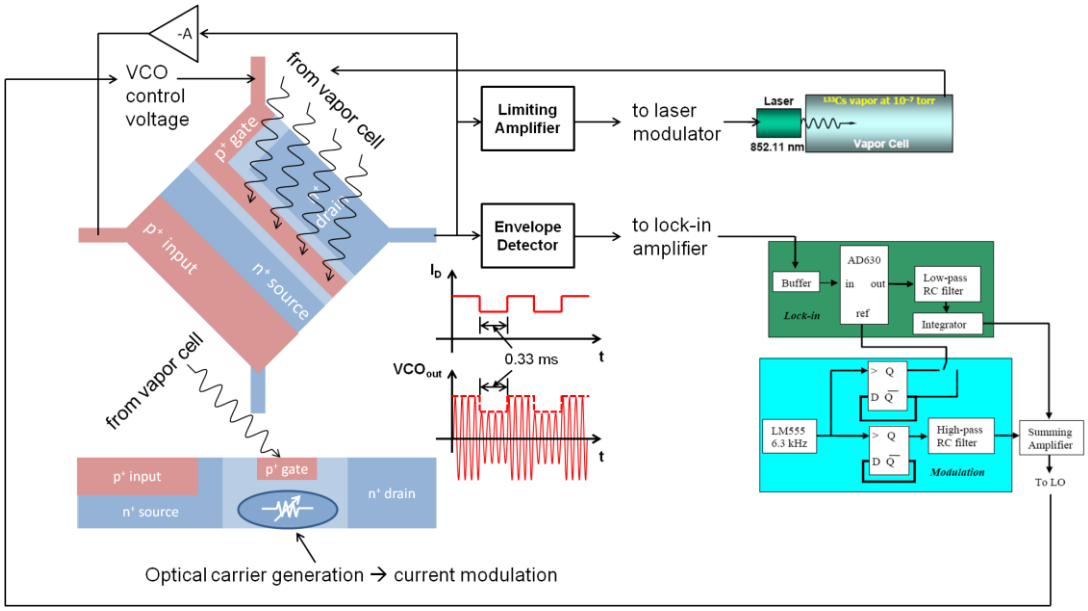

Figure 5.9. An alternate LO control loop using an RJT-based voltage controlled oscillator and making use of its optical sensitivity to perform the functions of the preamplifier/filter sub-block in Figure 5.8(a) with a single device.

5.5 Conclusions

Revisiting the original goals of this dissertation as presented in the introduction, we have presented in this work a novel UHF micromechanical resonator utilizing pn-diode internal transduction, which retains the high mechanical Q of single-crystal silicon and whose simple fabrication allows for easy integration into an SOI RF CMOS technology without any modifications to the existing front end process. Based on this concept, this dissertation demonstrates a resonant junction transistor (RJT) device that intimately couples the mechanical and electrical domains and reduces the feedthrough signal, leading to improved electromechanical transduction. Specifically, this dissertation demonstrates the highest f-Q product reported in silicon at room temperature to date of 6.67×10^{13} Hz at a frequency of 3.7 GHz. Another specific contribution of this dissertation includes the demonstration of the highest g_m/I_D ratio in

resonant transistors reported to date with a value of 1.2, indicating the feasibility of such devices in practical systems. This dissertation also investigates in detail the sources of acoustic loss present in silicon and develops a model based on these factors to closely fit experimental data obtained for these high *Q* resonators. In this regard, this dissertation reports on the first ever experimental demonstration via temperature measurements of Landau-Rumer scattering as the dominant phonon-phonon scattering process limiting the *Q* of silicon micromechanical resonators operating above 1 GHz. Also, this dissertation provides initial experimental evidence that at low temperatures, electron-phonon scattering may not be negligible in MEMS resonators using highly doped single-crystal silicon. It is the hope of the author that the work presented here may contribute to the understanding of RF MEMS resonators and their possibilities in the applications suggested in the future work section and other applications that have yet to be discovered.

APPENDIX

A. Effects of Acoustic Mismatch: Additional Details

In Chapter 2, the effects of acoustic mismatch on the optimal dielectric location and motional impedance of internal dielectrically transduced resonators was discussed and it was found that the Young's modulus of the dielectric film significantly impacts the resonator properties. Some additional details of the full derivation that were not included in the original analysis will be introduced here.

Again, the geometry under consideration is that shown in Figure 2.7. The analysis proceeds as before, following (19)-(41). The full expressions for the amplitude coefficients A_n and B_n in (39)-(41) are shown in (A1)-(A8).

$$A_1 = \frac{2\varepsilon_0\varepsilon_r V_{DC}\sin\left(k_{diel}\frac{g}{2}\right)}{g^2}\frac{1}{E_{si}k_{si}}\frac{N_1}{D},\quad B_1 = 0 \tag{A1}$$

$$N_1 = \sqrt{\frac{E_{diel}\rho_{diel}}{E_{si}\rho_{si}}}\sin\left(k_{diel}\frac{g}{2}\right)\cos\left(k_{si}\left(\frac{g}{2}-\frac{L}{2}+d\right)\right) - \cos\left(k_{diel}\frac{g}{2}\right)\sin\left(k_{si}\left(\frac{g}{2}-\frac{L}{2}+d\right)\right) \tag{A2}$$

$$A_2 = \frac{\varepsilon_0\varepsilon_r V_{DC}}{g^2}\frac{1}{E_{si}k_{si}}\frac{N_{A2}}{D},\quad B_2 = \frac{\varepsilon_0\varepsilon_r V_{DC}}{g^2}\frac{1}{E_{si}k_{si}}\frac{N_{B2}}{D} \tag{A3}$$

$$N_{A2} = \cos\left(k_{diel}\frac{g}{2}\right)\cos\left(k_{si}\left(g-\frac{L}{2}\right)\right) - 2\sqrt{\frac{E_{diel}\rho_{diel}}{E_{si}\rho_{si}}}\sin\left(k_{diel}\frac{g}{2}\right)\sin\left(k_{si}\left(d-\frac{g}{2}\right)\right)\cos\left(k_{si}\left(\frac{g}{2}-\frac{L}{2}+d\right)\right) \tag{A4}$$

$$N_{B2} = \sin\left(k_{diel}\frac{g}{2}\right)\cos\left(k_{si}\left(\frac{L}{2}-2d\right)\right) \tag{A5}$$

$$A_3 = 0,\quad B_3 = -\frac{2\varepsilon_0\varepsilon_r V_{DC}\sin\left(k_{diel}\frac{g}{2}\right)}{g^2}\frac{1}{E_{si}k_{si}}\frac{N_3}{D} \tag{A6}$$

$$N_3 = \sqrt{\frac{E_{diel}\rho_{diel}}{E_{si}\rho_{si}}}\sin\left(k_{diel}\frac{g}{2}\right)\sin\left(k_{si}\left(d-\frac{g}{2}\right)\right)-\cos\left(k_{diel}\frac{g}{2}\right)\cos\left(k_{si}\left(d-\frac{g}{2}\right)\right) \tag{A7}$$

$$\begin{aligned} D = {} & \sin(k_{diel}g) \\ & \left[\frac{E_{diel}\rho_{diel}}{E_{si}\rho_{si}}\cos\left(k_{si}\left(\frac{g}{2}-\frac{L}{2}+d\right)\right)\sin\left(k_{si}\left(d-\frac{g}{2}\right)\right)-\sin\left(k_{si}\left(\frac{g}{2}-\frac{L}{2}+d\right)\right)\cos\left(k_{si}\left(d-\frac{g}{2}\right)\right)\right] \\ & -\sqrt{\frac{E_{diel}\rho_{diel}}{E_{si}\rho_{si}}}\cos(k_{diel}g)\cos\left(k_{si}\left(\frac{L}{2}-g\right)\right) \end{aligned} \tag{A8}$$

Here, D is the factor in the denominator common for (A1), (A3), and (A6), and the resonant frequencies can be found by solving for ω when $D = 0$. This yields the results shown in Figures 2.8 to 2.11. In Chapter 2, correction factors for the optimal junction location and the motional impedance were introduced. In addition to these modifications, the resonant frequency also shifts. The correction to the resonant frequency due to acoustic mismatch between the dielectric film and the resonant body is given by

$$\frac{f_{o,new}}{f_o} = \frac{1-\frac{2g}{L}\frac{E_{si}}{E_{diel}}\cos^2\left(\frac{n\pi d}{L}\right)}{1-\frac{2g}{L}\cos^2\left(\frac{n\pi d}{L}\right)}\frac{1-\frac{2g}{L}\sin^2\left(\frac{n\pi d}{L}\right)}{1-\frac{2g}{L}\frac{\rho_{diel}}{\rho_{si}}\sin^2\left(\frac{n\pi d}{L}\right)} \approx \frac{1-\frac{2g}{L}\frac{E_{si}}{E_{diel}}}{1-\frac{2g}{L}}. \tag{A9}$$

The last approximation made in (A9) is true when the transducer is optimally placed such that the $\sin^2(n\pi d/L)$ term is nearly equal to zero. This frequency resulting from application of this correction factor has been compared with the exact frequency determined by numerical simulations using MATLAB. These results are shown in Figure A.1. The same comparison is performed for the motional impedance and its corresponding correction factor and the results are shown in Figure A.2. Figure A.3(a) and (b) plots the corresponding error for the resonant frequency and motional impedance found using the correction factor and numerical simulations.

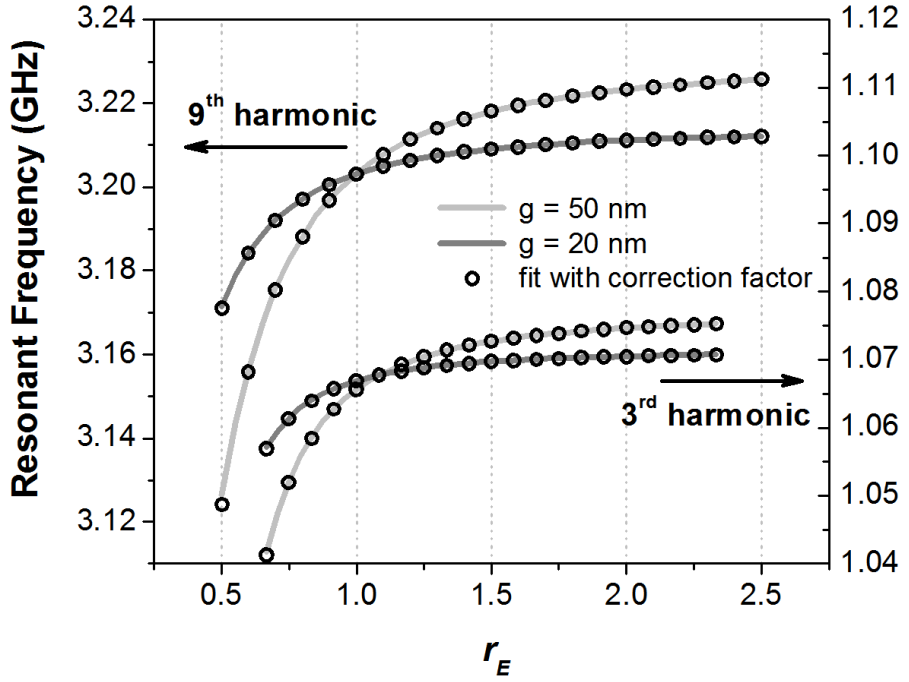

Figure A.1. Comparison of f_o for both 3rd and 9th harmonics (g = 20 and 50 nm) determined using correction factor given by (A9) and f_o found using numerical simulations in MATLAB.

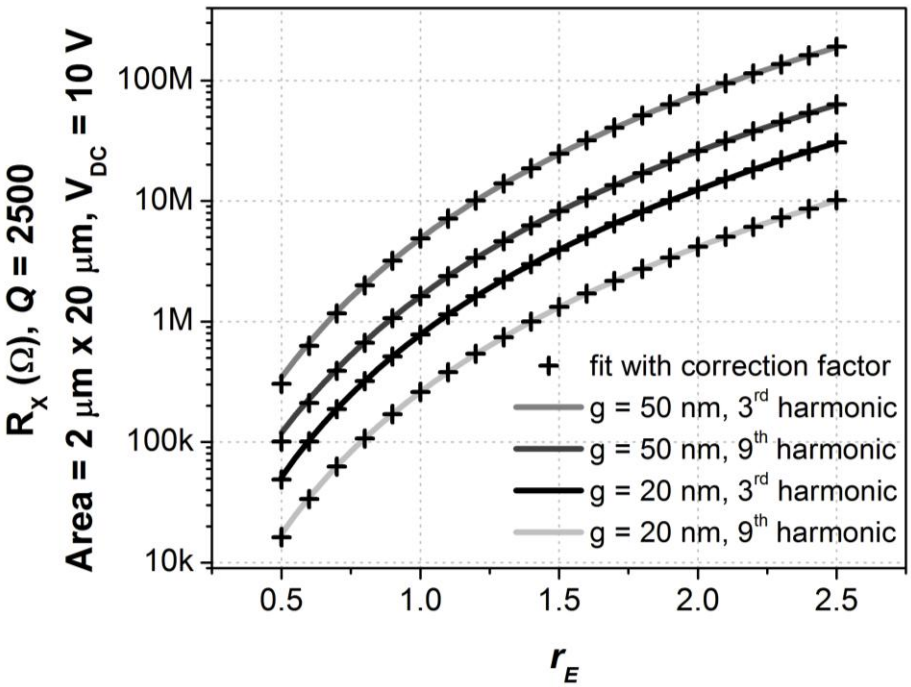

Figure A.2. Comparison of R_X for both 3rd and 9th harmonics (g = 20 and 50 nm) determined using correction factor given by (47) and R_X found using numerical simulations in MATLAB.

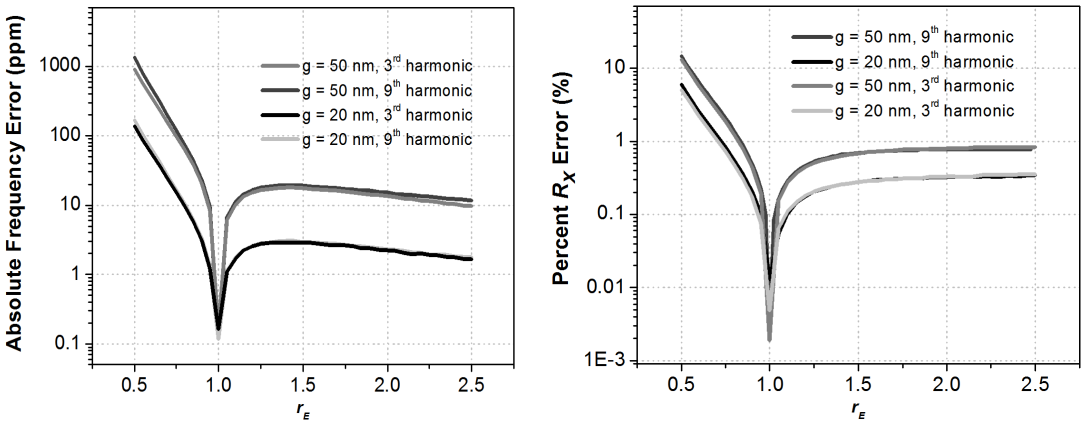

(b)

(b)

Figure A.3. (a) Frequency error (ppm) between simulated resonant frequency and that estimated by (A9). (d) Percent R_X error between simulated motional impedance and that estimated by (47).

B. pn-Diode Internally Transduced Resonator Detailed Fabrication Process

Provided below is the comprehensive list of process steps required to fabricate the pn-diode internally transduced resonator. This process is designed for fabrication of these devices in the CNF, but may be transferred to other facilities and modified as necessary.

Table B.1. Detailed fabrication process flow for the pn-diode internally transduced resonator

Mask Layer	Process Type	Mat/Mask	Tool	Process
-	Start	SOI wafer	Ultrasil	2.5 µm 0.006 Ω-cm device layer, 1.3 µm BOX, 500 µm handle
-	Clean	-	MOS	RCA clean
ALGN	Spin	P20 /SPR220-3.0	Resist Spinner	3000 rpm, 1000 rpm/s, 30 sec.
ALGN	Bake	SPR220-3.0	Hotplate	Prebake: 115°C, 90 sec.
ALGN	Expose	ALGN	AS200	Exposure time for 500 µm handle: 0.38 sec.
ALGN	Bake	SPR220-3.0	Hotplate	Post-exposure bake: 115°C, 90 sec.
ALGN	Develop	726MIF	Hamatech	Recipe 2: 726MIF DP 120 sec.
ALGN	Descum	SPR220-3.0	Oxford 81	O_2: 50 sccm, Pressure: 30 mTorr, RF: 100 W, 30 sec.
ALGN	Etch	Si/ SPR220-3.0	Oxford 100	Recipe: Si CF4 Test, 12 min.
ALGN	Strip	SPR220-3.0	Aura 1000	Recipe 2 (×2), break in between
ALGN	Clean	SPR220-3.0	Hamatech	Hot Piranha Clean
PIMP	Deposit	SiO_2	GSI	Recipe: L DEP RATE OX, 5 min, total 580-600 nm
PIMP	-	SiO_2	Filmetrics	Measure oxide hard mask thickness
PIMP	Spin	P20 /SPR220-3.0	Resist Spinner	3000 rpm, 1000 rpm/s, 30 sec., approx. 2.2 µm resist
PIMP	Bake	SPR220-3.0	Hotplate	Prebake: 115°C, 90 sec.
PIMP	Expose	PIMP	AS200	Exposure time for 500 µm handle: 0.375 sec.
PIMP	Bake	SPR220-3.0	Hotplate	Post-exposure bake: 115°C, 90 sec.
PIMP	Develop	726MIF	Hamatech	Recipe 2: 726MIF DP 120 sec.
PIMP	Descum	SPR220-3.0	Oxford 81	O_2: 50 sccm, Pressure: 30

				mTorr, RF: 100 W, 9 min.
PIMP	Etch	SiO_2/ SPR220-3.0	Oxford 100	Recipe: CHF_3/O_2 Oxide Etch, 4 min., leave approx. 100 nm SiO_2
PIMP	-	SiO_2	Filmetrics	Measure oxide hard mask thickness
PIMP	Etch	SiO_2/ SPR220-3.0	Chemistry hood	BOE 6:1, 1 min. (exact time depends on SiO_2 left from previous etch step)
PIMP	Strip	SPR220-3.0	Aura 1000	Recipe 2 (×2)
PIMP	Clean	SPR220-3.0	Hamatech	Hot Piranha Clean
PIMP	Implant	Boron/SiO_2	Eaton	Implant 1: 90 keV, 4e15 cm^{-2} dose Implant 2: 45 keV, 3e15 cm^{-2} dose Implant 3: 25 keV, 3e15 cm^{-2} dose Implant 4: 10 keV, 3e15 cm^{-2} dose Dependent on device layer thickness
PIMP	Clean	-	MOS	RCA clean
PIMP	Anneal	-	AG8108	300°C load, 25 sec. ramp to 1100°C, 15 sec. soak, 300°C unload
PIMP	Clean	-	MOS	RCA clean with 30 sec. 20:1 HF 49%:DI H_2O dip
PIMP	Diffusion	Boron	B Diff Furnace	750°C load, 20 min. ramp to 975°C, 20 min. soak, 50 min. ramp to 800°C
PIMP	Strip	BSG	MOS	20:1 HF 49%:DI H_2O, 5 min.
PIMP	Growth	SiO_2	MOS Oxide Furnace	750°C load, 750°C wet oxidation for 20 min. 750°C unload
PIMP	Strip	SiO_2	Chemistry hood	BOE 6:1, 5.5 min.
PIMP	Clean	-	Hamatech	Hot Piranha Clean
RES	Spin	P20/ nLOF2020	Resist Spinner	3000 rpm, 1000 rpm/s, 30 sec.
RES	Bake	nLOF2020	Hotplate	Prebake: 115°C, 90 sec.
RES	Expose	RES	AS200	Exposure time for 500 µm handle: 0.125 sec.
RES	Bake	nLOF2020	Hotplate	Post-exposure bake: 115°C, 90 sec.
RES	Develop	726MIF	Hamatech	Recipe 2: 726MIF DP 120 sec.
RES	Descum	nLOF2020	Oxford 81	O_2: 50 sccm, Pressure: 30 mTorr, RF: 100 W, 1 min.

RES	Deposit	Cr	CHA	Base pressure: 2 µTorr, 2 Cr rods, 5 Angstrom/sec.
RES	Liftoff	Cr	Photolith hood	Acetone bath 2 hr. soak, 30 min. sonicate in new acetone bath, rinse in IPA bath, DI rinse, N_2 blow dry
RES	Etch	Si/Cr	Oxford 100	Recipe: Si CF4 Test, 12 min.
RES	Strip	Cr	Chemistry hood	CR-14, 10 min.
RES	Clean	-	Hamatech	Hot Piranha Clean
MET	Etch	SiO_2	Chemistry hood	BOE 30:1, 1 min.
MET	Deposit	Cr, Al	CVC	Base pressure: 1.3 µTorr, 5 min. ion mill, 5 min. Cr presputter, 5 min deposition, 5 min. Al presputter, 10 min. Al deposition
MET	Spin	P20/ SPR220-3.0	Resist Spinner	3000 rpm, 1000 rpm/s, 30 sec.
MET	Bake	SPR220-3.0	Hotplate	Prebake: 115°C, 90 sec.
MET	Expose	MET	AS200	Exposure time for 500 µm handle: 0.38 sec.
MET	Bake	SPR220-3.0	Hotplate	Post-exposure bake: 115°C, 90 sec.
MET	Develop	726MIF	Hamatech	Recipe 2: 726MIF DP 120 sec.
MET	Descum	SPR220-3.0	Oxford 81	O_2: 50 sccm, Pressure: 30 mTorr, RF: 100 W, 1 min.
MET	Etch	Al	Chemistry hood	Al Etch A, 2 min. with agitation
MET	Etch	Cr	Chemistry hood	CR-14, 2 min. with agitation
MET	Rinse	DI H_2O	Chemistry hood	DI H_2O rinse, spin rinse dry
REL	Spin	P20/ SPR220-3.0	Resist Spinner	3000 rpm, 1000 rpm/s, 30 sec.
REL	Bake	SPR220-3.0	Hotplate	Prebake: 115°C, 90 sec.
REL	Expose	RES	AS200	Exposure time for 500 µm handle: 0.38 sec.
REL	Bake	SPR220-3.0	Hotplate	Post-exposure bake: 115°C, 90 sec.
REL	Develop	726MIF	Hamatech	Recipe 2: 726MIF DP 120 sec.
REL	Descum	SPR220-3.0	Oxford 81	O_2: 50 sccm, Pressure: 30 mTorr, RF: 100 W, 1 min.
REL	Cleave	-	Scribe	Into quarter pieces
REL	Etch	SiO_2	Chemistry hood	BOE 6:1, 80 min.

REL	Rinse	DI H_2O	Chemistry hood	DI H_2O, 4 baths
REL	Strip	SPR220-3.0	Chemistry hood	Acetone, 2 baths, 5 min. each
REL	Rinse	DI H_2O + Methanol	Chemistry hood	Successive soaks: 50%/50%, 25%/75% DI H_2O/methanol, then 100% methanol 2 baths
REL	CPD	CO_2	Tousimis	Cool 0.5, Fill 1.0, Purge-Vent 0.25, Bleed 0.25, 25 min. purge time

C. Resonant Junction Transistor Detailed Fabrication Process

Provided below is the comprehensive list of process steps required to fabricate the resonant junction transistor. This process is designed for fabrication of these devices in the CNF, but may be transferred to other facilities and modified as necessary.

Table C.1. Detailed fabrication process flow for the resonant junction transistor

Mask Layer	Process Type	Mat/Mask	Tool	Process
-	Start	SOI wafer	Ultrasil	2.5 µm undoped device layer, 2 µm BOX, 500 µm handle
-	Clean	-	MOS	RCA clean
-	Implant	-	Eaton	P implant, 190 keV, 1e12 cm^{-2} dose, 0° tilt
-	Clean	-	MOS	RCA clean with 30 sec. 20:1 HF 49% dip
-	Anneal	-	MOS clean anneal	800°C load, 20 min ramp to 1100°C, 5 hr. soak, 45 min. ramp to 800°C, N_2 ambient
ALGN	Spin	P20 /SPR220-3.0	Resist Spinner	3000 rpm, 1000 rpm/s, 30 sec.
ALGN	Bake	SPR220-3.0	Hotplate	Prebake: 115°C, 90 sec.
ALGN	Expose	ALGN	AS200	Exposure time for 500 µm handle: 0.38 sec.
ALGN	Bake	SPR220-3.0	Hotplate	Post-exposure bake: 115°C, 90 sec.
ALGN	Develop	726MIF	Hamatech	Recipe 2: 726MIF DP 120 sec.
ALGN	Descum	SPR220-3.0	Oxford 81	O_2: 50 sccm, Pressure: 30 mTorr, RF: 100 W, 30 sec.
ALGN	Etch	Si/ SPR220-3.0	Oxford 100	Recipe: Si CF4 Test, 12 min.
ALGN	Strip	SPR220-3.0	Aura 1000	Recipe 2 (×2), break in between
ALGN	Clean	SPR220-3.0	Hamatech	Hot Piranha Clean
NDIF	Deposit	SiO_2	GSI	Recipe: L DEP RATE OX, 4.4 min, total 490-500 nm
NDIF	-	SiO_2	Filmetrics	Measure oxide hard mask thickness
NDIF	Spin	P20 /SPR220-3.0	Resist Spinner	3000 rpm, 1000 rpm/s, 30 sec.
NDIF	Bake	SPR220-3.0	Hotplate	Prebake: 115°C, 90 sec.
NDIF	Expose	NDIF	AS200	Exposure time for 500 µm

				handle: 0.375 sec.
NDIF	Bake	SPR220-3.0	Hotplate	Post-exposure bake: 115°C, 90 sec.
NDIF	Develop	726MIF	Hamatech	Recipe 2: 726MIF DP 120 sec.
NDIF	Descum	SPR220-3.0	Oxford 81	O_2: 50 sccm, Pressure: 30 mTorr, RF: 100 W, 30 sec.
NDIF	Etch	SiO_2/ SPR220-3.0	Oxford 100	Recipe: CHF_3/O_2 Oxide Etch, 3.5 min., leave approx. 100 nm SiO_2
NDIF	-	SiO_2	Filmetrics	Measure oxide hard mask thickness
NDIF	Etch	SiO_2/ SPR220-3.0	Chemistry hood	BOE 6:1, 1 min. (exact time depends on SiO_2 left from previous etch step)
NDIF	Strip	SPR220-3.0	Aura 1000	Recipe 2 (×2), break in between
NDIF	Clean	SPR220-3.0	Hamatech	Hot Piranha Clean
NDIF	Clean	-	MOS	RCA clean with 30 sec. 20:1 HF 49%:DI H_2O dip
NDIF	Diffusion	Phosphorus	P Diff Furnace	750°C load, 25 min. ramp to 1000°C, 25 min. soak, 50 min. ramp to 800°C
NDIF	Strip	PSG	MOS	20:1 HF 49%:DI H_2O, 5 min.
NDIF	Diffusion	Phosphorus	MOS clean anneal	800°C load, 30 min. ramp to 1100°C, 75 min. soak, 60 min. ramp to 900°C, N_2 ambient
NDIF	Strip	SiO_2	Chemistry hood	BOE 6:1, 5 min.
PIMP	Deposit	SiO_2	GSI	Recipe: L DEP RATE OX, 5 min, total 580-600 nm
PIMP	-	SiO_2	Filmetrics	Measure oxide hard mask thickness
PIMP	Spin	P20 /SPR220-3.0	Resist Spinner	3000 rpm, 1000 rpm/s, 30 sec., approx. 2.2 µm resist
PIMP	Bake	SPR220-3.0	Hotplate	Prebake: 115°C, 90 sec.
PIMP	Expose	PIMP	AS200	Exposure time for 500 µm handle: 0.375 sec.
PIMP	Bake	SPR220-3.0	Hotplate	Post-exposure bake: 115°C, 90 sec.
PIMP	Develop	726MIF	Hamatech	Recipe 2: 726MIF DP 120 sec.
PIMP	Descum	SPR220-3.0	Oxford 81	O_2: 50 sccm, Pressure: 30 mTorr, RF: 100 W, 9 min.
PIMP	Etch	SiO_2/ SPR220-3.0	Oxford 100	Recipe: CHF_3/O_2 Oxide Etch, 4 min., leave approx. 100 nm SiO_2
PIMP	-	SiO_2	Filmetrics	Measure oxide hard mask thickness
PIMP	Etch	SiO_2/	Chemistry	BOE 6:1, 1 min. (exact time

		SPR220-3.0	hood	depends on SiO_2 left from previous etch step)
PIMP	Strip	SPR220-3.0	Aura 1000	Recipe 2 (×2)
PIMP	Clean	SPR220-3.0	Hamatech	Hot Piranha Clean
PIMP	Implant	Boron/SiO_2	Eaton	Implant 1: 90 keV, 4e15 cm^{-2} dose Implant 2: 45 keV, 3e15 cm^{-2} dose Implant 3: 25 keV, 3e15 cm^{-2} dose Implant 4: 10 keV, 3e15 cm^{-2} dose Dependent on device layer thickness
PIMP	Clean	-	MOS	RCA clean
PIMP	Anneal	-	AG8108	300°C load, 25 sec. ramp to 1100°C, 15 sec. soak, 300°C unload
PIMP	Clean	-	MOS	RCA clean with 30 sec. 20:1 HF 49%:DI H_2O dip
PIMP	Diffusion	Boron	B Diff Furnace	750°C load, 20 min. ramp to 975°C, 20 min. soak, 50 min. ramp to 800°C
PIMP	Strip	BSG	MOS	20:1 HF 49%:DI H_2O, 5 min.
PIMP	Growth	SiO_2	MOS Oxide Furnace	750°C load, 750°C wet oxidation for 20 min. 750°C unload
PIMP	Strip	SiO_2	Chemistry hood	BOE 6:1, 5.5 min.
PIMP	Clean	-	Hamatech	Hot Piranha Clean
MET	Spin	P20/ nLOF2020	Resist Spinner	3000 rpm, 1000 rpm/s, 30 sec.
MET	Bake	nLOF2020	Hotplate	Prebake: 115°C, 90 sec.
MET	Expose	MET	AS200	Exposure time for 500 µm handle: 0.125 sec.
MET	Bake	nLOF2020	Hotplate	Post-exposure bake: 115°C, 90 sec.
MET	Develop	726MIF	Hamatech	Recipe 2: 726MIF DP 120 sec.
MET	Descum	nLOF2020	Oxford 81	O_2: 50 sccm, Pressure: 30 mTorr, RF: 100 W, 1 min.
MET	Etch	SiO_2	Chemistry hood	BOE 30:1, 1 min.
MET	Deposit	Cr, Al	CVC	Base pressure: 1.3 µTorr, 5 min. ion mill, 5 min. Cr presputter, 5 min deposition, 5 min. Al presputter, 10 min. Al deposition

MET	Liftoff	Cr, Al	Photolith hood	1165 bath overnight, 30 min. sonicate in new 1165 bath, rinse in IPA bath, DI rinse, N_2 blow dry
RES	Spin	P20/ nLOF2020	Resist Spinner	3000 rpm, 1000 rpm/s, 30 sec.
RES	Bake	nLOF2020	Hotplate	Prebake: 115°C, 90 sec.
RES	Expose	RES	AS200	Exposure time for 500 µm handle: 0.125 sec.
RES	Bake	nLOF2020	Hotplate	Post-exposure bake: 115°C, 90 sec.
RES	Develop	726MIF	Hamatech	Recipe 2: 726MIF DP 120 sec.
RES	Descum	nLOF2020	Oxford 81	O_2: 50 sccm, Pressure: 30 mTorr, RF: 100 W, 1 min.
RES	Deposit	Cr	CHA	Base pressure: 2 µTorr, 2 Cr rods, 5 Angstrom/sec.
RES	Liftoff	Cr	Photolith hood	Acetone bath 2 hr. soak, 30 min. sonicate in new acetone bath, rinse in IPA bath, DI rinse, N_2 blow dry
RES	Etch	Si/Cr	Oxford 100	Recipe: Si CF4 Test, 12 min.
RES	Strip	Cr	Chemistry hood	Cr etch, 10 min.
REL	Spin	P20/ SPR220-3.0	Resist Spinner	3000 rpm, 1000 rpm/s, 30 sec.
REL	Bake	SPR220-3.0	Hotplate	Prebake: 115°C, 90 sec.
REL	Expose	RES	AS200	Exposure time for 500 µm handle: 0.38 sec.
REL	Bake	SPR220-3.0	Hotplate	Post-exposure bake: 115°C, 90 sec.
REL	Develop	726MIF	Hamatech	Recipe 2: 726MIF DP 120 sec.
REL	Descum	SPR220-3.0	Oxford 81	O_2: 50 sccm, Pressure: 30 mTorr, RF: 100 W, 1 min.
REL	Cleave	-	Scribe	Into quarter pieces
REL	Etch	SiO_2	Chemistry hood	BOE 6:1, 80 min.
REL	Rinse	DI H_2O	Chemistry hood	DI H_2O, 4 baths
REL	Strip	SPR220-3.0	Chemistry hood	Acetone, 2 baths, 5 min. each
REL	Rinse	DI H_2O + Methanol	Chemistry hood	Successive soaks: 50%/50%, 25%/75% DI H_2O/methanol, then 100% methanol 2 baths
REL	CPD	CO_2	Tousimis	Cool 0.5, Fill 1.0, Purge-Vent 0.25, Bleed 0.25, 25 min. purge

				time
-	Anneal	Forming Gas	AG610	300°C load, 20 sec. ramp to 500°C, 30 min. soak, 300°C unload

BIBLIOGRAPHY

[1] L. DeForest, “Space telegraphy,” U.S. Patent 879 532, Feb. 18, 1908.

[2] P. T. Farnsworth, “Television system,” U.S. Patent 1 773 980, Aug. 26, 1930.

[3] J. Shurkin, *Engines of the Mind: The Evolution of the Computer from Mainframes to Microprocessors*, New York, NY: W. W. Norton & Company, 1996.

[4] J. Bardeen and W. Brattain, “The transistor, a semi-conductor triode,” *Physical Review*, vol. 74, no. 2, pp. 230-231, Jul. 1948.

[5] J. R. Harris, “The earliest solid-state digital computers,” *IEEE Annals of the History of Computing*, vol. 21, pp. 49-54, Oct.-Dec. 1999.

[6] W. Shockley, M. Sparks, and G. K. Teal, “p-n junction transistors,” *Physical Review*, vol. 83, no. 1, pp. 151-162, Jul. 1951.

[7] G. K. Teal, “Methods of producing semiconductive bodies,” U.S. Patent 2 727 840, Dec. 20, 1955.

[8] M. Sparks and G. K. Teal, “Method of making P-N junctions in semiconductor materials,” U.S. Patent 2 631 356, Mar. 17, 1953.

[9] L. C. Brown, “Flyable TRADIC: The first airborne transistorized digital computer,” *IEEE Annals of the History of Computing*, vol. 21, pp. 55-61, Oct.-Dec. 1999.

[10] M. Tannenbaum *et al.*, “Silicon n-p-n grown junction transistors,” *Journal of Applied Physics*, vol. 26, no. 6, pp. 686-692, Jun. 1955.

[11] R. Norman, J. Last, and I. Haas, “Solid-state micrologic elements,” in *1960 IEEE International Solid-State Circuits Conference Digest of Technical Papers*, San Francisco, CA, 1960, pp. 82-83.

[12] D. Kahng, “Electric field controlled semiconductor devices,” U.S. Patent 3 102

230, Aug. 27, 1963.

[13] R. H. Norman and H. E. Stephenson, "Shift register employing insulated gate field effect transistors," U.S. Patent 3 454 785, Jul. 8, 1969.

[14] G. Moore, "Cramming more components onto integrated circuits," *Electronics*, vol. 38, no. 8, pp. 114-116, Apr. 1965.

[15] W. Aspray, "The Intel 4004 microprocessor: What constituted invention?" *IEEE Annals of the History of Computing*, vol. 19, pp. 4-15, Jul-Sep. 1997.

[16] A. C. Kay, "A personal computer for children of all ages," in *Proceedings of the ACM Annual Conference*, vol. 1, New York, NY, 1972.

[17] C. T.-C. Nguyen, "Integrated micromechanical circuits for RF front ends," in *Proceedings of the 32nd European Solid-State Circuits Conference*, Montreaux, Switzerland, 2006, pp. 7-16.

[18] J. Wang, J. E. Butler, T. Feygelson, and C. T.-C. Nguyen, "1.51-GHz nanocrystalline diamond micromechanical disk resonator with material-mismatched isolating support," in *Proceedings of the 17th IEEE International Conference on Micro Electro Mechanical Systems*, Maastricht, The Netherlands, 2004, pp. 641-644.

[19] S. Pourkamali, G. K. Ho, and F. Ayazi, "Low-impedance VHF and UHF capacitive silicon bulk acoustic-wave resonators – part II: Measurement and characterization," *IEEE Transactions on Electron Devices*, vol. 54, pp. 2024-2030, Aug. 2007.

[20] D. Weinstein and S. A. Bhave, "Internal dielectric transduction of a 4.5 GHz silicon bar resonator," in *IEEE 2007 International Electron Devices Meeting Technical Digest*, Washington, DC, 2007, pp. 415-418.

[21] P. F. Van Kessel, L. J. Hornbeck, R. E. Meier, and M. R. Douglass, "A MEMS-based projection display," *Proceedings of the IEEE*, vol. 86, pp. 1687-1704, Aug. 1998.

[22] W.-L. Huang, S.-S. Li, Z. Ren, and C. T.-C. Nguyen, "UHF nickel micromechanical spoke-supported ring resonators," in *Digest of Technical*

Papers of the 14th International Conference on Solid-State Sensors, Actuators, and Microsystems, Lyon, France, 2007, pp. 323-326.

[23] M. W. Putty and K. Najafi, "A micromachined vibrating ring gyroscope," in *1994 Solid-State Sensor and Actuator Workshop Technical Digest*, Hilton Head, SC, 1994, pp. 213-220.

[24] W.-T. Hsu, S. Lee, and C. T.-C. Nguyen, "In situ localized annealing for contamination resistance and enhanced stability in nickel micromechanical resonators," in *10th International Conference on Solid-State Sensors, Actuators, and Microsystems Digest of Technical Papers*, Sendai, Japan, 1999, pp. 932-935.

[25] W.-L. Huang, Z. Ren, Y.-W. Lin, H.-Y. Chen, J. Lahann, and C. T.-C. Nguyen, "Fully monolithic CMOS nickel micromechanical resonator oscillator," in *Proceedings of the 21st IEEE International Conference on Micro Electro Mechanical Systems*, Tuscon, AZ, 2008, pp. 10-13.

[26] E. P. Quevy, A. San Paulo, E. Basol, R. T. Howe, T.-J. King, and J. Bokor, "Back-end-of-line poly-SiGe disk resonators," in *Proceedings of the 19th IEEE International Conference on Micro Electro Mechanical Systems*, Istanbul, Turkey, 2006, pp. 234-237.

[27] M.-A. Dubois, J.-F. Carpentier, P. Vincent, C. Billard, G. Parat, C. Muller, P. Ancey, and P. Conti, "Monolithic above-IC resonator technology for integrated architectures in mobile and wireless communication," *IEEE Journal of Solid-State Circuits*, vol. 41, pp. 7-16, Jan. 2006.

[28] R. Ruby, P. Bradley, J. Larson III, Y. Oshmyansky, and D. Figueredo, "Ultra-miniature high-Q filters and duplexers using FBAR technology," in *2001 IEEE International Solid-State Circuits Conference Digest of Technical Papers*, San Francisco, CA, 2001, pp. 120-121.

[29] H.-C. Hsieh, J. C. Hung, A. S. J. Chin, S.-C. Lee, J.-J. Shin, R.-G. Liu, and B. J. Lin, "Mask cost and cycle time reduction," in *Proceedings of SPIE*, vol. 5130, Yokohama, Japan, 2003, pp. 4-15.

[30] C.-C. Lo, F. Chen, and G. K. Fedder, "Integrated HF CMOS-MEMS square-frame resonators with on-chip electronics and electrothermal narrow gap mechanism," in *13th International Conference on Solid-State Sensors, Actuators, and Microsystems Digest of Technical Papers*, Seoul, South Korea, 2005, pp. 2074-2077.

[31] W.-C. Chen, C.-S. Chen, K.-A. Wen, L.-S. Fan, W. Fang, and S.-S. Li, "A generalized foundry CMOS platform for capacitively-transduced resonators monolithically integrated with amplifiers," in *Proceedings of the 23rd IEEE International Conference on Micro Electro Mechanical Systems*, Hong Kong, 2010, pp. 204-207.

[32] J. M. Bustillo, R. T. Howe, and R. S. Muller, "Surface micromachining for microelectromechanical systems," *Proceedings of the IEEE*, vol. 86, pp. 1552-1574, Aug. 1998.

[33] M. K. Zalalutdinov, J. D. Cross, J. W. Baldwin, B. R. Ilic, W. Zhou, B. H. Houston, and J. M. Parpia, "CMOS-integrated RF MEMS resonators," *IEEE/ASME Journal of Microelectromechanical Systems*, vol. 19, pp. 807-815, Aug. 2010.

[34] H. C. Nathanson, W. E. Newell, R. A. Wickstrom, and J. R. Davis, Jr., "The resonant gate transistor," *IEEE Transactions on Electron Devices*, vol. ED-14, pp. 117-133, Mar. 1967.

[35] D. Grogg, M. Mazza, D. Tsamados, A. M. Ionescu, "Multi-gate vibrating-body field effect transistor (VB-FETs)," in *IEEE 2008 International Electron Devices Meeting Technical Digest*, Washington, DC, 2008, pp. 663-666.

[36] D. Grogg, S. Ayoz, D. Tsamados, A. M. Ionescu, "Small signal modeling of charge and piezoresistive modulations in active MEM resonators," in *Proceedings of the 39th European Solid State Device Research Conference*, Athens, Greece, 2009, pp. 379-382.

[37] D. Weinstein and S. A. Bhave, "The resonant body transistor," *Nano Letters*, vol. 10, no. 4, pp. 1234-1237, Feb. 2010.

[38] D. Weinstein and S. A. Bhave, "Internal dielectric transduction in bulk-mode resonators," *IEEE/ASME Journal of Microelectromechanical Systems*, vol. 18, pp. 1401-1408, Dec. 2009.

[39] S. Nuttinck, B. Parvais, G. Curatola, and A. Mercha, "Double-gate finFETs as a CMOS technology downscaling option: An RF perspective," *IEEE Transactions on Electron Devices*, vol. 54, pp. 279-283. Feb. 2007.

[40] B. Parvais, V. Subramanian, A. Mercha, M. Dehan, P. Wambacq, W. Sansen, G.

Groeseneken, and S. Decoutere, “FinFET technology for analog and RF circuits,” in *Proceedings of the 14th IEEE International Conference on Electronics, Circuits, and Systems*, Marrakech, Morocco, 2007, pp. 182-185.

[41] V. Subramanian, A. Mercha, B. Parvais, M. Dehan, G. Groeseneken, W. Sansen, and S. Decoutere, “Identifying the bottlenecks to the RF performance of finFETs," in *Proceedings of the 23rd International Conference on VLSI Design*, Bangalore, India, 2010, pp. 111-116.

[42] V. Subramanian, B. Parvais, J. Borremans, A. Mercha, D. Linten, P. Wambacq, J. Loo, M. Dehan, C. Gustin, N. Collaert, S. Kubicek, R. Lander, J. Hooker, F. Cubaynes, S. Donnay, M. Jurczak, G. Groeseneken, W. Sansen, and S. Decoutere, “Planar bulk MOSFETs versus finFETs: An analog/RF perspective,” *IEEE Transactions on Electron Devices*, vol. 53, pp. 3071-3079, Dec. 2006.

[43] J. Borremans, B. Parvais, M. Dehan, S. Thijs, P. Wambacq, A. Mercha, M. Kuijk, G. Carchon, and S. Decoutere, “Perspective of RF design in future planar and finFET CMOS,” in *2008 IEEE Radio Frequency Integrated Circuits* Symposium, Atlanta, GA, 2008, pp. 75-78.

[44] J. Yue and J. Kriz, “SOI CMOS technology for RF system-on-chip applications,” *Microwave Journal*, vol. 45, no. 1, pp.104-108, 2002.

[45] S. Bouwstra, F. R. Blom, T. S. J. Lammerink, H. Yntema, P. Schrap, J. H. J. Fluitman, and M. Elwenspoek, “Excitation and detection of vibrations of micromechanical structures using a dielectric thin film,” *Sensors and Actuators*, vol. 17, no. 1-2, pp. 219-223, May 1989.

[46] S. Senturia, *Microsystem Design*, New York, NY: Springer Science+Business Media, Inc., 2001.

[47] G. G. Stoney, “The tension of metallic films deposited by electrolysis,” *Proceedings of the Royal Society of London, Series A: Mathematical and Physical Sciences*, vol. 82, no. 553, pp. 172-175, May 1909.

[48] S. A. Bhave and R. T. Howe, “Silicon nitride-on-silicon bar resonator using internal electrostatic transduction,” in *13th International Conference on Solid-State Sensors, Actuators, and Microsystems Digest of Technical Papers*, Seoul, South Korea, 2005, pp. 2139-2142.

[49] H. Chandrahalim, D. Weinstein, L. F. Cheow and S. A. Bhave, "High-κ dielectrically transduced MEMS thickness shear mode resonators and tunable channel-select RF filters," *Sensors and Actuators A: Physical*, vol. 136, no. 2, pp. 527-539, Jan. 2007.

[50] Y.-W. Lin, S.-S. Li, Y. Xie, Z. Ren, and C. T.-C. Nguyen, "Vibrating micromechanical resonators with solid dielectric capacitive transducer gaps," in *Proceedings of the 2005 IEEE International Frequency Control Symposium and Exposition*, Vancouver, BC, Canada, 2005, pp. 128-134.

[51] L.-W. Hung, Y. Xie, Y.-W. Lin, S.-S. Li, Z. Ren, C. T.-C. Nguyen, "UHF micromechanical compound-(2,4) mode ring resonators with solid-gap transducers," in *Proceedings of the Joint Meeting of the 21st European Frequency and Time Forum and the 2007 IEEE International Frequency Control Symposium*, Geneva, Switzerland, 2007, pp. 1370-1375.

[52] M. Ziaei-Moayyed, D. Elata, J. Hsieh, J.-W. P. Chen, E. P. Quevy and R. T. Howe, "Fully differential internal electrostatic transduction of a lamé-mode resonator," in *Proceedings of the 22nd IEEE International Conference on Micro Electro Mechanical Systems*, Sorrento, Italy, 2009, pp. 931-934.

[53] M. Ziaei-Moayyed, E. P. Quevy, J. Hsieh, and R. T. Howe, "Efficient internal electrostatic transduction of the 41st radial mode of a ring resonator," in *Proceedings of the 23rd IEEE International Conference on Micro Electro Mechanical Systems*, Hong Kong, 2010, pp. 711-714.

[54] J.-M. Baik and R. B. Thompson, "Ultrasonic scattering from imperfect interfaces: a quasi-static model," *Journal of Nondestructive Evaluation*, vol. 4, no. 3-4, pp. 177-196, 1984.

[55] J. H. T. Ransley, C. Durkan, and A. A. Seshia, "A depletion layer actuator," in *14th International Conference on Solid-State Sensors, Actuators, and Microsystems Digest of Technical Papers*, Lyon, France, 2007, pp. 1393-1396.

[56] S. W. P. van Sterkenburg, "The electrostriction of silicon and diamond," *Journal of Physics D: Applied Physics*, vol. 25, no. 6, pp. 996-1003, Jun. 1992.

[57] J. S. Yang and S. Krishnaswamy, "An approximate analysis of thickness-stretch waves in an elastic plate," *Wave Motion*, vol. 30, no. 4, pp. 291-301, Mar. 1999.

[58] J. E.-Y. Lee and A. A. Seshia, "Parasitic feedthrough cancellation techniques for enhanced electrical characterization of electrostatic microresonators," *Sensors and Actuators A: Physical*, vol. 156, no. 1, pp. 36-42, Feb. 2009.

[59] A. K. Samarao and F. Ayazi, "Temperature compensation of silicon micromechanical resonators via degenerate doping," in *IEEE 2009 International Electron Devices Meeting Technical Digest*, Baltimore, MD, 2009, pp. 789-792.

[60] R. Tabrizian, M. Rais-Zadeh, and F. Ayazi, "Effect of phonon interactions on limiting the $f \cdot Q$ product of micromechanical resonators," in *15th International Conference on Solid-State Sensors, Actuators, and Microsystems Digest of Technical Papers*, Denver, CO, 2009, pp. 2131-2134.

[61] P. G. Klemens, "The scattering of low-frequency lattice waves by static imperfections," *Proceedings of the Physical Society of London, Section A*, vol. 68, no. 12, pp. 1113-1128, Dec. 1955.

[62] T. O. Woodruff and H. Ehrenreich, "Absorption of sound in insulators," *Physical Review*, vol. 123, no. 5, pp. 1553-1559, Sept. 1961.

[63] H. J. Maris, "Interaction of sound waves with thermal phonons in dielectric crystals," in *Physical Acoustics: Principles and Methods*, 1st ed., vol. VIII. W. P. Mason and R. N. Thurston, Eds. New York, NY: Academic Press, Inc., 1971, pp. 279-345.

[64] J. M. Ziman, "The effect of free electrons on lattice conduction," *Philosophical Magazine*, vol. 2, no. 14, pp. 292, Feb. 1957.

[65] V. V. Kosarev, "Scattering of phonons by carriers in the field of charged impurities," *Soviet Journal of Experimental and Theoretical Physics*, vol. 33, p. 793, 1971.

[66] T. Rocheleau, T. Ndukum, C. Macklin, J. B. Hertzberg, A. A. Clerk, and K. C. Schwab, "Preparation and detection of a mechanical resonator near the ground state of motion," *Nature*, vol. 463, no. 7277, pp. 72-75, Jan. 2010.

[67] A. D. O'Connell, M. Hofheinz, M. Ansmann, R. C. Bialczak, M. Lenander, E. Lucero, M. Neeley, D. Sank, H. Wang, M. Weides, J. Wenner, J. M. Martinis, and A. N. Cleland, "Quantum ground state and single-phonon control of a mechanical resonator," *Nature*, vol. 464, no. 7289, pp. 697-703, Apr. 2010.

[68] L.-Y. Yap, L.-K. Yap, W. Ye, "Air damping in an ultra-high-frequency disk resonator," in *Proceedings of the 6th International Conference on Modeling and Simulation of Microsystems*, vol. 2, San Francisco, CA, 2003, pp. 444-447.

[69] C. Zener, "Internal friction in solids – I. Theory of internal friction in reeds," *Physical Review*, vol. 52, no. 3, pp. 230-235, Aug. 1937.

[70] C. Zener, "Internal friction in solids – II. General theory of thermoelastic internal friction," *Physical Review*, vol. 53, no. 1, pp. 230-235, Jan. 1938.

[71] R. N. Candler, M. Hopcroft, W.-T. Park, S. A. Chandorkar, G. Yama, K. E. Goodson, M. Varghese, A. E. Duwel, A. Partridge, M. Lutz, and T. W. Kenny, "Reduction in thermoelastic dissipation in micromechanical resonators by disruption of heat transport," in *2004 Solid-State Sensor, Actuator, and Microsystems Workshop Technical Digest*, Hilton Head, SC, 2004, pp. 45-48.

[72] S. A. Chandorkar, H. Mehta, M. Agarwal, M. A. Hopcroft, C. M. Jha, R. N. Candler, G. Yama, G. Bahl, B. Kim, R. Melamud, K. E. Goodson, and T. W. Kenny, "Non-isothermal micromechanical resonators," in *Proceedings of the 20th IEEE International Conference on Micro Electro Mechanical Systems*, Kobe, Japan, 2007, pp. 211-214.

[73] S. A. Chandorkar, R. N. Candler, A. E. Duwel, R. Melamud, M. Agarwal, K. E. Goodson, and T. W. Kenny, "Multimode thermoelastic dissipation," *Journal of Applied Physics*, vol. 105, no. 4, 043505, Feb. 2009.

[74] W. P. Mason and T. B. Bateman, "Ultrasonic-wave propagation in pure silicon and germanium," *Journal of the Acoustical Society of America*, vol. 36, no. 4, pp. 644-652, Apr. 1964.

[75] Y. V. Ilisavskii and V. M. Sternin, "Lattice absorption of high-frequency sound in silicon," *Soviet Physics – Solid State*, vol. 27, no. 2, pp. 236-239, Feb. 1985.

[76] R. Tubino, L. Piseri, and G. Zerbi, "Lattice dynamics and spectroscopic properties by a valence force potential of diamondlike crystals: C, Si, Ge, and Sn," *Journal of Chemical Physics*, vol. 56, no. 3, pp. 1022-1039, 1972.

[77] J. M. Ziman, *Electrons and Phonons: The Theory of Transport Phenomena in Solids*, Oxford: Clarendon Press, 1960.

[78] C. Herring, "Role of low-energy phonons in thermal conduction," *Physical Review*, vol. 95, no. 4, pp. 954-965, Aug. 1954.

[79] A. Akheiser, *J . Phys. USSR*, pp. 1277, 1939.

[80] E. Grüneisen, "The state of a body," *Handbook of Physics*, vol. 10, pp. 1-52. NASA translation RE2-18-59W

[81] J. S. Shah and M. E. Straumanis, "Thermal expansion behavior of silicon at low temperatures," *Solid State Communications*, vol. 10, no. 1, pp. 159-162, 1972.

[82] W. B. Gauster, "Low-temperature Grüneisen parameters for silicon and aluminum," *Physical Review B*, vol. 4, no. 4, pp. 1288-1296, Aug. 1971.

[83] J. Philip and M. A. Breazeale, "Third-order elastic constants and Grüneisen parameters of silicon and germanium between 3 and 300 °K," *Journal of Applied Physics*, vol. 54, no. 2, pp. 752-757, Feb. 1983.

[84] C. Yamanouchi, K. Mizuguchi, W. Sasaki, "Electrical conduction in phosphorus doped silicon at low temperatures," *Journal of the Physical Society of Japan*, vol. 22, no. 3, pp. 859-864, Mar. 1967.

[85] K. Wang, A.-C. Wong, and C. T.-C. Nguyen, "VHF free-free beam high-*Q* micromechanical resonators," *IEEE/ASME Journal of Microelectromechanical Systems*, vol. 9, pp. 347-360, Sep. 2000.

[86] M. Konno and H. Nakamura, "Equivalent electrical network for the transversely vibrating uniform bar," *Journal of the Acoustical Society of America*, vol. 38, no. 4, pp. 614-622, Oct. 1965.

[87] A. El Habti and F. O. Bastien, "Low temperature limitation on the quality factor of quartz resonators," *IEEE Transactions on Ultrasonics, Ferroelectrics, and Frequency Control*, vol. 41, pp. 250-255, Mar. 1994.

[88] A. Ward and D. A. Broido, "Intrinsic phonon relaxation times from first-principles studies of the thermal conductivities of Si and Ge," *Physical Review B*, vol. 81, no. 8, 085205, Feb. 2010.

[89] G. G. Sahasrabudhe and S. D. Lambade, "Temperature dependence of the collective phonon relaxation time and acoustic damping in Ge and Si," *Journal of Physics and Chemistry of Solids*, vol. 60, no. 6, pp. 773-785, Jun. 1999.

[90] W.-C. Li, Y. Lin, B. Kim, Z. Ren, C. T.-C. Nguyen, "Quality factor enhancement in micromechanical resonators at cryogenic temperatures," in *15th International Conference on Solid-State Sensors, Actuators, and Microsystems Digest of Technical Papers*, Denver, CO, 2009, pp. 1445-1448.

[91] M. Asheghi, K. Kurabayashi, R. Kasnavi, and K. E. Goodson, "Thermal conduction in doped single-crystal silicon films," *Journal of Applied Physics*, vol. 91, no. 8, pp. 5079-5088, Apr. 2002.

[92] J. Callaway, "Model for lattice thermal conductivity at low temperatures," *Phys. Rev.*, vol. 113, no. 4, pp. 1046-1051, Feb. 1959.

[93] M. Asheghi, Y. K. Leung, S. S. Wong, and K. E. Goodson, "Phonon-boundary scattering in thin silicon layers," *Applied Physics Letters*, vol. 71, no. 13, pp. 1798-1800, Sep. 1997.

[94] D. Fortier and K. Suzuki, "Effect of P donors on thermal phonon scattering in Si," *Journal of Physics*, vol. 37, no. 2, pp. 143-147, 1976.

[95] V. Radhakrishnan, P. C. Sharma, and M. Singh, "Electron-phonon interaction in *P*-doped silicon at low temperatures," *Zeitschrift für Physik B Condensed Matter*, vol. 39, pp. 15-19, Mar. 1980.

[96] W. P. Mason and T. B. Bateman, "Ultrasonic attenuation and velocity changes in doped *n*-type germanium and *p*-type silicon and their use in determining an intrinsic electron and hole scattering time," *Physical Review Letters*, vol. 10, no. 5, pp. 151-154, Mar. 1963.

[97] V. B. Braginsky, V. P. Mitrofanov, and V. I. Panov, *Systems with Small Dissipation*, Chicago: The University of Chicago Press, 1985.

[98] M. N. Alexander and D. F. Holcomb, "Semiconductor-to-metal transition in *n*-type group IV semiconductors," *Reviews of Modern Physics*, vol. 40, no. 4, pp. 815-829, Oct. 1968.

[99] N. Mikoshiba, "Model for the metal-nonmetal transition in impure semiconductors," *Reviews of Modern Physics*, vol. 40, no. 4, pp. 833-838, Oct. 1968.

[100] P. G. Steeneken, J. J. M. Ruigrok, S. Kang, J. T. M. van Beek, J. Bontemps, and J. J. Koning, "Parameter extraction and support-loss in MEMS resonators," presented at the *COMSOL Conference 2007*, Boston, MA, 2007.

[101] C. Bourgeois, E. Steinsland, N. Blanc, and N. F. de Rooij, "Design of resonators for the determination of the temperature coefficients of elastic constants of monocrystalline silicon," in *Proceedings of the 1997 IEEE International Frequency Control Symposium*, Orlando, FL, 1997, pp. 791-799.

[102] S. A. Bhave, D. Gao, R. Maboudian, and R. T. Howe, "Fully-differential poly-SiC lamé-mode resonator and checkerboard filter," in *Proceedings of the 18th IEEE International Conference on Micro Electro Mechanical Systems*, Miami, FL, 2005, pp. 223-226.

[103] J. Arcamone, E. Colinet, A. Niel, and E. Ollier, "Efficient capacitive transductionof high-frequency micromechanical resonators by intrinsic cancellation of parasitic feedthrough capacitances," *Applied Physics Letters*, vol. 97, 043505, Jul. 2010.

[104] T. J. Kippenberg and K. J. Vahala, "Cavity optomechanics: back-action at the mesoscale," *Science*, vol. 321, no. 5893, pp. 1172-1176, Aug. 2008.

[105] G. S. Wiederhecker, L. Chen, A. Gondarenko, and M. Lipson, "Controlling photonic structures using optical forces," *Nature*, vol. 462, no. 7273, pp. 633-636, Dec. 2009.

[106] S. Sridaran and S. A. Bhave, "Electrostatic actuation of silicon optomechanical resonators," *Optics Express*, vol. 19, no. 10, pp. 9020-9026, Apr. 2011.

[107] J. T. M. van Beek, K. L. Phan, G. J. A. M. Verheijden, G. E. J. Koops, C. van der Avoort, J. van Wingerden, D. Ernur Badaroglu, J. J. M. Bontemps, and R. Puers, "A piezo-resistive resonant MEMS amplifier," in *IEEE 2008 International Electron Devices Meeting Technical Digest*, Washington, DC, 2008, pp. 667-670.

[108] J. F. Creemer, F. Fruett, G. C. M. Meijer, and P. J. French, "The piezojunction

effect in silicon sensors and circuits and its relation to piezoresistance," *IEEE Sensors Journal*, vol. 1, pp. 98-108, Aug. 2001.

[109] S. Sugiyama, M. Takigawa, I. Igarashi, "Integrated piezoresistive pressure sensor with both voltage and frequency output," *Sensors and Actuators*, vol. 4, pp. 113-120, Jan. 1983.

[110] V. Mosser, J. Suski, J. Goss, E. Obermeier, "Piezoresistive pressure sensors based on polycrystalline silicon," *Sensors and Actuators A: Physical*, vol. 28, no. 2, pp. 113-132, Jul. 1991.

[111] F. A. Levinzon, "Noise of the JFET amplifier," *IEEE Transactions on Circuits and Systems – I: Fundamental Theory and Applications*, vol. 47, pp. 981-985, Jul. 2000.

[112] M. Chu, T. Nishida, X. Lv, N. Mohta, and S. E. Thompson, "Comparison between high-field piezoresistance coefficients of Si metal-oxide semiconductor field-effect transistors and bulk Si under uniaxial and biaxial stress," *Journal of Applied Physics*, vol. 103, no. 11, 113704, Jun. 2008.

[113] K. H. Hung, P. K. Ko, C. Hu, and Y. C. Cheng, "A unified model for the flicker noise in metal-oxide-semiconductor field-effect transistors," *IEEE Transactions on Electron Devices*, vol. 37, pp. 654-665, Mar. 1990.

[114] A. van der Ziel, "Flicker noise in semiconductors: Not a true bulk effect," *Applied Physics Letters*, vol. 33, no. 10, pp. 883-884, 1978.

[115] A. Hajimiri and T. H. Lee, "A general theory of phase noise in electrical oscillators," *IEEE Journal of Solid-State Circuits*, vol. 33, pp. 179-194, Feb. 1998.

[116] S. M. Sze, "MESFET and related devices," in *Semiconductor Devices: Physics and Technology*, 2nd ed. Singapore: John Wiley & Sons, 2001, pp. 224-253.

[117] Y. Kanda, "A graphical representation of the piezoresistance coefficients in silicon," *IEEE Transactions on Electron Devices*, vol. ED-29, pp. 64-70, Jan. 1982.

[118] D. M. Caughey and R. E. Thomas, "Carrier mobilities in silicon empirically

related to doping and field," *Proceedings of the IEEE*, vol. 55, pp. 2192-2193, Dec. 1967.

[119] Y. Taur and T. H. Ning, "CMOS process flow," in *Fundamentals of Modern VLSI Devices*, 9th ed. New York: Cambridge University Press, 2006, pp. 414-417.

[120] T. H. Lee, "Chapter 19: Architectures," in *The Design of CMOS Radio-Frequency Integrated Circuits*, 2nd ed., New York, NY: Cambridge University Press, 2004, pp. 694-763.

[121] A.-C. Wong and C. T.-C. Nguyen, "Micromechanical mixer-filters ("mixlers")," *IEEE/ASME Journal of Microelectromechanical Systems*, vol. 13, pp. 100-112, Feb. 2004.

[122] A. T. Alastalo, M. Koskenvuori, H. Seppä, and J. Dekker, "A micromechanical resonating RF mixer," in *Proceedings of the 34th European Microwave Conference*, Amsterdam, The Netherlands, 2004, pp. 1297-1300.

[123] S. M. Sze, "Photonic Devices," in *Semiconductor Devices: Physics and Technology*, 2nd ed. Singapore: John Wiley & Sons, 2001, pp. 282-331.

[124] C. T.-C. Nguyen and J. Kitching, "Towards chip-scale atomic clocks," in *2005 IEEE International Solid-State Circuits Conference Digest of Technical Papers*, San Francisco, CA, 2005, pp. 84-85.

[125] J. Kitching, S. Knappe, L.-A. Liew, P. D. D. Schwindt, V. Gerginov, V. Shah, J. Moreland, A. Brannon, J. Breitbarth, Z. Popovic, and L. Hollberg, "Chip-scale atomic frequency references," in *Proceedings of the ION GNSS 18th International Technical Meeting of the Satellite Division*, Long Beach, CA, 2005, pp. 1662-1669.

[126] V. Shah, S. Knappe, L. Hollberg, and J. Kitching, "Generation of coherent population trapping resonances with nearly 100% transmission contrast," in *Proceedings of the Joint Meeting of the 21st European Frequency and Time Forum and the 2007 IEEE International Frequency Control Symposium*, Geneva, Switzerland, 2007, pp. 1339-1341.

[127] A. N. Cleland, *Foundations of Nanomechanics: From Solid-State Theory to Device Applications*, Berlin: Springer-Verlag, 2003.

[128] G. W. Neudeck, "The PN junction diode," in *Modular Series on Solid State Devices*, vol. 2, 2nd ed., R. F. Pierret and G. W. Neudeck, Eds. Reading, MA: Addison-Wesley, 1989.

[129] K. F. Graff, *Wave Motion in Elastic Solids*, New York: Dover Publications, 1991.

[130] V. Kaajakari, *Practical MEMS*, Las Vegas, NV: Small Gear Publishing, 2009.

[131] J. D. Plummer, M. D. Deal, P. B. Griffin, *Silicon VLSI Technology: Fundamentals, Practice, and Modeling*, Upper Saddle River, NJ: Prentice Hall, 2000.